

ALICE-ANA-2014-xxx  
January 25, 2023

# Strangeness Production ( $\Lambda$ ) in Jets and Medium in p-Pb collisions at $\sqrt{s_{NN}} = 5.02$ TeV

Ryan Hannigan

1. University of Texas at Austin

Emails: ryan.hannigan@austin.utexas.edu

## Abstract

By studying strange hadrons in proton-proton, proton-nucleus, and heavy ion collisions, one can investigate strange quark production and hadron formation with respect to increasing system size. Recent measurements show an enhancement of strange particles (e.g. an increase in the  $\Lambda/\pi$  ratio) in p-Pb and high multiplicity pp collisions. In order to probe the origin of this increase, it is necessary to separate the strange particles produced in hard processes (jets) from those produced in soft processes (bulk). By examining this trend from low to high multiplicity p-Pb collisions, we are able to study the onset of this enhancement from small to large collision systems.

Two-particle jet-like angular correlations with identified strange hadrons in p-Pb collisions allow us to measure both the jet and non-jet components of strange particle production. Modifications in the production mechanisms across different system sizes can be probed by examining changes in the  $\Lambda/h$  ratio within jets and in the underlying event separately. In addition, changes to the jet hadrochemistry via medium interactions are studied by measuring strangeness production in the away-side jet. In this note we present the first measurements of the  $\Lambda/h$  ratio in jets as a function of multiplicity using jet-like hadron- $\Lambda$  angular correlations in p-Pb collisions at  $\sqrt{s_{NN}} = 5.02$  TeV.



---

23 **Contents**

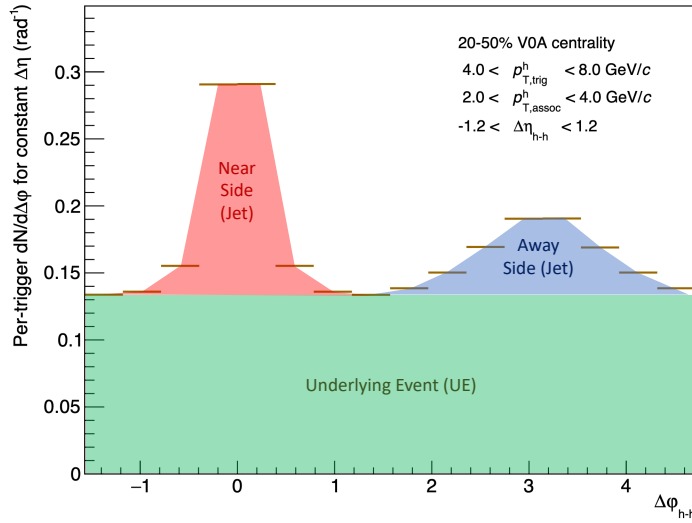


**Fig. 1:** A h-h  $\Delta\phi$  distribution taken from this analysis with the near-side, away-side, and uncorrelated regions highlighted.

## 1 Introduction

### 1.1 Motivation

Recent studies have shown that the ratio of the yield of  $\Lambda$  baryons to charged pions differs between pp, p-Pb and PbPb collisions, specifically in the mid- $p_T$  region of 1–4 GeV/c. Additionally, similar studies have seen an increase in the  $\Lambda/(\pi^+ + \pi^-)$  yields as a function of charged particle multiplicity in p-Pb collisions. The origin of this increase is still unknown.

By performing angular correlations of a high  $p_T$  trigger hadron with an associated  $\Lambda$  (or charged hadron as a proxy for a pion) in p-Pb events, we are able to separate out  $\Lambda$  baryon production into three distinct kinematic regions:

- The near-side peak of the correlation, corresponding to jet-like production with no medium interactions,
- The away-side peak of the correlation, corresponding to jet-like production with possible medium interaction, and
- The uncorrelated pairs, corresponding to the “underlying event” or soft production within the medium.

A h-h  $\Delta\phi$  distribution with these regions highlighted is shown in Figure ??.

For this study, 1-d  $\Delta\phi$  angular correlations of jet-like  $h - \Lambda$  and  $h - h$  pairs were measured in p-Pb events independently for three multiplicity bins (0-20%, 20-50%, 50-80%), and the final ratios of yields of correlated pairs were compared to study the onset of this enhancement.

### 1.2 Dataset and Event Selection

#### 1.2.1 Dataset

Every event in this analysis was a p-Pb collision at  $\sqrt{s_{NN}} = 5.02$  TeV taken from the following runlist which consists of 32 runs during the LHC16q period:

47 **265525, 265521, 265501, 265500, 265499, 265435, 265427, 265426, 265425, 265424, 265422, 265421,**  
 48 **265420, 265419, 265388, 265387, 265385, 265384, 265383, 265381, 265378, 265377, 265344, 265343,**  
 49 **265342, 265339, 265338, 265336, 265335, 265334, 265332, 265309**

50 This analysis uses the data from these runs with the FAST reconstruction, corresponding to approxi-  
 51 mately 400 million minimum bias events.

52 For the majority of the MC studies (MC method test, MC Closure test), the analysis was performed  
 53 using the standard purpose generated MC production LHC17f2b\_FAST, anchored to the LHC16q\_FAST  
 54 production. This production consists of around 30 million minimum bias events.

55 Larger statistics were needed to correct for a pairwise hadron- $\Lambda$  inefficiency due to track merging, which  
 56 was done using a template created from analyzing the standard purpose generated pp MC production  
 57 LHC18j2\_FAST, which is anchored to the LHC17q\_FAST production consisting of 15 TeV pp data. This  
 58 MC production contains around N million minimum bias events.

### 59 1.2.2 Event Selection

60 Events were selected by requiring a collision Z-vertex of less than 10 cm and at least 3 reconstructed  
 61 tracks in the event.

62 This reduces the total number of events (FAST + CENT\_wo\_SDD) considered to approximately 420  
 63 million events (see Table ??). The V0A estimator was chosen to determine event multiplicity percentile,  
 64 and the correlation measurement was performed in three multiplicity percentile bins: **0-20%, 20-50%,**  
 65 **and 50-80%.**

Multiplicity	Total Evt.	Has 3 Tracks	$ Z_{vtx}  < 10\text{cm} + 3 \text{ tracks}$	% Pass
0-20%	1.218E08	1.217E08	1.061E08	87.1%
20-50%	1.840E08	1.835E08	1.590E08	86.4%
50-80%	1.850E08	1.804E08	1.563E08	84.5%

**Table 1:** Number of events passing our criteria for each multiplicity bin considered.

66 For all events, the standard Physics selection with pile-up cuts was applied with `AddTaskPhysicsSelection(kFALSE`  
 67 `kTRUE)`.

### 68 1.3 Code Locations

69 The code for this analysis can be found in the following locations:

70 *Correlations in Data and MC:*

- 71 – PWGLF/Strangeness/DPhi/AliAnalysisTaskLambdaHadronRatioV0 (for  $\Lambda$ s reconstructed using  
 72 V0 finder)
- 73 – PWGLF/Strangeness/DPhi/AliAnalysisTaskLambdaHadronRatioRes (for  $\Lambda$ s reconstructed using  
 74 resonance technique)

75 *Efficiency Computation:*

- 76 – PWGLF/Strangeness/DPhi/AliAnalysisTaskLambdaHadronEfficiency (for  $\Lambda$ s reconstructed using  
 77 V0 finder and resonance technique)

78 *MonteCarlo Closure Test*

- PWGLF/Strangeness/DPhi/AliAnalysisTaskLambdaHadronV0Closure (for  $\Lambda$ s reconstructed using V0 finder)
- PWGLF/Strangeness/DPhi/AliAnalysisTaskLambdaHadronResClosure (for  $\Lambda$ s reconstructed using resonance technique)

## 1.4 Relevant Contributions to ALICE Meetings

This analysis was presented at the following ALICE meetings, in reverse chronological order:

- Strangeness PAG Meeting: 10 January 2023 (<https://indico.cern.ch/event/1237832>)
- Strangeness PAG Meeting: 18 October 2022 (<https://indico.cern.ch/event/1211594>)
- Correlations PAG Meeting: 11 October 2022 (<https://indico.cern.ch/event/1210412>)
- Strangeness PAG Meeting: 4 October 2022 (<https://indico.cern.ch/event/1206673>)
- Resonance PAG Meeting: 17 November 2021 (<https://indico.cern.ch/event/1096156>)
- Strangeness PAG Meeting: 4 August 2020 (<https://indico.cern.ch/event/943026>)
- Correlations PAG Meeting: 26 June 2020 (<https://indico.cern.ch/event/903613>)
- Resonance PAG Meeting: 24 June 2020 (<https://indico.cern.ch/event/931429>)

## 2 Track Selection

### 2.1 Associated Hadron Track Cuts

For all associated hadrons, a minimum  $p_T$  cuts of  $p_T > 0.15$  GeV/c was applied. Additionally, an  $\eta$  cut of  $|\eta| < 0.8$  was required. Furthermore, all associated hadrons were required to meet the standard cuts supplied by `AliESDtrackCuts::GetStandardITSTPCTrackCuts2011()` corresponding to track filter bit 1024, with a modified number of `MinNClustersTPC` from the standard cut of 50:

- TPC Refit
- ITS Refit
- **SetMinNClustersTPC: 80**
- SetMaxChi2PerClusterTPC: 4
- SetAcceptKinkDaughters: kFALSE
- SetMaxDCAToVertexZ: 2
- SetMaxDCAToVertexXYPtDep:  $0.0105 + 0.0350/p_T^{1.1}$
- SetDCAToVertex2D: kFALSE
- SetMaxChi2TPCConstrainedGlobal: 36
- SetRequireSigmaToVertex: kFALSE
- SetMaxChi2PerClusterITS: 36

110 For the correlation, the associated hadron is selected only in the momentum region

$$1.0 < p_T < 4.0 \text{ GeV}/c,$$

111 with further binning performed offline. The  $p_T$ ,  $\phi$  and  $\eta$  distributions for the associated hadrons that  
112 pass these cuts in the 0-20% multiplicity bin can be seen in Figure ??.

### 113 **2.2 $\Lambda$ Daughter Proton and Pion Track Cuts**

114 The proton and the pion are required to have a minimum  $p_T$  of  $p_T > 0.15 \text{ GeV}/c$  and an  $\eta$  cut of  
115  $|\eta| < 0.8$ . Furthermore, the proton and pion are required to meet the following quality cuts:

- 116 – TPC refit flag enabled
- 117 – TPC crossed rows  $> 70$
- 118 – (TPC crossed rows)/(findable clusters)  $> 0.8$

119 All of these cuts are applied to the daughters of the reconstructed  $\Lambda$ , independent of the technique used  
120 for said reconstruction. For the correlation, the reconstructed  $\Lambda$  is selected only in the momentum region

$$1.0 < p_T < 4.0 \text{ GeV}/c,$$

121 with further binning performed offline.

### 122 **2.3 Trigger Track Cuts**

123 For the trigger hadron tracks, Hybrid Global constrained tracks were accepted using the cuts supplied by  
124 `IsHybridGlobalConstrainedGlobal()`, or track bit 768:

- 125 – `SetMinNClustersTPC`: 50
- 126 – `SetMaxChi2PerClusterTPC`: 4
- 127 – `SetAcceptKinkDaughters`: kFALSE
- 128 – `SetMaxDCAToVertexZ`: 3.2
- 129 – `SetMaxDCAToVertexXY`: 2.4
- 130 – `SetDCAToVertex2D`: kTRUE
- 131 – `SetMaxChi2TPCConstrainedGlobal`(36)
- 132 – `SetMaxFractionSharedTPCClusters`(0.4)

133 For the both the di-hadron and h- $\Lambda$  correlation, the trigger hadron is selected in the momentum region:

$$4.0 < p_T < 8.0 \text{ GeV}/c,$$

134 with further binning performed offline. The  $p_T$ ,  $\phi$  and  $\eta$  distributions for the trigger hadrons that pass  
135 these cuts in the 0-20% multiplicity bin can be seen in Figure ??.

### 3 $\Lambda$ Reconstruction

The  $\Lambda$  candidates were reconstructed through the  $\Lambda \rightarrow p\pi^-$  ( $\bar{\Lambda} \rightarrow \pi^+p$ ) decay channel with a branching ratio of 63.9%. For the majority of this analysis, the  $\Lambda$  and  $\bar{\Lambda}$  are combined together. Thus, unless otherwise specified,  $\Lambda = \Lambda + \bar{\Lambda}$ .

The  $\Lambda$  candidates in this analysis were reconstructed using two separate techniques:

- **V0 Finder Technique** - The V0 finder technique reconstructs the  $\Lambda$  by combining the proton and pion tracks with the V0 finder algorithm, which can be found within the AliROOT framework.
- **Resonance Technique** - The resonance technique combines all oppositely charged proton-pion pairs to reconstruct the  $\Lambda$ , resulting in maximal statistics at the cost of a large combinatorial background.

The central points in this analysis are from  $\Lambda$  candidates reconstructed using the V0 finder technique. The resonance technique serves as a powerful cross-check to ensure no topological biases are introduced within the V0 finder algorithm, and is investigated in detail in Section ??.

#### 3.1 V0 Selection

The central points in this analysis were generated using  $\Lambda$ s reconstructed using the V0-finder algorithm found within the AliROOT framework. All of the V0s found by the V0 finder algorithm were required to pass the following cuts:

- $p_T > 0.2 \text{ GeV}/c$
- $|\eta| < 0.8$
- On the fly status: disabled (offline V0s only)

There were no additional topological cuts applied to the V0s or their corresponding daughters. This was done to maximize statistics and to minimize any topological biases beyond those introduced by reconstructing  $\Lambda$ s using the V0-finder algorithm.

#### 3.2 V0 Daughter PID Cuts

The daughter protons and pions were required to meet the following PID cuts using both the TPC and TOF detectors:

- \*  $|n\sigma_{TPC,p}| < 2$
- \*  $|n\sigma_{TPC,\pi}| < 3$
- \*  $|n\sigma_{TOF,p}| < 2$  (if signal exists)
- \*  $|n\sigma_{TOF,\pi}| < 3$  (if signal exists)

The  $n\sigma$  values for both the TPC and TOF detectors of the daughter proton and pion are shown in Figure ?? and Figure ??, respectively. These values were obtained from the AOD tracks associated with every V0 found by the V0 finder algorithm, provided that those tracks also pass the aforementioned daughter track quality cuts.



To account for any biases introduced from choosing daughter tracks from the V0 finder algorithm, the TPC and TOF  $n\sigma_{p,\pi}$  distributions are shown for all AOD tracks in the tracklist in Figure ???. There are no major differences between the  $n\sigma$  distributions of the daughter tracks from the V0 finder algorithm and the AOD tracks in the tracklist. This indicates that the V0 finder algorithm is not introducing any biases in the PID selection of the daughter tracks. These plots also represent the PID cuts used for the resonance technique, which utilizes the full AOD track list and will be discussed in Section ??.

### 3.3 Invariant Mass Region

The invariant mass distributions in each multiplicity bin for the  $\Lambda$ s reconstructed using the V0 finder algorithm are shown in Figure ???. The  $\Lambda$  peak is clearly visible with almost zero background.

A Voigt (signal) + 2nd order polynomial (BG) fit was applied to the invariant mass distributions for each multiplicity bin. The extracted parameters from the Voigt fit are shown in Table ???. While the background is nearly zero for each multiplicity bin, its effect on the final correlation measurement is investigated in Section ??.

Multiplicity	A	$\mu$ (GeV/ $c^2$ )	$\sigma$ (GeV/ $c^2$ )	$\gamma$ (GeV/ $c^2$ )	$\chi^2/NDF$
0-20%	1.82e+02	1.116	1.24e-03	1.10e-03	31.24
20-50%	8.58e+01	1.116	1.24e-03	1.07e-03	15.55
50-80%	1.78e+01	1.116	1.23e-03	1.03e-03	4.55

**Table 2:** Parameters from the Voigt fit to the invariant mass distributions for the  $\Lambda$ s reconstructed using the V0 finder, along with the  $\chi^2/NDF$  for the total fit. The errors were negligible relative to the values.

Measuring the  $h - \Lambda$  correlation requires a clearly defined signal region for the unlike-sign  $p\pi$  pairs from the V0 finder. The signal region range is as follows:

$$\text{-- unlike-sign } p\pi \text{ in } \Lambda \text{ mass region: } 1.100 \text{ GeV}/c^2 < M_{p\pi} < 1.134 \text{ GeV}/c^2$$

This signal region was chosen to maximize statistical significance, and it does not depend on multiplicity. As it accounts for roughly 99.5% of the total signal, no correction for the tails of the distribution was applied. However, the choice of signal region and the corresponding correction factors are investigated more closely in Section ??.

## 4 Acceptance and Efficiency Corrections

This section details all of the detector acceptance and efficiency corrections applied to the central values of this analysis. All other corrections are discussed in Section ??.

### 4.1 Mixed Event Acceptance Correction

For each multiplicity bin, events were separated into z-vertex position bins with a width of 2 cm, ranging from  $-10$  cm to  $10$  cm. An AliEventPool of size 500 and track-depth 1000 was filled with a list of trigger tracks, then correlated with a list of associated hadrons (or  $p\pi$  pairs) for each event once the pool was ready. The uncorrected and mixed-event distributions ( $h-p\pi$ ,  $h-h$ ) for each multiplicity bin are shown in Figures ?? through ??.

For each multiplicity bin, the acceptance correction (as described in Eq. 1) was performed for each z-vertex bin, then the results were merged together to form the acceptance-corrected distributions, shown in Figures ?? through ???. Each plot was scaled by  $1/N_{trig}$ .

As this analysis relies on multiple angular correlations ( $h - \Lambda$ ,  $h - h$ ), the event mixing was done with a shared mixed event pool containing the list of trigger tracks, then the correlation was performed using

the associated ( $p\pi$ ) or hadron list for each event. After mixing, each correlation was corrected using its corresponding mixed-event distribution. The event mixing was only performed on events that contained both a  $\Lambda$  candidate ( $p\pi$  pair from either V0 finder or global AOD list) and an associated hadron.

## 4.2 Reconstruction Efficiency

In this section we investigate the reconstruction efficiency of the  $\Lambda$ , trigger and associated hadrons.

### 4.2.1 $\Lambda$ Reconstruction Efficiency

To estimate the  $\Lambda$  reconstruction efficiency, we compare  $\Lambda$  yields reconstructed using the V0 finder to the true  $\Lambda$  yields using the MC production LHC17f2b\_FAST (anchored to LHC16q\_FAST production). The efficiency was calculated using the following formula:

$$\varepsilon_{\Lambda} = \frac{N_{\Lambda, \text{ reco with V0 finder}}}{N_{\Lambda, \text{ real MC yield}}},$$

where each  $\Lambda$  in  $N_{\Lambda, \text{ reco with V0 finder}}$  meets the following criteria:

- Found in the list of offline V0s
- $|\eta_{V0}| \leq 0.8$
- The daughter  $p, \pi$  pass the daughter track cuts outlined in Section ??
- The daughter  $p, \pi$  tracks have corresponding real  $p, \pi$  in the MC stack
- The corresponding MC stack  $p, \pi$  daughters come from the same mother  $\Lambda$  (also in MC stack)

and each  $\Lambda$  in  $N_{\Lambda, \text{ real MC yield}}$  meets the following criteria:

- Found in the MC stack
- $|\eta_{\Lambda}| \leq 0.8$
- The  $\Lambda$  decays to  $p\pi$

While previous analyses focus solely on primary  $\Lambda$ s (excluding  $\Omega$  and  $\Xi$  contamination), there is no requirement for either the V0-reconstructed  $\Lambda$  or the MC-generated  $\Lambda$  to be a primary particle. As this analysis is mostly interested in the  $\Lambda$  due to its strange quark content, whether or not the  $\Lambda$  came from a cascade decay is irrelevant. This is important to note when making comparisons between this analysis and previous analyses, as secondary contamination from cascades accounts for nearly 20% of all  $\Lambda$ s.

As mentioned in Section ??, both the  $\Lambda$  and the  $\bar{\Lambda}$  were combined together for this efficiency calculation. Efficiencies were calculated as a function of  $p_T$ ,  $\eta$ ,  $\phi$ , Event Z vertex, and Multiplicity. However, the final efficiency correction was applied as a function of  $p_T$  only and can be seen in Figure ??.

### 4.2.2 Trigger and Associated Hadron Reconstruction Efficiency

The trigger and associated hadron reconstruction efficiencies are calculated using the following formula:

$$\epsilon_{trig,assoc} = \frac{N_{trig,assoc, \text{ reco yield}}}{N_{trig,assoc, \text{ real MC yield}}},$$

where each trigger or associated hadron in  $N_{trig,assoc, \text{ reco yield}}$  meets the following criteria:

- Found in the list of AOD tracks
- $|\eta_{track}| \leq 0.8$
- The track passes the track cuts outlined in Section ?? (trigger) or ?? (associated)
- The track has a corresponding real track in the MC stack
- The corresponding MC track is either a pion, proton, kaon, electron or muon
- The corresponding MC track is not a secondary particle (`IsPhysicalPrimary() == true`)

and each trigger or associated hadron in  $N_{trig,assoc, \text{ real MC yield}}$  meets the following criteria:

- Found in the MC stack
- $|\eta_{track}| \leq 0.8$
- The track is either a pion, proton, kaon, electron or muon
- The track is not a secondary particle (`IsPhysicalPrimary() == true`)

The efficiencies for both the trigger and associated hadrons as a function of  $p_T$  are shown in Figure ??.

Because all of these efficiencies appear to be multiplicity independent, the final efficiency correction is performed using the integrated 0-100% points shown in red for each of the  $\Lambda$ , trigger and associated efficiency plots.

As our correlation measurement depends on both the trigger and associated particle, we must combine the two efficiencies to get the overall efficiency for the pair. This is done using the following formula:

$$\epsilon_{pair} = \epsilon_{trig} * \epsilon_{assoc}$$

This efficiency is corrected for on-the-fly as the pairs are being filled into the total correlation distribution by using a weighting factor equal to the inverse of  $\epsilon_{pair}$ . The same trigger efficiency used in the pair efficiency is then also to correct our  $N_{trig}$  for our final per-trigger correlation in both the h-h and h- $\Lambda$  case.

### 4.3 Track Merging Efficiency

Many correlation studies are susceptible to track merging inefficiencies, whereby either the trigger or associated particle gets merged over by the other during the track reconstruction. This results in a dip at small angles in the  $\Delta\eta\Delta\phi$  distribution when compared to a similar distribution with no instances of track merging. As this effect cannot be seen directly in data due to the missing reconstructed tracks, it was investigated using our MonteCarlo sample, where we can compare the reconstructed tracks with the MC generated particles they were reconstructed from. While this effect is usually negligible and only relevant at extremely small angles ( $\Delta\phi < 0.01, \Delta\eta < 0.1$ ), in this analysis we see that this effect is more severe and occurs at larger angles ( $\Delta\phi < 1, \Delta\eta < 0.6$ ), shown in Figure ??.

The severity of this effect is likely due to two factors:

- The  $\Lambda$  decay length is large ( $c\tau \approx 10$  cm), meaning the daughter particles will have less hits in the detector than the trigger particle (which is produced at the primary vertex). As Kalman filtering (track reconstruction) favors the track with more hits, the  $\Lambda$  daughter track is “merged” over by the trigger track.[?]
- The  $\Lambda$  decay is assymmetric ( $m_p/m_\pi \approx 7$ ), so the  $\Lambda$  and daughter proton end up with similar momenta (and thus  $\phi$  and  $\eta$ ). This means that whenever a proton from a  $\Lambda$  decay is “merged” over by a trigger track, an  $h - \Lambda$  pair with small  $\Delta\phi, \Delta\eta$  is lost.

To see how the decay length can affect the track merging, we can measure the  $\Delta\eta\Delta\phi$  distributions for  $h$ –proton pairs in our MonteCarlo sample where the proton is secondary—meaning it came from a weak decay with decay length  $\lesssim 2$  cm—and compare it to the same ratio for  $h$ –proton pairs where the proton is primary. The result is shown in Figure ?. All reconstructed triggers and protons are selected from the AOD track list and pass our trigger and daughter cuts from Sections ?? and ??, respectively (with the caveat being that the protons are required to have a corresponding entry in the MC stack and that entry is either secondary or primary).

We can also observe the  $p_T$  dependence of this effect by looking at the reconstructed and ground truth  $h$ –(secondary proton) distributions in different  $p_T$  bins. This effect

This track merging inefficiency in the  $h$ –(secondary proton) distribution manifests itself in our final  $h - \Lambda$  correlation.

This is because protons which came from a  $\Lambda$  decay have similar kinematics to their mother  $\Lambda$  ( $p_T, \phi, \eta$ ), meaning if there is a  $h$ –(secondary proton from  $\Lambda$ ) pair missing from our reconstructed tracks, there will be a corresponding  $h$ – $\Lambda$  pair missing with similar  $p_T, \Delta\eta\Delta\phi$ . To see this, we can compare the  $h - \pi$  and  $h$ –proton distributions, where both the  $\pi$  and proton came from a  $\Lambda$  within our  $2 < p_T < 4$  range. This comparison is shown in Figure ?. As the dip at small  $\Delta\phi, \Delta\eta$  is not present in the  $h - \pi$  distribution, we conclude that the loss of  $h - \Lambda$  pairs at small angles is strictly due to the merging of  $h$ –(secondary proton) pairs.

This effect has been seen in previous correlation studies[?][?], but due to the nature of the  $\Lambda$  decay it is more pronounced in this analysis. As such, we correct this effect by using the following formula:

$$C_{corr.}(\Delta\phi, \Delta\eta) = C_{uncorr.}(\Delta\phi, \Delta\eta) \left( \frac{C_{reco.MC}(\Delta\phi, \Delta\eta)}{C_{real.MC}(\Delta\phi, \Delta\eta)} \right)^{-1}$$

where  $C_{corr.}$  is the corrected correlation,  $C_{uncorr.}$  is the uncorrected correlation, and the efficiency template  $\frac{C_{reco.MC}(\Delta\phi, \Delta\eta)}{C_{real.MC}(\Delta\phi, \Delta\eta)}$  is generated with a large MonteCarlo sample using the same procedure as the MonteCarlo closure test described in Section ?. The efficiency template is shown in Figure ?.

295 This effect is investigated more thoroughly in Section ??.

## 296 5 Correlation Measurement Technique

### 297 5.1 Full Correlation Measurement Method

298 The per-trigger correlation is approximated for each multiplicity bin using the formula:

$$C_{trig}(\Delta\phi, \Delta\eta) = \frac{1}{N_{trig}} \frac{B(0,0) * S(\Delta\phi, \Delta\eta)}{B(\Delta\phi, \Delta\eta)} \quad (1)$$

299 where  $N_{trig}$  is the total number of hadrons in the  $4 < p_T < 8$  GeV/c range that pass our trigger cuts  
 300 described in Section ??,  $S(\Delta\phi, \Delta\eta)$  is the efficiency-corrected (Section ??) same event correlation and  
 301  $B(\Delta\phi, \Delta\eta)$  is the mixed-event correlation. To properly account for the acceptance effects, the mixed-  
 302 event distribution is scaled to the value of the  $(\Delta\phi = 0, \Delta\eta = 0)$  bin of the same event distribution.

303 However, what is actually measured is an angular correlation of  $h - (p\pi)$  pairs that is comprised of the  
 304 real  $h - \Lambda$  signal as well as a background of  $h - (p\pi)$  pairs. The full correlation equation is then:

$$C_{h-\Lambda}(\Delta\phi, \Delta\eta) = r_{\text{Signal}} \left( C_{(h-p\pi)_{\text{Signal}}}^{US}(\Delta\phi, \Delta\eta) - r_{LS} * C_{(h-p\pi)_{\text{RSB}}}^{US}(\Delta\phi, \Delta\eta) \right) \quad (2)$$

305 Where each term is defined as follows:

- 306 –  $C_{h-\Lambda}(\Delta\phi, \Delta\eta)$ : The final  $h - \Lambda$  correlation distribution
- 307 –  $C_{(h-p\pi)_{\text{Signal}}}^{US}$ : The  $h - (p\pi)$  correlation in our signal region
- 308 –  $C_{(h-p\pi)_{\text{RSB}}}^{US}(\Delta\phi, \Delta\eta)$ : The  $h - (p\pi)$  correlation in the right sideband region (RSB)
- 309 –  $r_{\text{Signal}}$ : Scaling factor used to account for fraction of the  $h - \Lambda$  signal that is missed by choosing a  
 310 finite signal region
- 311 –  $r_{LS}$ : Scaling factor used to account for combinatorial background in the  $h - (p\pi)$  correlation

312 In our primary momentum bin ( $2 < p_T < 4$ ) for  $\Lambda$ s reconstructed using the V0 finder,  $r_{\text{Signal}}$  is nearly unity  
 313 (1.001) and  $C_{(h-p\pi)_{\text{RSB}}}^{US}(\Delta\phi, \Delta\eta)$  is not used as our combinatorial background is negligible, thus the full  
 314 correlation equation simplifies to (1). However, the full correlation equation (2) is used in the systematic  
 315 uncertainty calculations (Section ??) as well as the  $h - \Lambda$  correlations where the  $\Lambda$  is reconstructed using  
 316 the resonance technique (Section ??).

### 317 5.2 Full h- $\Lambda$ and h-h Correlation Measurement

318 Using Equation ?? and the efficiencies calculated in Section ??, we can plot the 2D and 1D angular cor-  
 319 relations for both h- $\Lambda$  and h-h pairs, shown in Figures ?? through ??. Both the 2D and 1D correlations  
 320 are such that  $|\Delta\eta| < 1.2$ .

### 5.3 Extracting Near-side, Away-side, and Underlying Event Yields

Once the  $\Delta\phi$  distributions are calculated, they are separated into the three kinematic regions discussed in Section ???. While this can be done in a multitude of ways, the central points of this analysis were calculated using the following technique (with other techniques discussed in Section ??):

#### 6-bin underlying event technique:

- The underlying event region is defined using a straight-line fit of the average of bins (1, 2, 7, 8, 9, 16) in the  $\Delta\phi$  distribution
- The near-side yield is calculated via  $\sum_{i=1}^8 (\Delta\phi_{\text{bin } i} - \text{UE}_i)$ , where  $\text{UE}_i$  is the value of the straight-line fit at the center of the  $i$ th bin
- The away-side yield is calculated via  $\sum_{i=9}^{16} (\Delta\phi_{\text{bin } i} - \text{UE}_i)$ , where  $\text{UE}_i$  is the value of the straight-line fit at the center of the  $i$ th bin
- The underlying-event yield is calculated via  $\sum_{i=1}^{16} \text{UE}_i = 16 \times \text{UE}$
- The total-yield is calculated via  $\sum_{i=1}^{16} \Delta\phi_{\text{bin } i} = \text{near-side} + \text{away-side} + \text{underlying-event}$

The final per-trigger  $\Delta\phi$  distributions with the 6-bin UE fit for the  $h - \Lambda$  and  $h - h$  pairs in each multiplicity bin are shown in Figures ?? and Figure ??, respectively.

### 5.4 Per-trigger Pairwise Yields

The  $h - \Lambda$  and  $h - h$  near-side, away-side, and underlying-event per-trigger pairwise yields for each multiplicity bin are shown in Table ?? ( $h - \Lambda$ ) and Table ?? ( $h - h$ ). The errors reported are the statistical errors on the yields. The systematic errors are discussed in Section ??.

Multiplicity Bin	Near-side Jet	Away-side Jet	Underlying Event	Total
0-20%	$4.14\text{e-}03 \pm 1.35\text{e-}04$	$4.42\text{e-}03 \pm 1.88\text{e-}04$	$8.75\text{e-}02 \pm 3.84\text{e-}04$	$9.58\text{e-}02 \pm 2.45\text{e-}04$
20-50%	$3.50\text{e-}03 \pm 1.23\text{e-}04$	$3.27\text{e-}03 \pm 1.45\text{e-}04$	$4.69\text{e-}02 \pm 3.11\text{e-}04$	$5.36\text{e-}02 \pm 2.02\text{e-}04$
50-80%	$2.93\text{e-}03 \pm 1.61\text{e-}04$	$2.80\text{e-}03 \pm 2.06\text{e-}04$	$2.44\text{e-}02 \pm 3.89\text{e-}04$	$2.99\text{e-}02 \pm 2.66\text{e-}04$

**Table 3:** Per-trigger pairwise  $h - \Lambda$  extracted yields and corresponding statistical errors in the different kinematic regions for each multiplicity bin. The yields were extracted using the same procedure described in the previous section.

Multiplicity Bin	Near-side Jet	Away-side Jet	Underlying Event	Total
0-20%	$3.60\text{e-}01 \pm 8.23\text{e-}04$	$2.28\text{e-}01 \pm 9.29\text{e-}04$	$3.63\text{e+}00 \pm 1.88\text{e-}03$	$4.21\text{e+}00 \pm 1.23\text{e-}03$
20-50%	$3.48\text{e-}01 \pm 6.54\text{e-}04$	$2.08\text{e-}01 \pm 8.38\text{e-}04$	$2.18\text{e+}00 \pm 1.65\text{e-}03$	$2.73\text{e+}00 \pm 1.12\text{e-}03$
50-80%	$3.46\text{e-}01 \pm 1.02\text{e-}03$	$1.99\text{e-}01 \pm 1.15\text{e-}03$	$1.24\text{e+}00 \pm 2.12\text{e-}03$	$1.78\text{e+}00 \pm 1.60\text{e-}03$

**Table 4:** Per-trigger pairwise  $h - h$  extracted yields and corresponding statistical errors in the different kinematic regions for each multiplicity bin. The yields were extracted using the same procedure described in the previous section.

In order to investigate the multiplicity dependence of jet-like  $\Lambda$  production, the  $h - \Lambda$  and  $h - h$  near-side and away-side per-trigger pairwise jet yields are plotted in Figure ??. The  $h - \Lambda$  yield appears to increase with respect to multiplicity, whereas the  $h - h$  yield appears mostly flat.

### 5.5 Multiplicity Dependent Ratio Measurement

Once we have extracted the per-trigger pairwise yields from our  $h - \Lambda$  and  $h - h$  correlations, we are able to measure the ratio of yields of  $h - \Lambda/h - h$  pairs in each of the kinematic regions described in

the previous section—near-side of jet, away-side of jet, underlying event and total yield—as a function of multiplicity. This result of this can be seen in Figure ??.

Comparing the ratio in different kinematic regions as a function of multiplicity, we see a clear separation between the "jet-like" and "underlying event" components, with the underlying event seeing the largest  $\frac{h-\Lambda}{h-h}$  ratio in all multiplicity bins, whereas both the near-side and away-side ratios are lower than the total ratio for all multiplicity bins. We also see a clear separation between the near-side and away-side ratios, with the away-side ratio being higher than the near-side across all multiplicity bins. All kinematic region ratios see an increase with respect to multiplicity, but the underlying event ratio sees the smallest increase, while the away-side ratio sees the largest increase.

## 6 Systematic Errors

### 6.1 Systematics Overview

For all possible sources of systematic errors, the errors are first calculated per  $\Delta\phi$  bin in the full  $\Delta\phi$  distribution. This is done using a ratio of all variations to the standard cut and finding the overall RMS across all  $\Delta\phi$  bin. After this is done, each variation then undergoes the full yield extraction. The variation of the final yields is then calculated again as the RMS of all variations, giving a separate systematic error for the near-side, away-side, underlying-event, and total pair yield. For the final  $(h-\phi)/(h-h)$  pair ratios, the systematic errors from the individual  $(h-\phi)$  and  $(h-h)$  yields are treated as uncorrelated.

### 6.2 Systematic Error Sources

### 6.3 PID Cuts

### 6.4 Signal Region Selection

### 6.5 Background Subtraction

### 6.6 Correlation Fitting Procedure

## 7 Results and Comparisons

### 7.1 Per-trigger $h-\Lambda$ , $h-h$ $\Delta\phi$ Correlations

### 7.2 $h-\Lambda$ , $h-h$ Jet-like Yields

### 7.3 Multiplicity Dependent $h-\Lambda/(h-h)$ Ratios

### 7.4 Comparison to the $\phi(1020)$

### 7.5 Multiplicity Dependent $h-\Lambda/h-\phi$ Ratios

## 8 Cross Checks

### 8.1 Resonance Technique for $\Lambda$ Reconstruction

While using the V0 finder to reconstruct  $\Lambda$  baryons is the most common method, it is possible that the V0 finder algorithm introduces some topological biases in the  $\Lambda$  reconstruction, even when no further topological cuts are being applied to the V0 or its corresponding daughters. Because of this, we also investigate another method for reconstructing  $\Lambda$  baryons whereby all proton and pion pairs from the global AOD track list that pass the daughter cuts (Section ??) within an event are combined to reconstruct the  $\Lambda$ s. This method is referred to as the *resonance technique*, as it is the technique used to reconstruct short-lived particles that could otherwise not be reconstructed using the V0 finder.

### 8.1.1 Combinatorial Background Estimation

As  $\Lambda$  baryons reconstructed using the resonance technique will have a large combinatorial background, the final correlation will contain  $h - (p\pi)$  pairs that need to be removed. In order to remove this background, we need both an estimate of the correlation shape of the  $h - (p\pi)$  pairs, as well as an estimate of the Signal/Background in the  $\Lambda$  mass peak region.

The background shape of the  $\Lambda$  invariant mass distribution can be estimated using one of the following techniques:

- **Like-sign  $p\pi$  pairs** - Reconstruct the invariant mass of like-sign  $p\pi$  pairs, and scale the like-sign  $p\pi$  distribution to the un-like sign  $p\pi$  distribution in a region outside of the  $\Lambda$  signal region.
- **Rotated  $p\pi$  pairs** - Reconstruct the invariant mass of unlike-sign  $p\pi$  pairs, but rotate either the pion or proton around the z-axis by  $\pi$  radians, and scale the rotated  $p\pi$  distribution to the un-like sign  $p\pi$  distribution in a region outside of the  $\Lambda$  signal region.
- **Voigt + polynomial fit** - Perform a standard fitting procedure using TMath::Voigt for the signal along with a second-order polynomial for the background.

We will address the last technique (fitting procedure) first, as it fails to properly estimate the signal and background in data. To illustrate this, we can find the best possible fits in data and extract the corresponding signal shape to compare with the signal shape in MonteCarlo (with full track reconstruction). This comparison is done for our 20-50% multiplicity bin in Figure ??.

The MonteCarlo plot was generated using our standard MC sample, and applying the same techniques for  $\Lambda$  reconstruction described previously using the global AOD list. The background on the plot was generated by taking all  $p\pi$  pairs that did NOT come from a  $\Lambda$ , verified within the MC stack. While comparing data to MonteCarlo should be done with caution, it should also be pointed out that even extracting the  $\Lambda$  signal in MonteCarlo without a priori knowledge of the background shape is nontrivial and naive attempts result in severely underestimating the signal.

While it may be possible to get a proper handle on the background shape using the fitting procedure, all attempts by the author to do so have failed. Because of this, we will only consider the first two techniques for the rest of this analysis. To determine which of the two remaining techniques is more effective, we compare the background shape of the  $\Lambda$  invariant mass distribution for both techniques in MonteCarlo where we have direct access to the background shape. The like-sign and rotated  $p\pi$  pairs are shown along with the extracted signal comparison in Figure ?. The like-sign  $p\pi$  pairs match the background shape of the  $\Lambda$  invariant mass distribution more closely than the rotated  $p\pi$  pairs, so we use the like-sign  $p\pi$  pairs to estimate the combinatorial background in the  $\Lambda$  invariant mass distribution in data.

The region outside of the  $\Lambda$  signal region used for scaling the background estimates is called the Right SideBand region, or RSB. The choice of RSB has a large systematical effect on the background approximation as neither the like-sign nor rotated  $p\pi$  pairs match the background shape throughout the entirety of the distribution. The RSB region was chosen to minimize the difference in shape between the extracted signal in data (total - like-sign BG) and the resonance-technique reconstructed signal shape in MonteCarlo, generated from all  $p\pi$  pairs which guaranteed came from a  $\Lambda$ . The raw unlike-sign  $p\pi$  distribution for the 0-20% Multiplicity Percentile is shown in Figure ?, and the extracted signal and comparison with MonteCarlo is shown in Figure ?.

The resonance technique  $p\pi$  invariant mass distributions for each multiplicity bin are shown in Figure ?, and a table containing their yields, signal/BG and significance is shown in Table ?.



### 8.1.2 Invariant Mass Regions

The signal shape and background from  $\Lambda$ s reconstructed using the resonance technique is vastly different than those reconstructed using the V0 finder, thus it is necessary to define new invariant mass regions such that the signal can be properly extracted:

- unlike-sign  $p\pi$  in  $\Lambda$  mass region:  $1.014 \text{ GeV}/c^2 < M_{p\pi} < 1.026 \text{ GeV}/c^2$
- like-sign  $p\pi$  in  $\Lambda$  mass region:  $1.014 \text{ GeV}/c^2 < M_{p\pi} < 1.026 \text{ GeV}/c^2$
- unlike-sign  $p\pi$  in 0-20% multiplicity bin RSB:  $0.995 \text{ GeV}/c^2 < M_{p\pi} < 1.005 \text{ GeV}/c^2$
- unlike-sign  $p\pi$  in 20-50% multiplicity bin RSB:  $0.995 \text{ GeV}/c^2 < M_{p\pi} < 1.005 \text{ GeV}/c^2$
- unlike-sign  $p\pi$  in 50-80% multiplicity bin RSB:  $0.995 \text{ GeV}/c^2 < M_{p\pi} < 1.005 \text{ GeV}/c^2$

The signal regions were chosen to maximize significance and were not multiplicity dependent, whereas the RSB regions were chosen to minimize the difference in shape between the extracted signal in data (total - like-sign BG) and the resonance-technique reconstructed signal shape in MonteCarlo, generated from all  $p\pi$  pairs which guaranteed came from a  $\Lambda$ , as was demonstrated in Figure ???. This process was repeated for each multiplicity bin resulting in slight fluctuations of the RSB with respect to multiplicity.

For the resonance technique, the combinatorial background contribution to the correlation was removed using the like-sign  $p\pi$  distribution scaled to the RSB for each multiplicity bin, a procedure described with more detail in Section ???.

### 8.1.3 Efficiency Correction

To estimate the  $\Lambda$  reconstruction efficiency, we compare  $\Lambda$  yields reconstructed using the resonance technique to the true  $\Lambda$  yields using the MC production LHC17f2b.FAST (anchored to LHC16q.FAST production). The efficiency was calculated using the following formula:

$$\epsilon_{\Lambda} = \frac{N_{\Lambda, \text{ reco. with resonance technique}}}{N_{\Lambda, \text{ real MC yield}}},$$

where each  $\Lambda$  in  $N_{\Lambda, \text{ reco. with resonance technique}}$  is found in the following way:

- Find all protons and pions within the AOD list that pass our daughter cuts (Section ??, PID is done via MC label)
- For each proton in list, determine if it came from a  $\Lambda$  (via MC label)
- If proton came from  $\Lambda$ , loop through pions until we find one that came from same  $\Lambda$  (via MC label)
- Reconstruct the  $\Lambda_{\text{reco}}$  using the daughter AOD tracks
- Only keep  $\Lambda_{\text{reco}}$  if  $|\eta| < 0.8$

and each  $\Lambda$  in  $N_{\Lambda, \text{ real MC yield}}$  meets the following criteria:

- Found in the MC stack

–  $|\eta_\Lambda| \leq 0.8$

– The  $\Lambda$  decays to  $p\pi$

As the resulting invariant mass signal from  $N_{\Lambda, \text{ reco. with resonance technique}}$  is much wider than the signal from the V0 finder technique (Figure ??), the efficiency calculation is taken using the entire invariant mass range and the correction for our finite signal region is applied later (see Section ??).

While previous analyses focus solely on primary  $\Lambda$ s (excluding  $\Omega$  and  $\Xi$  contamination), there is no requirement for either the V0-reconstructed  $\Lambda$  or the MC-generated  $\Lambda$  to be a primary particle. As this analysis is mostly interested in the  $\Lambda$  due to its strange quark content, whether or not the  $\Lambda$  came from a cascade decay is irrelevant. This is important to note when making comparisons between this analysis and previous analyses, as secondary contamination from cascades accounts for nearly 20% of all  $\Lambda$ s.

As mentioned in Section ??, both the  $\Lambda$  and the  $\bar{\Lambda}$  were combined together for this efficiency calculation. Efficiencies were calculated as a function of  $p_T$ ,  $\eta$ ,  $\phi$ , Event Z vertex, and Multiplicity. However, the final efficiency correction was applied as a function of  $p_T$  only and can be seen in Figure ??.

The  $h - \Lambda$  pairwise efficiency correction is applied in the same way as described in Section ??.

#### 8.1.4 Mixed Event Acceptance Correction

The procedure for correcting for finite detector acceptance in our angular correlations is exactly the same as the one described in Section ??.

#### 8.1.5 Removal of Combinatorial $p - \pi$ Background

Since we do not know which  $p - \pi$  pairs came from a real  $\Lambda$  decay, we must remove the contribution to the angular correlation structure due to the combinatorial background of  $p - \pi$  pairs that did not come from a  $\Lambda$ .

To do this,  $h - (p\pi)$  angular correlations are measured for unlike-sign  $p\pi$  pairs within the right sideband (RSB) for each multiplicity bin. The correlation structure in the RSB is then normalized to its integral to give an estimate of the combinatorial background shape, as the RSB should contain little-to-no  $p\pi$  pairs that came from a  $\Lambda$ . The self-normalized 1D  $\Delta\phi$  distributions for different choices of RSB regions are shown in Figure ?. As the shapes are similar for each choice of RSB, we conclude that there is no substantial contribution from  $p\pi$  pairs coming from  $\Lambda$  decay.

For the remainder of this resonance technique analysis we will be using  $1.16 < M_{RSB} < 1.18$  as our choice of RSB region for each multiplicity bin.

Next, the  $h - p\pi$  angular correlation in our chosen sideband region is scaled to match the integral of our background in our signal region. However, this scaling is not performed directly as while the Signal/Background and Signal/(Signal + Background) ratios are the same for the single-particle  $\Lambda$  distribution and its corresponding invariant mass axis in our  $h - \Lambda$  distribution, the total yields are different. We therefore scale the  $h - p\pi$  distribution in the RSB to the BG integral in our signal region found using the following formula:

$$h - p\pi \text{ Combinatorial BG} = (\text{Integral of } h - p\pi \text{ in Signal Region}) \times \left(1 - \frac{S}{S+B}\right), \quad (3)$$

where  $S$  and  $B$  are calculated in the Signal region using the single-particle  $\Lambda$  distributions from Table ??.

Once the  $h - p\pi$  angular correlation in the RSB is scaled to match the  $h - p\pi$  Combinatorial BG, it is subtracted from the total  $h - p\pi$  distribution in our signal region, then scaled to correct for our finite signal region. This scale factor is calculated using the following formula:

$$s_{\text{finite region}} = (\text{Integral of residual in signal region} / \text{Total integral of residual})^{-1} \quad (4)$$

Once the scale factor is applied, we are then left with the full  $h - \Lambda$  2D angular correlations and corresponding 1D  $\Delta\phi$  projections, shown in Figures ?? and ??, respectively.

### 8.1.6 Near-side, Away-side and Underlying Event Yield Extraction

The procedure for extracting the near-side, away-side and underlying event yields is exactly the same as the one described in Section ?. However, due to the statistical fluctuations introduced by the combinatorial background subtraction, we will be limiting the underlying event fitting procedure to the “6-bin average” method. The final  $\Delta\phi$  correlations with their corresponding underlying event fits can be seen in Figure ?. The extracted per-trigger yields and corresponding errors are shown in Table ?.

Multiplicity Bin	Near-side Jet	Away-side Jet	Underlying Event	Total
0-20%	$4.21\text{e-}3 \pm 0.38\text{e-}3$	$5.07\text{e-}3 \pm 0.54\text{e-}3$	$1.01\text{e-}1 \pm 0.01\text{e-}1$	$1.11\text{e-}1 \pm 0.07\text{e-}1$
20-50%	$3.66\text{e-}3 \pm 0.31\text{e-}3$	$3.58\text{e-}3 \pm 0.35\text{e-}3$	$5.34\text{e-}2 \pm 0.07\text{e-}2$	$6.05\text{e-}2 \pm 0.05\text{e-}2$
50-80%	$3.40\text{e-}3 \pm 0.31\text{e-}3$	$3.62\text{e-}3 \pm 0.40\text{e-}3$	$2.51\text{e-}2 \pm 0.08\text{e-}2$	$3.21\text{e-}2 \pm 0.05\text{e-}2$

**Table 5:** Per-trigger pairwise  $h - \Lambda$  extracted yields and corresponding errors in the different kinematic regions for each multiplicity bin. The yields were extracted using the same procedure described in Section ?.

### 8.1.7 Results and Comparison with V0 Technique

The final  $h - \Lambda/h - h$  ratio vs. multiplicity plot for  $\Lambda$ s reconstructed using the resonance technique is shown in Figure ?. The per-trigger near and away-side pairwise yields vs. multiplicity for the  $h - \Lambda$  and  $h - h$  distributions are shown in Figure ?.

A comparison of the final per-trigger  $h - \Lambda \Delta\phi$  correlation structure for the resonance and V0 techniques can be seen in Figure ?. The correlation shapes are nearly identical, with the resonance technique having slightly larger uncertainties due to the combinatorial background subtraction. While this is not surprising (a  $\Lambda$  is a  $\Lambda$ , regardless of how it is reconstructed), it serves as a powerful cross check to our central values from the V0 technique.

## 8.2 MonteCarlo Closure Tests

### 8.3 Fit of $\Delta\phi$ Correlation Structure

In order to measure the yields within the near- and away-side jet, the angular correlation must first be fit with a function that allows for the separation of jet-like and underlying event components. For this, the 2D correlation function is projected onto  $\Delta\phi$  for the range  $-1.2 < \Delta\eta < 1.2$  due to statistics limiting the ability to fit the full 2D correlation. Several methods were used to estimate the “underlying event” component of the  $\Delta\phi$  correlation (see Section ?). For the 1D fit in  $\Delta\phi$  space, the following fit function was chosen:

$$\text{Fit}(\Delta\phi) = C + A_{\text{near}} * \exp\left(\frac{(\Delta\phi - M_{\text{near}})^2}{2 * \sigma_{\text{near}}}\right) + A_{\text{away}} * \exp\left(\frac{(\Delta\phi - M_{\text{away}})^2}{2 * \sigma_{\text{away}}}\right) + \text{periodicity} \quad (5)$$

where periodicity is taken into account by also including a gaussian with the same parameters as the near and away-side peaks but at offset intervals of  $2\pi$ . Both the  $h - \phi$  and  $h - h$  correlations are fit with this method (fig. ??).

#### 8.4 Estimate of Near and Away-side Yields

Once the fit of the 1D  $\Delta\phi$  angular correlations is performed, the constant component of the fit is used to estimate the non-jet yield of correlated pairs. The near-side (away-side) yields are then the integral of the correlation distribution above this fit constant for the  $-\pi/2$  to  $\pi/2$  ( $\pi/2$  to  $3\pi/2$ ) region of  $\Delta\phi$  space (fig. ??).

These yields are calculated for the different multiplicity bins in both the near and away-side peaks, as well as the total yield of correlated pairs for both the  $h - \phi$  and  $h - h$  correlations.

### 9 Multiplicity Dependent Ratio Measurement

## 10 Monte Carlo Studies

### 10.1 Correlation Method Test using Monte Carlo

In order to test whether the full correlation measure (eq. ??) accurately describes the real  $h - \phi$  correlation, several Monte Carlo studies were performed. The first of these was a complete test of the correlation extraction method without detector inefficiencies. To accomplish this test, two correlations were measured in MC dataset LHC17f2b\_FAST with the same set of high  $p_T$  ( $4 < p_T < 8 \text{ GeV}/c$ ) trigger hadrons. The first used an associated particle taken from the MC generated  $\phi$  mesons (identified via MC particle's associated PDG code), representing the real  $h - \phi$  correlation. The second used the correlation method described in Section 4 to reconstruct the  $h - \phi$  correlation, using the MC generated Kaons identified via MC particle's PDG code instead of track PID cuts.

Comparing the generated vs. reconstructed correlation in  $\Delta\phi$  shows very good agreement, proving that the background subtraction method using the invariant sideband regions is sound (fig. ??).

### 10.2 MC Closure Test

After the MC method test showed that the general measurement method was correctly recovering the generated  $h - \phi$  correlations, a full MC closure test was performed using LHC17f2b\_FAST and LHC17f2b\_CENT datasets. The generated correlation was taken the same way as the above method test. For the reconstructed case, the full analysis procedure was used including tracking efficiency (Sec. ??). The reconstructed  $\Delta\phi$  distribution was then compared to the generated distribution (Fig. ??). A ratio of the two distributions fit with a straight line gives a closure of  $0.98 \pm 0.04$ , consistent with 1.

## 11 Systematic Errors & Crosschecks

### 11.1 (

)

### 11.2 TOF Efficiency Crosscheck

Since the TOF does not have uniform coverage in  $\phi$  and  $\eta$ , a crosscheck was necessary to ensure that the strict TOF PID signal was not influencing the final correlation measurement. The correlation was performed separately for associated particles that fell in the angular range  $0 < \phi_{assoc} < \pi$  (with gap in TOF coverage), and in the angular range  $\pi < \phi_{assoc} < 2\pi$  (no gap in TOF coverage).

These two correlations were then normalized to 1 to account for the different statistics and plotted against one another. Within statistical errors, there was no difference between the correlations from one side of the detector and the other, showing that there was no effect on the final correlation shape due to the gap in TOF coverage.

### 11.3 Invariant Mass Range Checks

In order to test the systematic effects of the correlation method (i.e. choosing specific narrow mass regions for the "mass peak", as well as for the "side band" regions for background estimation), it is necessary to vary the width and positions of these regions and see the effect on the final correlation results.

#### 11.3.1 Mass Peak Region Check

The mass peak range can be varied by widening and narrowing the  $\phi(1020)$  signal mass region considered. Since this directly changes the Signal/Background of the uncorrected correlation, this variation tests whether or not the Signal/Background of the considered region has an effect on the final correlation even after the fraction of total signal that is excluded is taken into account (i.e. the correlation is corrected by the factor  $k_{\text{Signal}}$  from Eq. ??, which changes with the mass window used).

Within the range variation considered, we see no significant effect on the correlation function (fig. ??) due to the changing Signal/Background ratio. The ratio of each cut to the standard is also plotted, and found to be uniform in  $\Delta\phi$  and consistent with 1. We also project all ratio points for each  $\Delta\phi$  bin onto a single distribution (fig. ??) to find an RMS value of 1.4%, well below the statistical error of the distribution.

#### 11.3.2 Sideband Region Check

The sideband regions of the invariant mass distribution are used for both estimating the correlation background under the mass peak, as well as for the like-sign scaling factor. In order to make sure the choice of sideband region does not significantly change the final correlation structure, both the left and right sideband regions were varied from their standard ranges (fig. ?? & ??). In both cases, variation of the sideband region shows no significant changes to the correlation distribution, with any differences well below the statistical errors of the correlation.

#### 11.3.3 Likesign Sideband Scaling Factor Check

To estimate the Signal/Background ratio in the  $\phi(1020)$  mass peak region, the like sign invariant mass distribution is scaled to the integral of the unlike sign sideband regions. Since this scaling factor is influenced both by the statistics of the integral (of both the like and un-like sign distributions), as well as the specific sideband mass ranges, the choice of scaling was varied between the following options:

- Right Sideband only
- Right Sideband + Statistical Error
- Right Sideband - Statistical Error
- Left Sideband only
- Left Sideband + Statistical Error
- Left Sideband - Statistical Error
- Average of Left and Right Sideband

**Fig. 55:** Pro  
from the va

– Average + Statistical Error

– Average - Statistical Error

The "Average" case is taken to be the central value, and the ratio to the variations to the central correlation is plotted as a function of  $\Delta\phi$  (fig. ??). Combining the ratios at each point into a single distribution (fig. ??) gives an RMS value of 2%. Since this scaling factor directly shifts the correlation function up or down, the variation cannot be ignored even with the larger statistical errors, and must be accounted for in the final systematic errors.

#### 11.4 Correlation Fitting Procedure

Since there are several different methods of separating the "underlying event" from the jet peaks in the  $\Delta\phi$  correlation, a systematic check is needed to see if the final ratios are dependent on the method chosen. The correlation consists of 16 bins in  $\Delta\phi$ , and the underlying event can be estimated by looking at those bins that are farthest from the near and away jet peaks:

ection of the ratio of all  $\Delta\phi$  points from fig. ?? onto a single distribution shows a variation due to the scaling factor used (RMS of 2.0%)

– Average of bins 1, 8, 9

– Average of bins 1, 2, 7, 8, 9, 16

– Full Correlation Fit (straight line as free parameter)

For the "Full Correlation Fit", the whole distribution is fit with two gaussians (the near and away-side peaks) and a straight line component. After the full fit converges, only the straight line parameter is extracted and used as the "underlying event".

For our final systematic, we take the RMS value of the distribution of ratios given from each of the listed BG estimation procedures (fig. ??). This gives us the following related systematic for the near-side, away-side, and UE:

#### 11.5 PID cuts

With a relatively wide PID cut, we need to check that the inclusion of pion contamination does not effect our final correlation structure. To do this, the TPC PID cut was varied from the standard cut of  $|n\sigma_{TPC}| < 3$  to 2.8, 2.6, 2.4, 2.2 and 2.0.

8: Plot showing the variation in the yield ratios for the different flat background assumptions

#### 11.6 Affect of $v_2$ Assumption on Ratios

Since the near and away-side peak (and underlying event) yields are calculated based on the assumption of a flat background underneath the jets, an additional check is needed to see if the inclusion of a  $v_2$  term changes the final  $(h-\phi)/(h-h)$  ratios. Since a published value for  $\phi$   $v_2$  in p-Pb was not available, we chose to use the published values for inclusive charged hadrons to estimate a systematic error. Using the published ALICE values (<https://doi.org/10.1016/j.physletb.2013.08.024>) gives us a  $v_2$  in the 0-20% bin of 0.15, while the 20-50% and 50-80% values are taken as 85% and 50% of the high multiplicity value, respectively.

By computing the pair yields using the non-zero  $v_2$  values, we can compare the effect on the  $(h-\phi)/(h-h)$  ratio measurement to our flat background assumption. Since the  $(h-h)$  and  $(h-\phi)$  correlations are treated with the same charge particle  $v_2$ , the overall effect on the ratio is a slight decrease in the jet yields at high multiplicity. On the other hand, since the non-jet component is so dominant within our correlation momentum ranges, the non-zero  $v_2$  does not have a visible effect on the Underlying Event ratio.

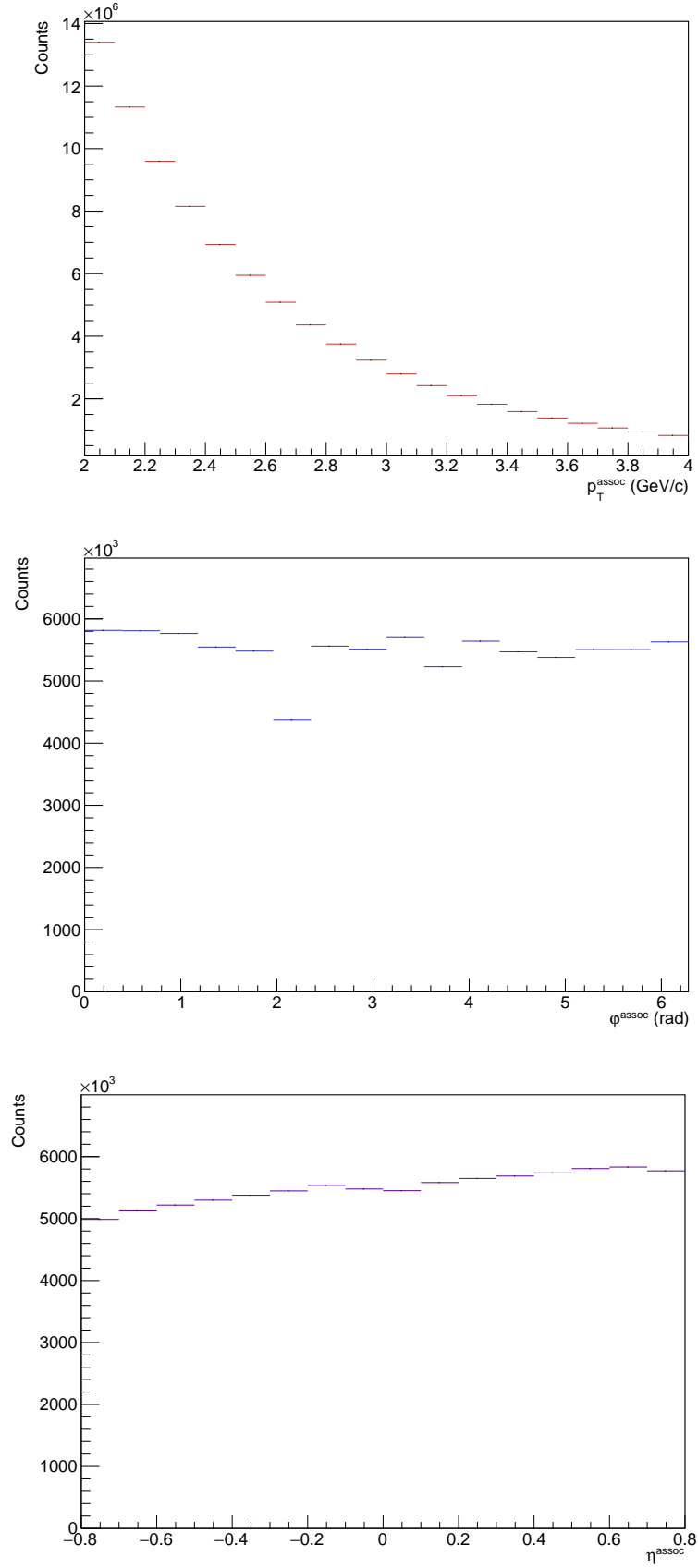


**Fig. 2:** The  $p_T$  (top),  $\phi$  (center) and  $\eta$  (bottom) distributions for the associated hadrons in the multiplicity range 0-20%.

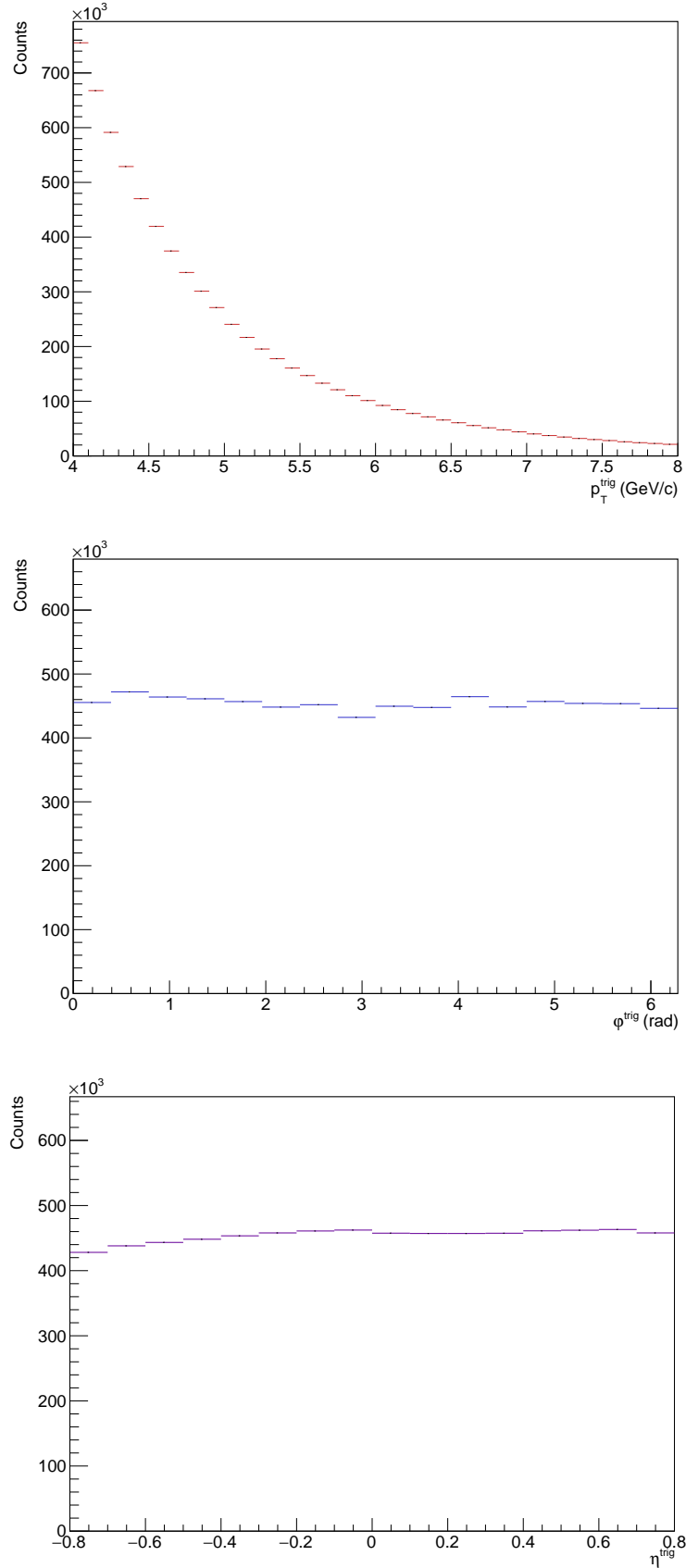


**Fig. 3:** The  $p_T$  (top),  $\phi$  (center) and  $\eta$  (bottom) distributions for the trigger hadrons in the multiplicity range 0-20%. Note that the  $\phi$  and  $\eta$  distributions are uniform, indicating no geometric biases from track selection (TPC sector bounds, etc.) will be introduced into the angular correlations.



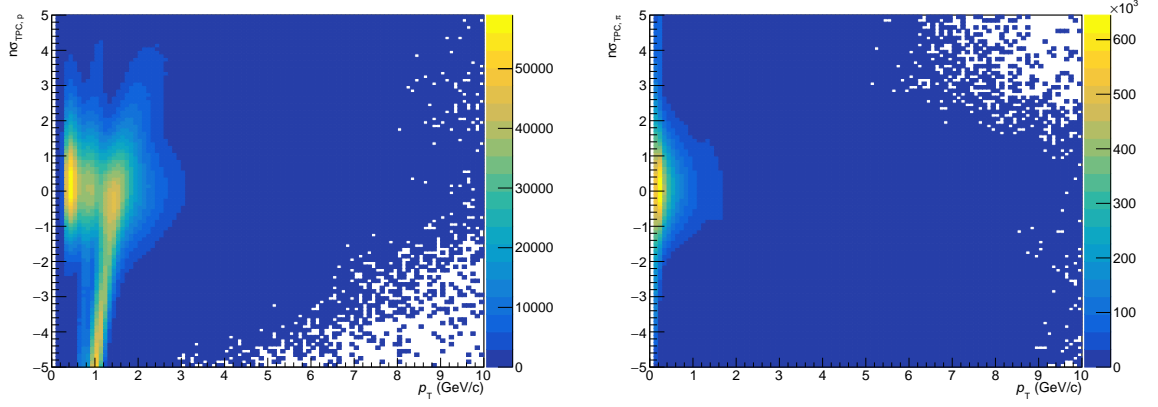


**Fig. 4:**  $n\sigma$  for protons (left) and pions (right) in the TPC detector as a function of  $p_T$ . A wider PID cut is used for the pion to maximize the  $\Lambda$  signal.

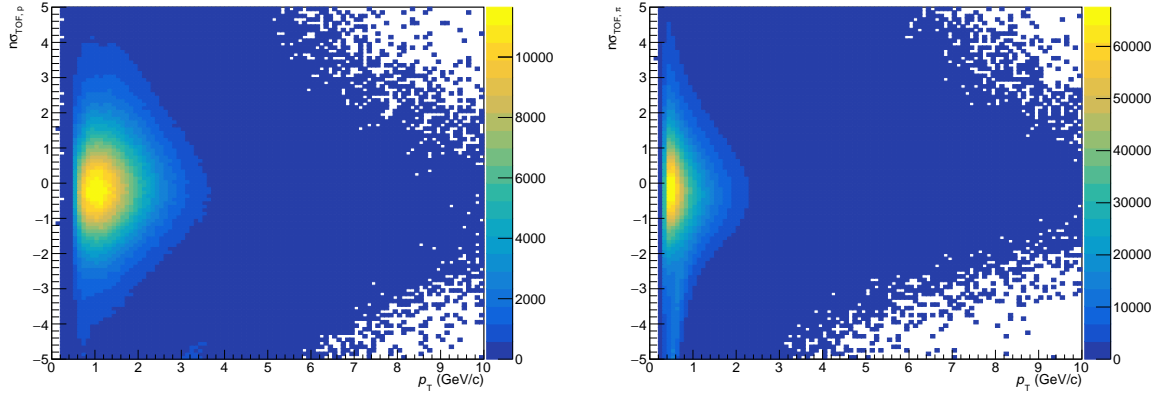


**Fig. 5:**  $n\sigma$  for pions (left) and protons (right) in the TOF detector as a function of  $p_T$ . If there is no TOF signal for the track, the TOF PID cut is not applied.

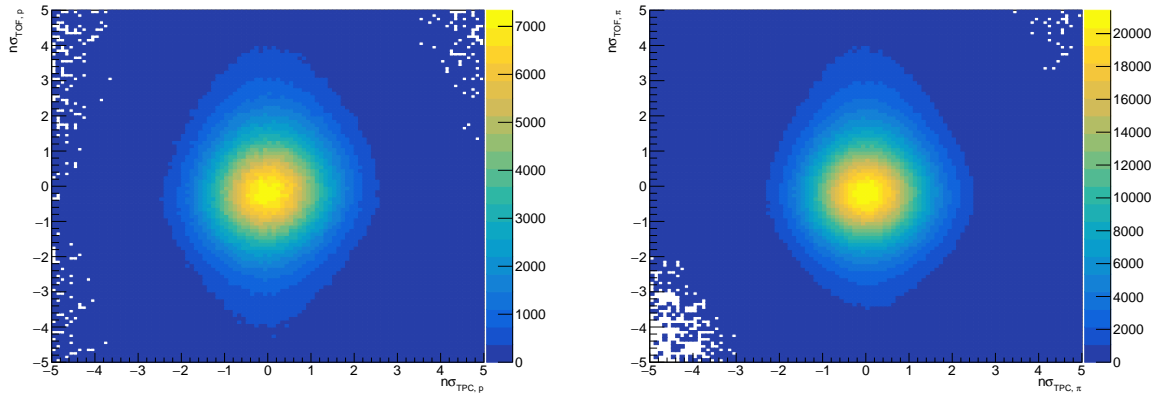


**Fig. 6:**  $n\sigma$  in TOF vs  $n\sigma$  in TPC for protons (left) and pions (right). No contamination is observed for both of the particle species.

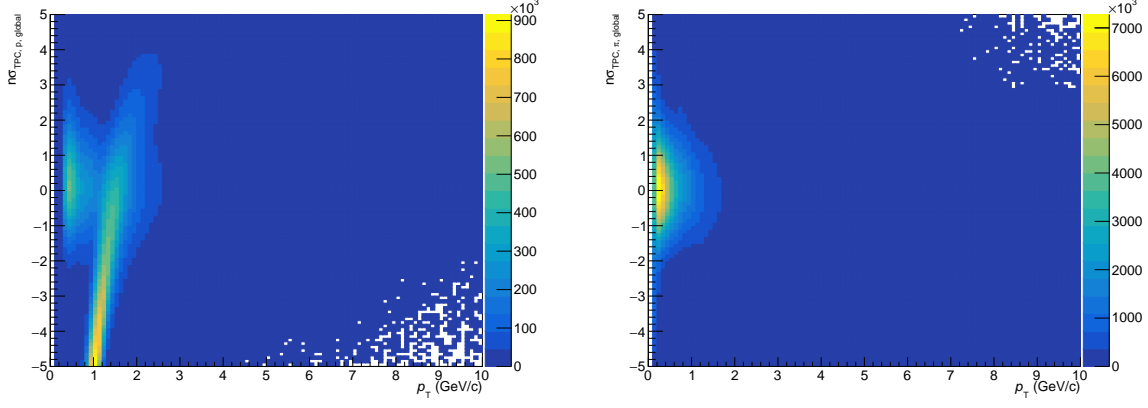


**Fig. 7:**  $n\sigma$  for protons (left) and pions (right) from the global AOD track list in the TPC detector as a function of  $p_T$ . These plots are very similar to those generated from V0 daughter tracks, so we conclude no PID biases are introduced from the V0 finder method.

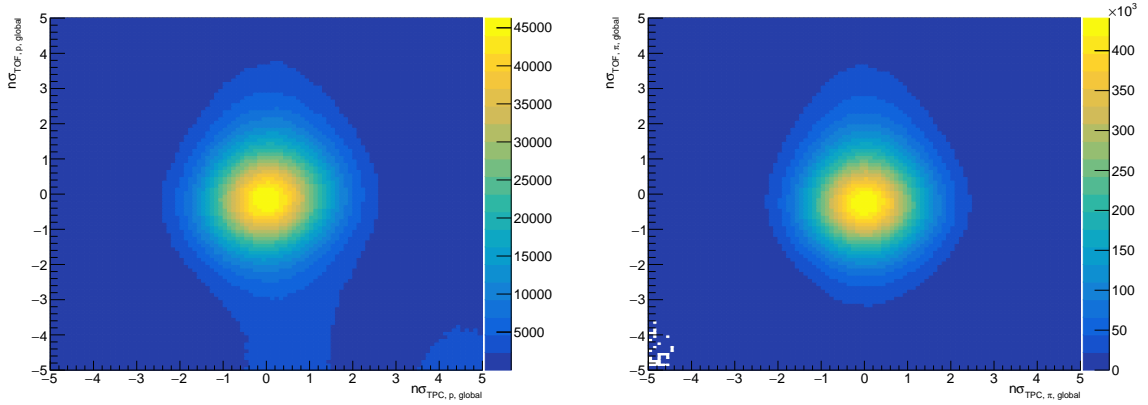


**Fig. 8:**  $n\sigma$  for protons (left) and pions (right) from the global AOD track list in the TOF detector as a function of  $p_T$ . Little to no contamination is observed.

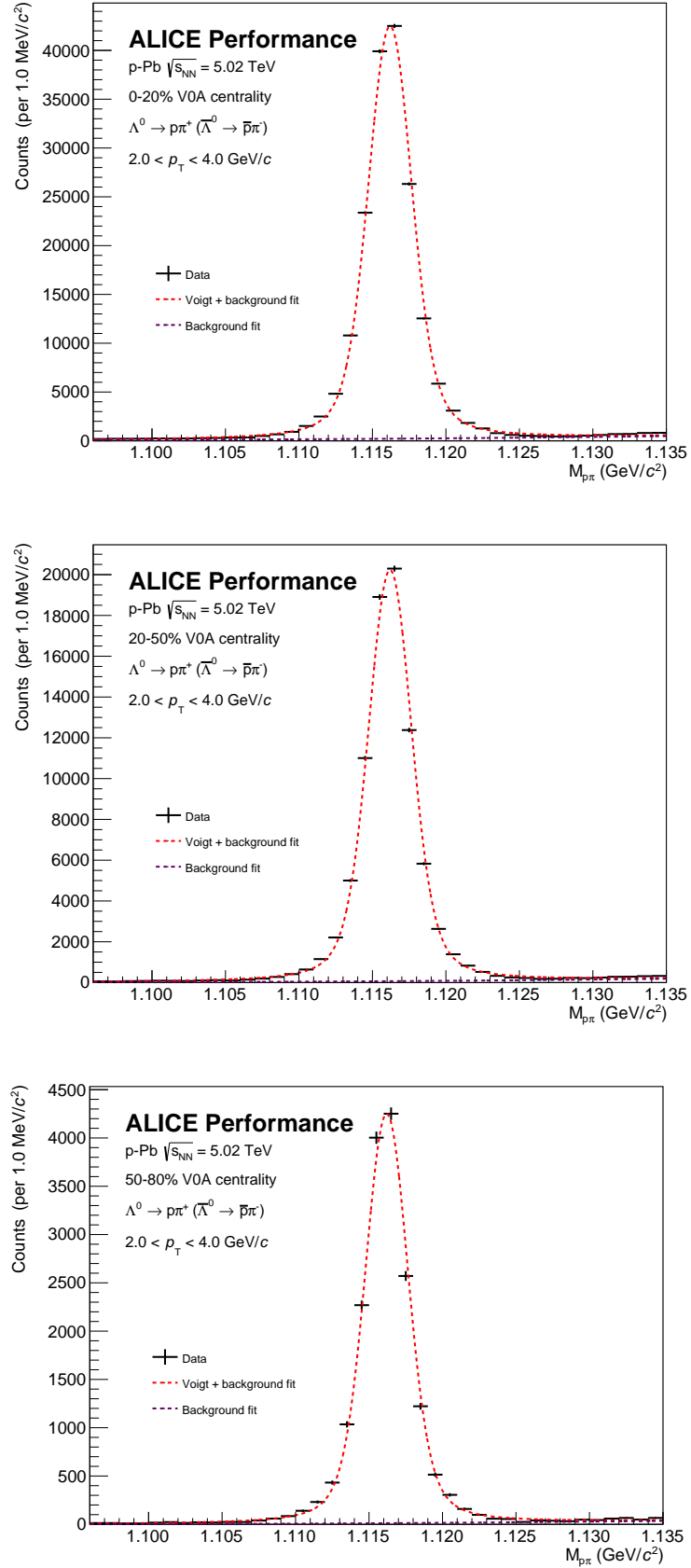


**Fig. 9:** Invariant mass distributions in the 0-20% (top), 20-50% (center), and 50-80% (bottom) multiplicity bins for  $\Lambda$ s reconstructed using the V0 finder with  $2 < p_T < 4$ . The background from misidentified  $\Lambda$ s is negligible for all multiplicity bins, despite no topological cuts being applied to the V0s.

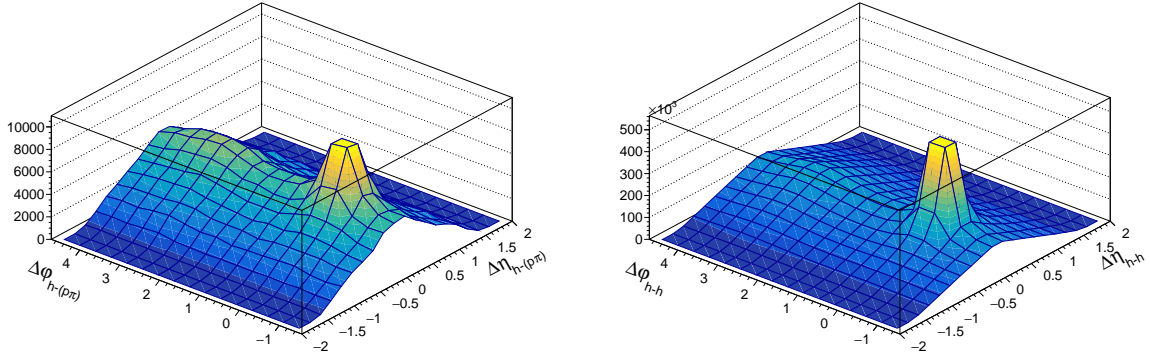


**Fig. 10:** 2-D non-acceptance corrected h- $p\pi$  (left) and h-h (right) angular correlations for the 0-20% multiplicity bin (all z-vertex bins merged together)

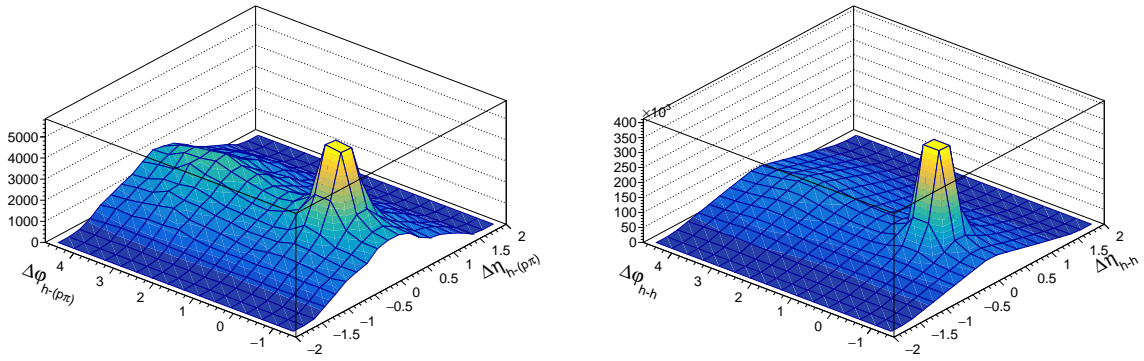


**Fig. 11:** 2-D non-acceptance corrected h- $p\pi$  (left) and h-h (right) angular correlations for the 20-50% multiplicity bin (all z-vertex bins merged together)

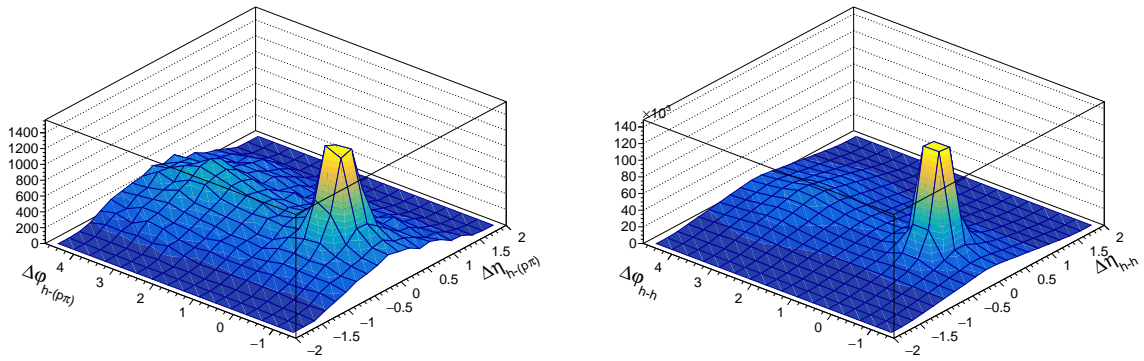


**Fig. 12:** 2-D non-acceptance corrected h- $p\pi$  (left) and h-h (right) angular correlations for the 50-80% multiplicity bin (all z-vertex bins merged together)

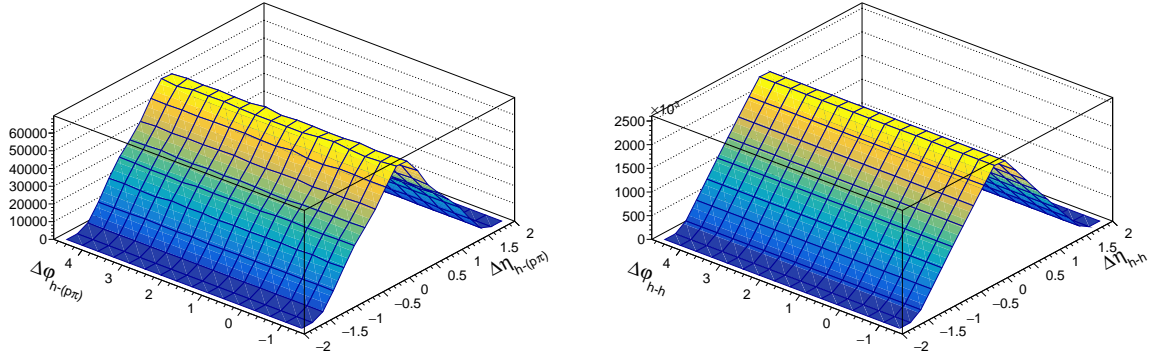


**Fig. 13:** 2-D mixed event  $h-p\pi$  (left) and  $h-h$  (right) angular correlations for the 0-20% multiplicity bin (all z-vertex bins merged together)

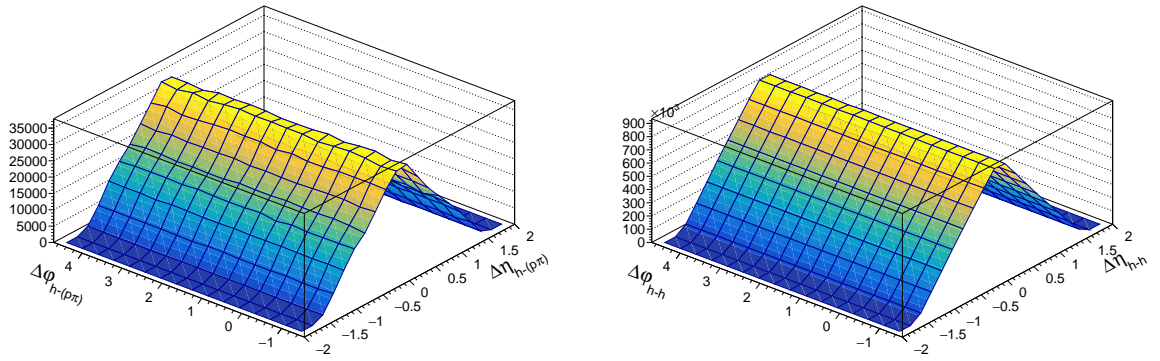


**Fig. 14:** 2-D mixed event  $h-p\pi$  (left) and  $h-h$  (right) angular correlations for the 20-50% multiplicity bin (all z-vertex bins merged together)

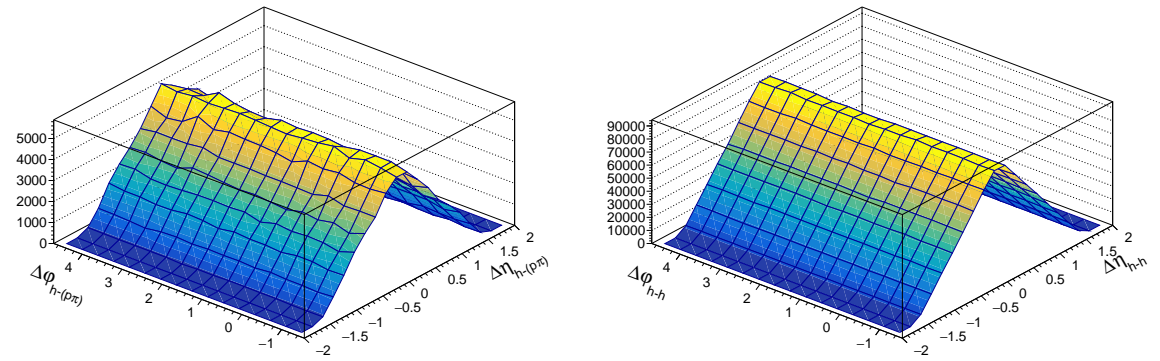


**Fig. 15:** 2-D mixed event  $h-p\pi$  (left) and  $h-h$  (right) angular correlations for the 50-80% multiplicity bin (all z-vertex bins merged together)

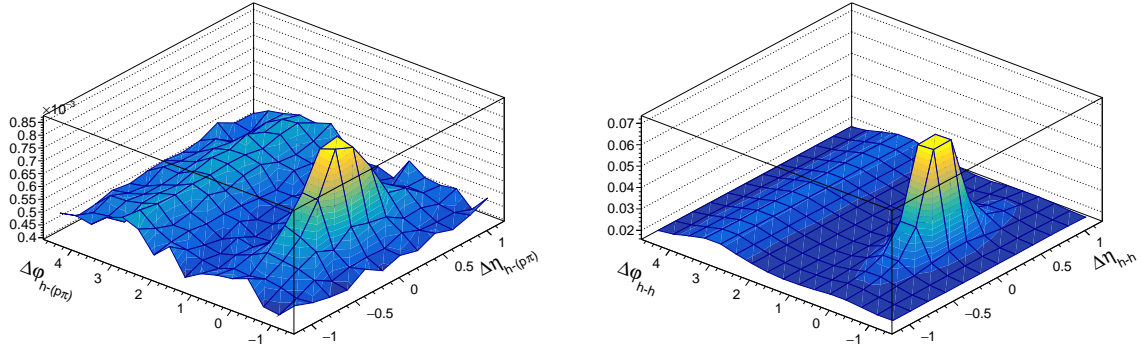


**Fig. 16:** Per-trigger 2-D  $h$ - $p\pi$  (left) and  $h$ - $h$  (right) angular correlations for the 0-20% multiplicity bin after acceptance corrections. Note that the triangular shape in  $\Delta\eta$  is no longer present.

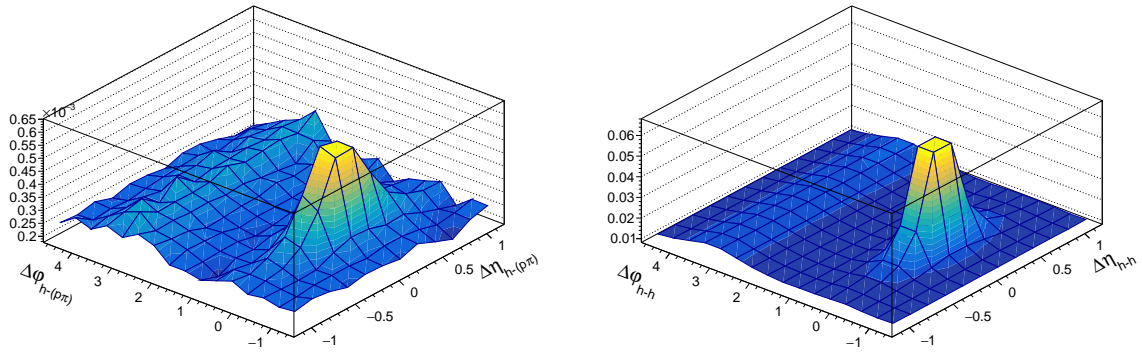


**Fig. 17:** Per-trigger 2-D  $h$ - $p\pi$  (left) and  $h$ - $h$  (right) angular correlations for the 20-50% multiplicity bin after acceptance corrections. Note that the triangular shape in  $\Delta\eta$  is no longer present.

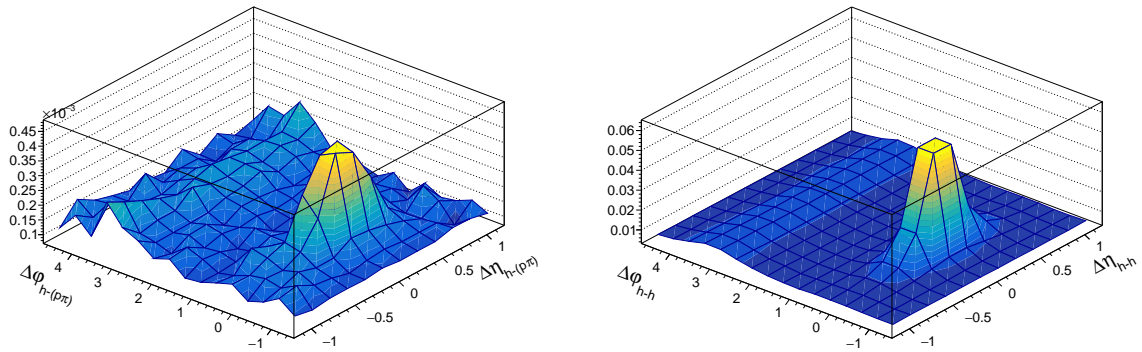


**Fig. 18:** Per-trigger 2-D  $h$ - $p\pi$  (left) and  $h$ - $h$  (right) angular correlations for the 50-80% multiplicity bin after acceptance corrections. Note that the triangular shape in  $\Delta\eta$  is no longer present.

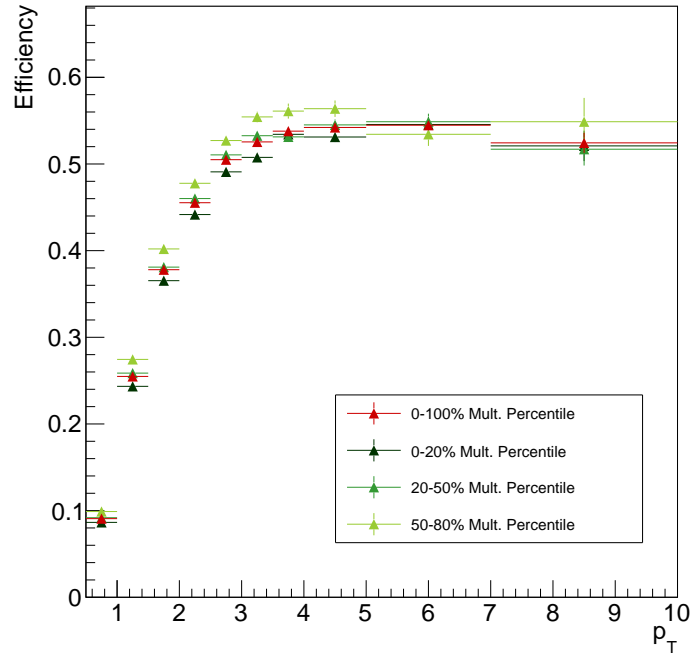


**Fig. 19:** Efficiency vs.  $p_T$  for  $\Lambda$  reconstruction for each multiplicity bin, along with an integrated 0-100% point in red. There does not appear to be any significant dependence on multiplicity.

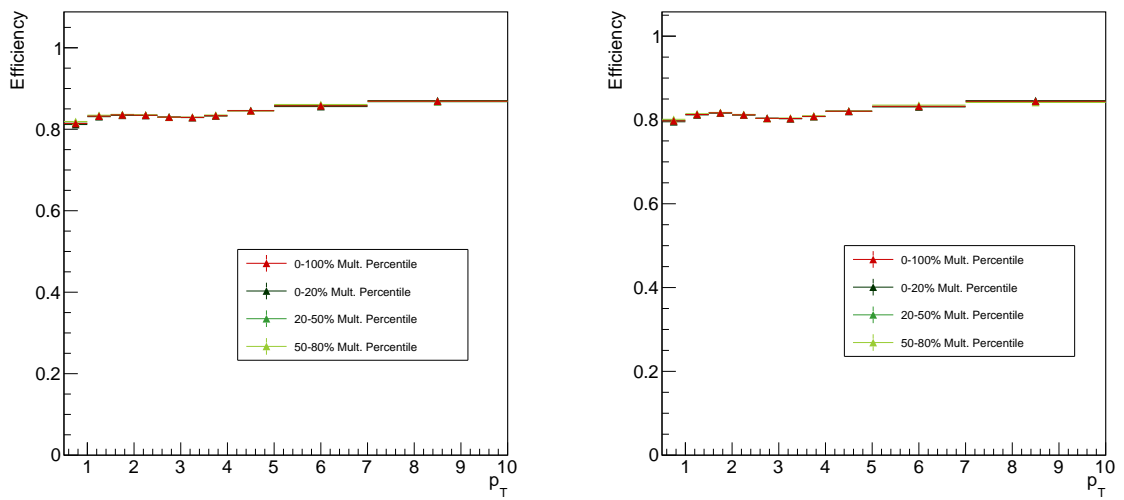


**Fig. 20:** Efficiency vs.  $p_T$  for trigger (left) and associated (right) hadrons. Both are slightly above 80% for the entire  $p_T$  range.



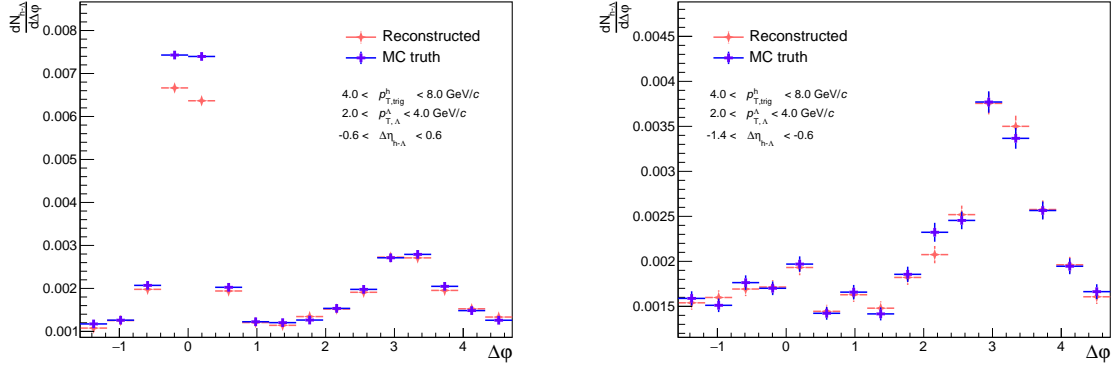


**Fig. 21:** Demonstration of the track merging effect for  $h - \Lambda$  pairs, whereby we see a dip in the reconstructed distribution at small  $\Delta\phi$  and  $\Delta\eta$  when compared to the MC ground truth (left). This dip is not present at large  $\Delta\eta$  (right), but we also lose nearly the entirety of our near-side peak.



**Fig. 22:** The reconstructed and ground truth  $\Delta\eta\Delta\phi$  distributions for h-(secondary protons) (left) and h-(primary protons) (right). The suppression at smaller  $\Delta\eta, \Delta\phi$  is clearly seen in the secondary case, but is not observable in the primary case.





**Fig. 23:** The (same-event/mixed-event)  $\Delta\eta\Delta\phi$  distribution ratios for h-(secondary protons) (left) and h-(primary protons) (right). The suppression at smaller  $\Delta\eta, \Delta\phi$  is clearly seen in the secondary case, but is not observable in the primary case.

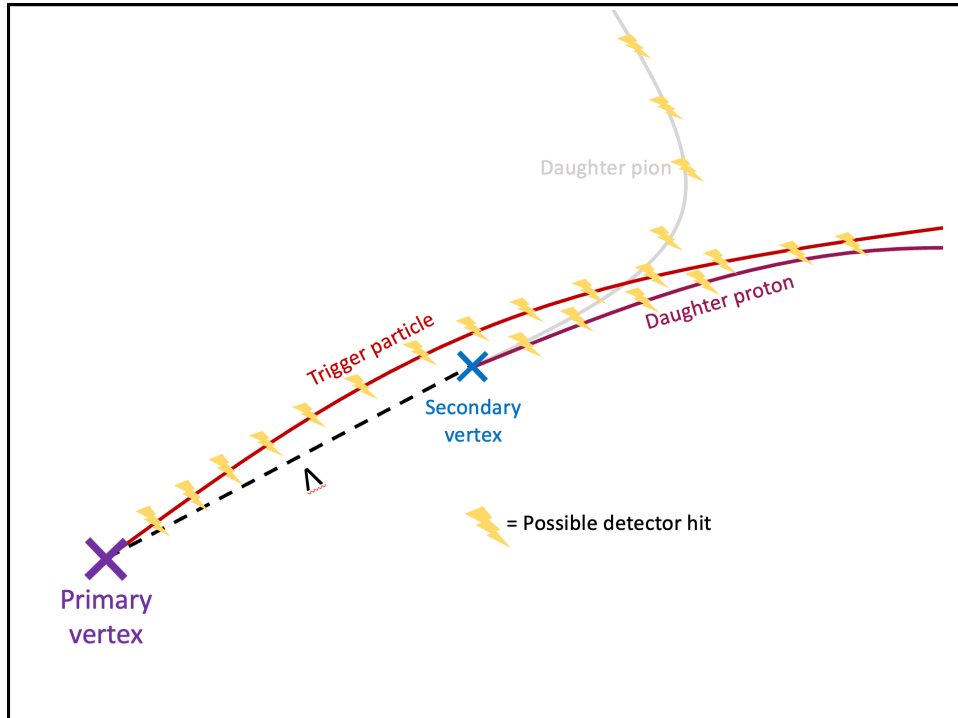


**Fig. 24:** Simple diagram depicting why track merging occurs: The  $\Lambda$  daughter proton has fewer possible hits in the detector, and is physically close to the trigger particle. When the tracks are being reconstructed, the proton track is “merged” over by the trigger track as the Kalman filtering process favors the track with more hits.

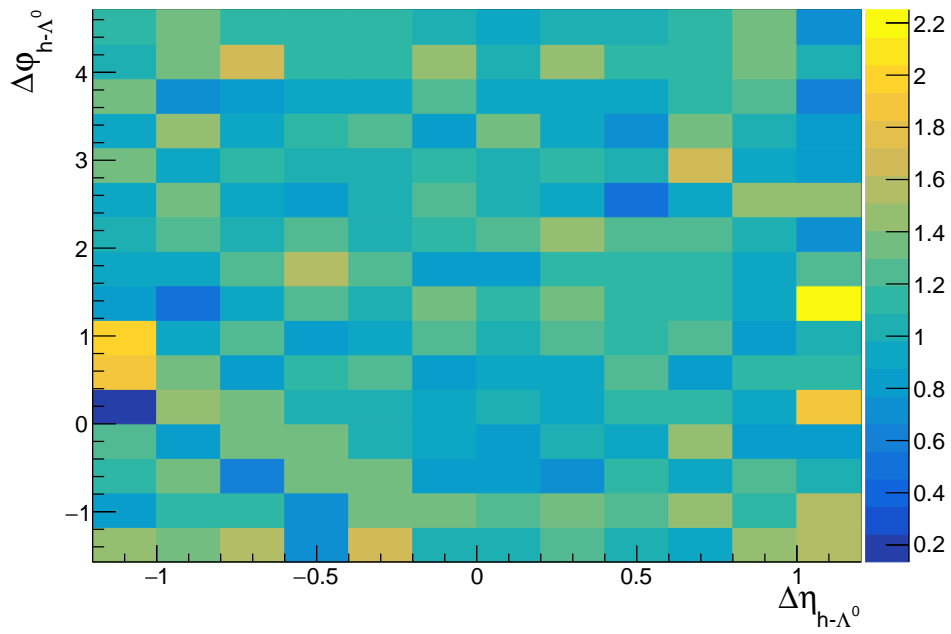


**Fig. 25:** Efficiency template for track merging correction.

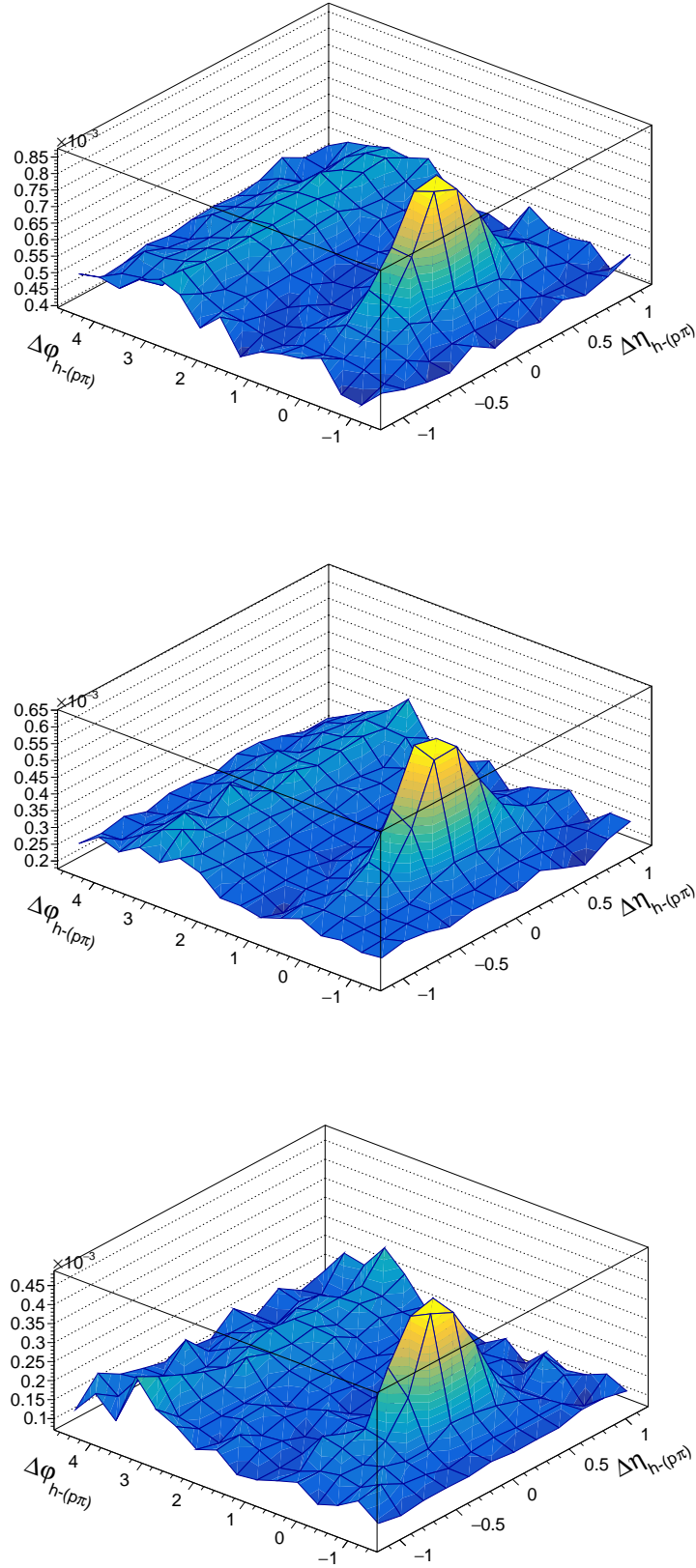


**Fig. 26:** Per-trigger normalized 2D angular correlations for h- $\Lambda$  pairs in the 0-20% (top), 20-50% (center) and 50-80% (bottom) multiplicity bins.

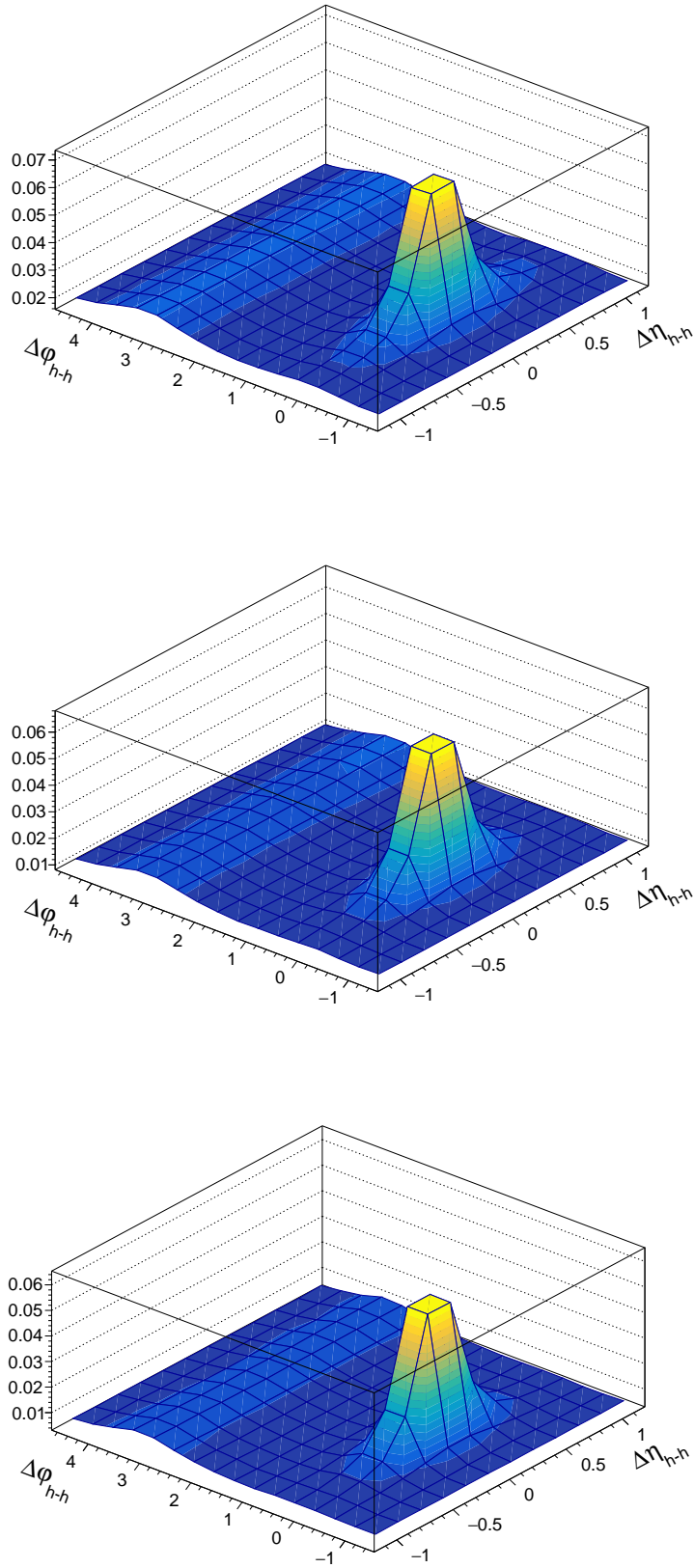


**Fig. 27:** Per-trigger normalized 2D angular correlations for h-h pairs in the 0-20% (top), 20-50% (center) and 50-80% (bottom) multiplicity bins.

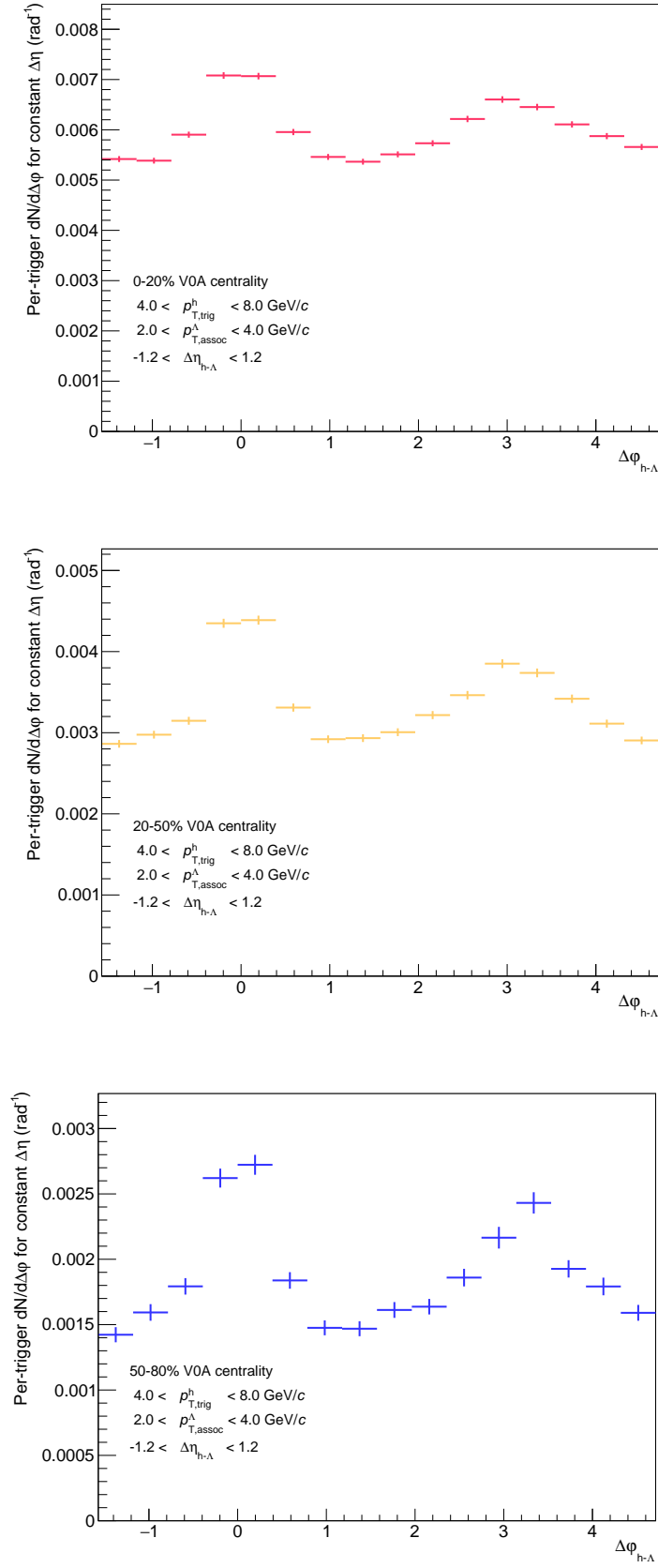


**Fig. 28:** Per-trigger normalized  $\Delta\phi$  correlations for  $h$ - $\Lambda$  pairs in the 0-20% (top), 20-50% (center) and 50-80% (bottom) multiplicity bins.

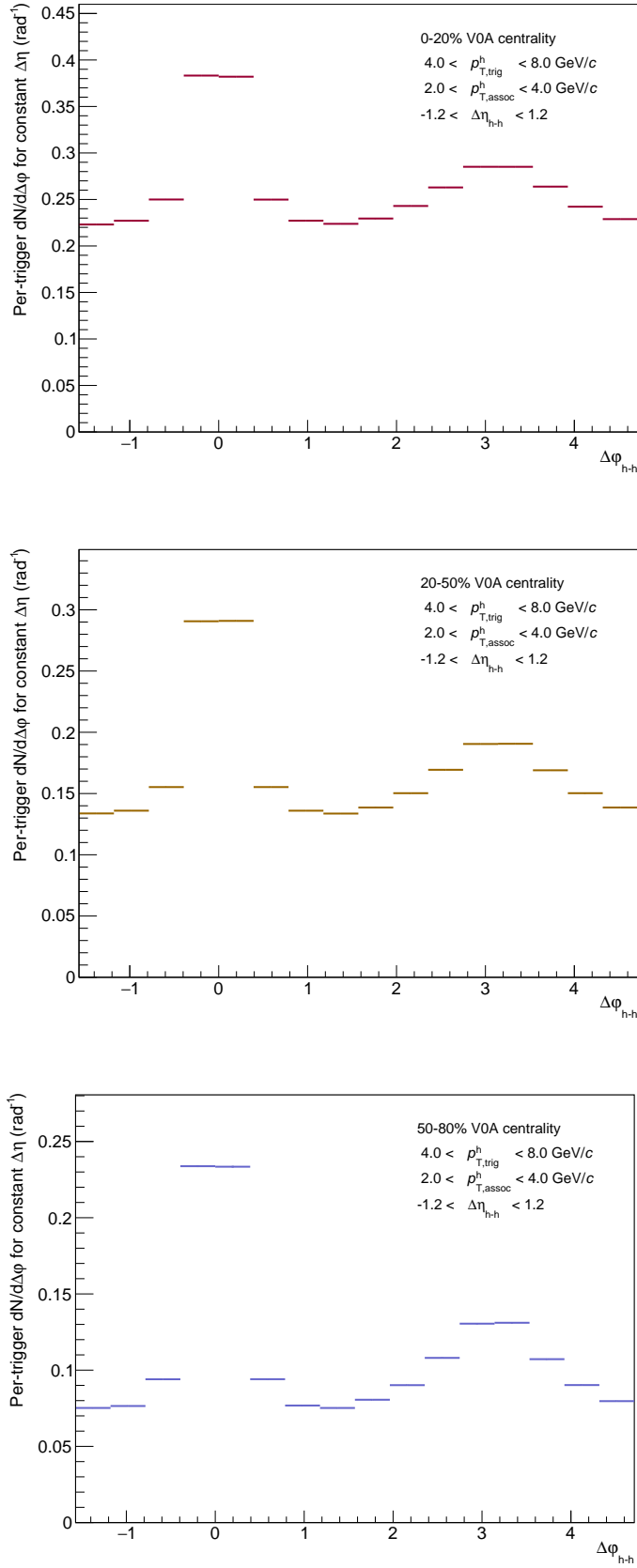


**Fig. 29:** Per-trigger normalized  $\Delta\phi$  correlations for h-h pairs in the 0-20% (top), 20-50% (center) and 50-80% (bottom) multiplicity bins.

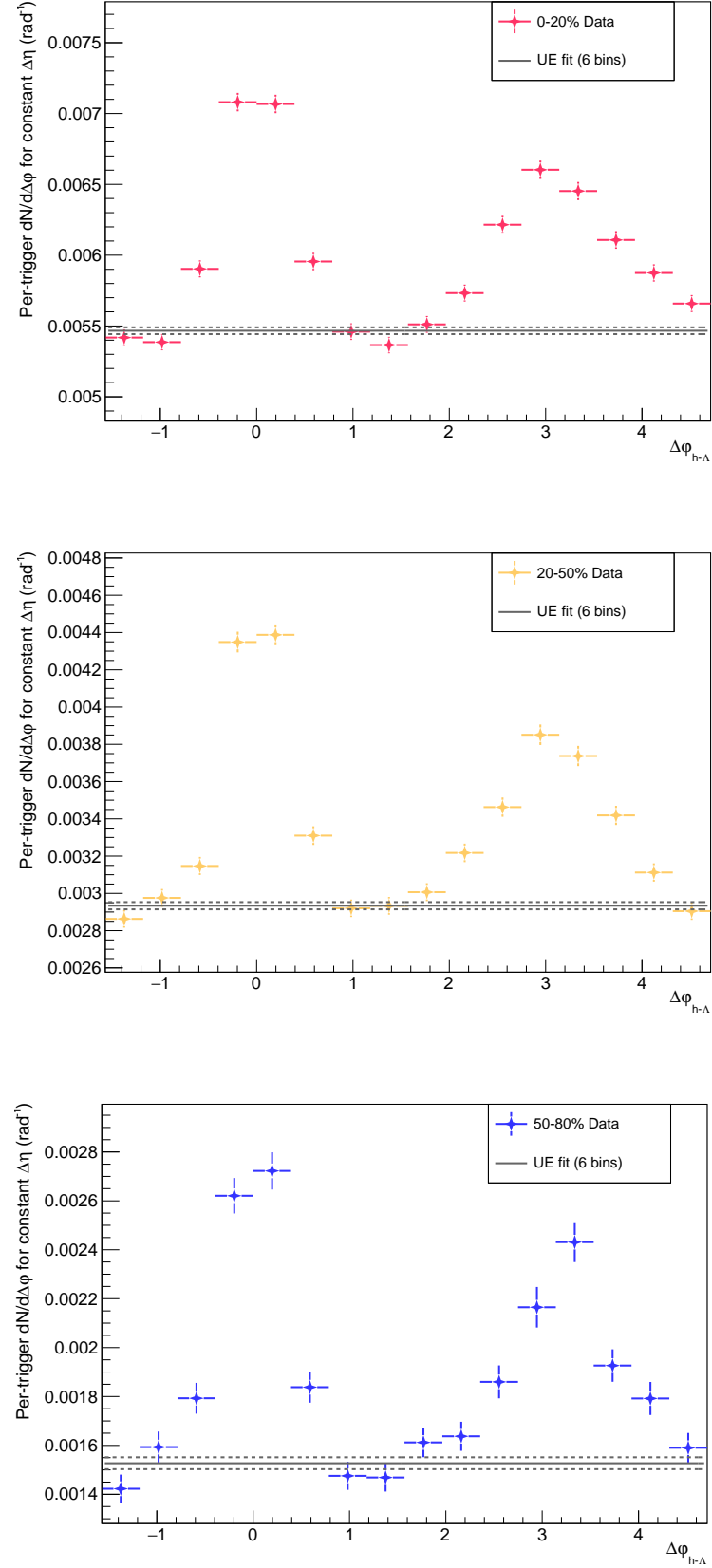


**Fig. 30:** The final per-trigger  $h - \Lambda$   $\Delta\phi$  correlations with underlying event fit for the 0-20% (top), 20-50% (center) and 50-80% (bottom) multiplicity bins. The solid line is the central value for the fit, with the dashed lines representing the error ( $\pm$ ). The underlying event fit was taken using the 6-bin technique described in this section.

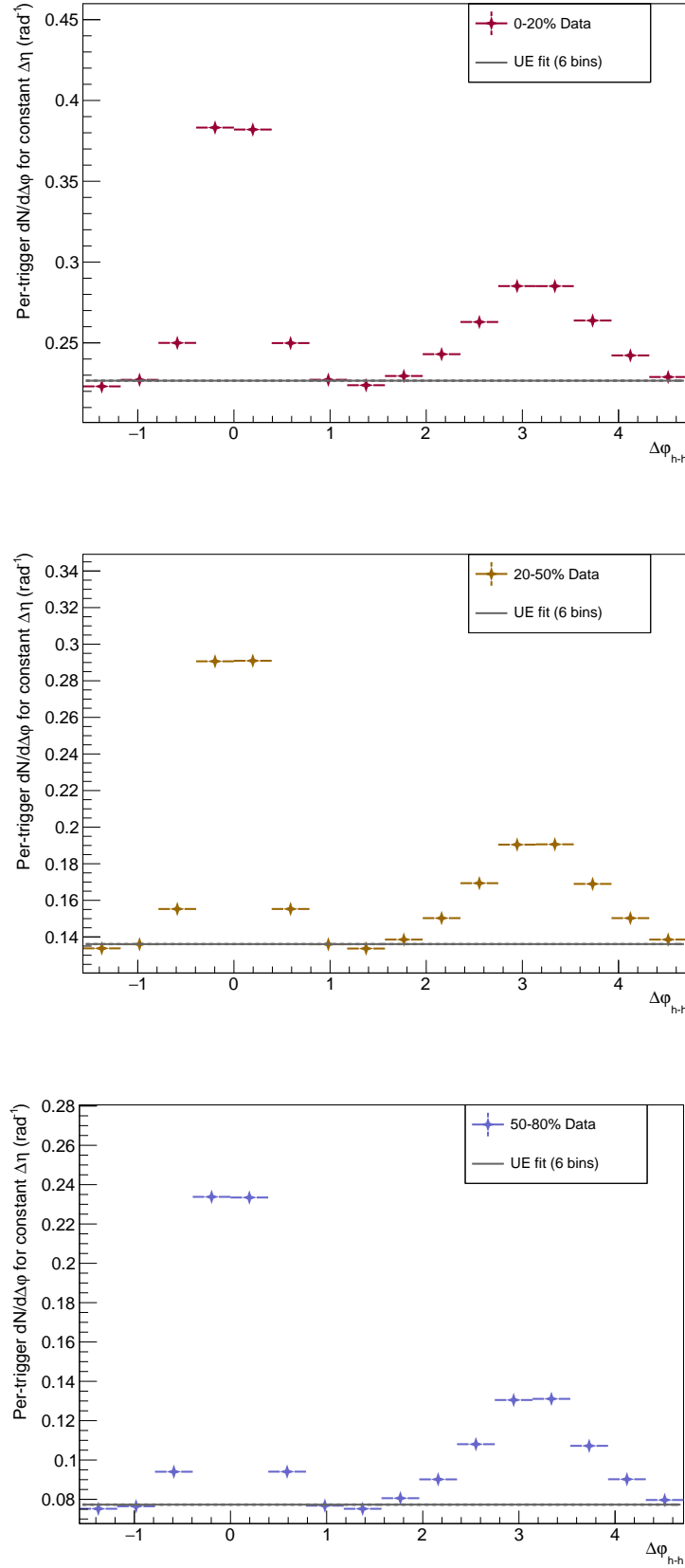


**Fig. 31:** The final per-trigger  $h-h$   $\Delta\phi$  correlations with underlying event fit for the 0-20% (top), 20-50% (center) and 50-80% (bottom) multiplicity bins. The solid line is the central value for the fit, with the dashed lines representing the error ( $\pm$ ). The underlying event fit was taken using the 6-bin technique described in this section.



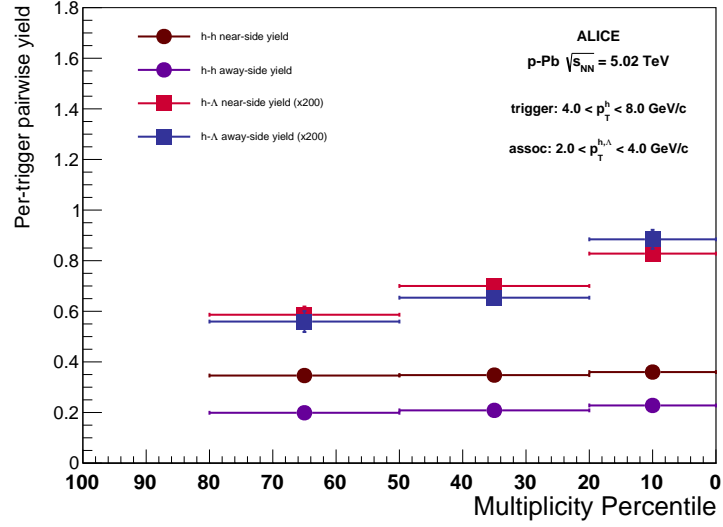


**Fig. 32:** Per-trigger pairwise  $h - \Lambda$  (scaled by 200 for clarity) and  $h - h$  yields plotted with respect to our multiplicity bins. The  $h - \Lambda$  sees roughly a 70% increase from the lowest multiplicity bin to the highest, while the  $h - h$  yield only sees around a 5% increase.

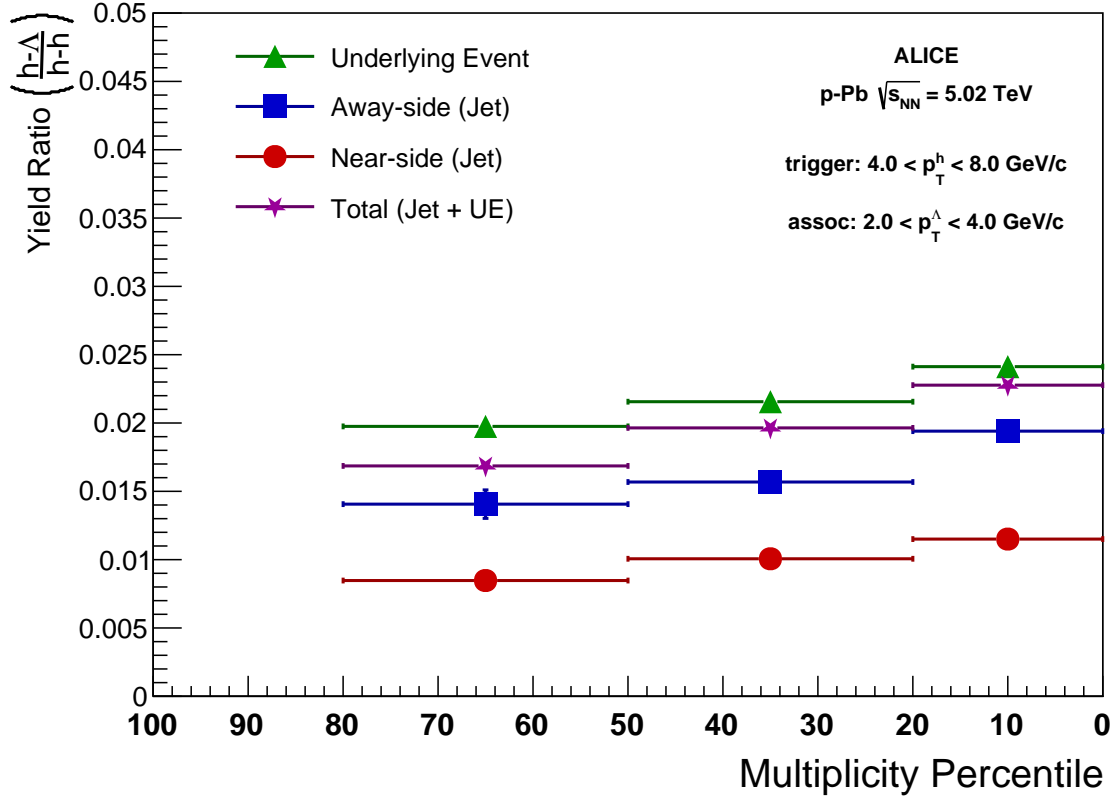


**Fig. 33:** Ratio of the per-trigger yields of  $h - \Lambda/h - h$  pairs as a function of multiplicity percentile for each of the kinematic regions. The yields are extracted using the procedure described in Section ??, with values taken from Tables ?? and ??.

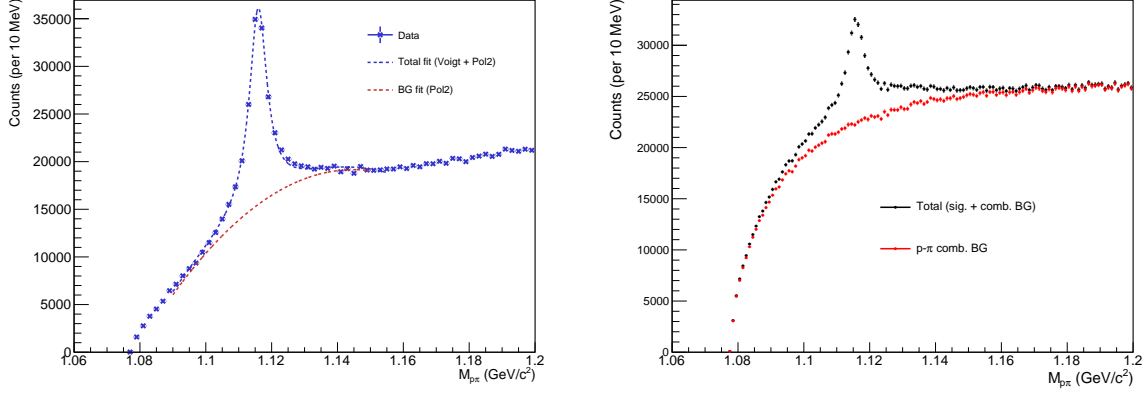


**Fig. 34:** Left: Invariant mass distribution with corresponding Voigt + Polynomial fit in our 20-50% multiplicity bin (data). Right: Our signal and background shapes in MonteCarlo (MC). Note that even though MC appears to have a completely different S/B, the signal shapes should be similar. Our fit in data appears to be massively underestimating our  $\Lambda$  signal, as our MC sample indicates we have  $\Lambda$  signal where our total data fit converges with our BG fit.

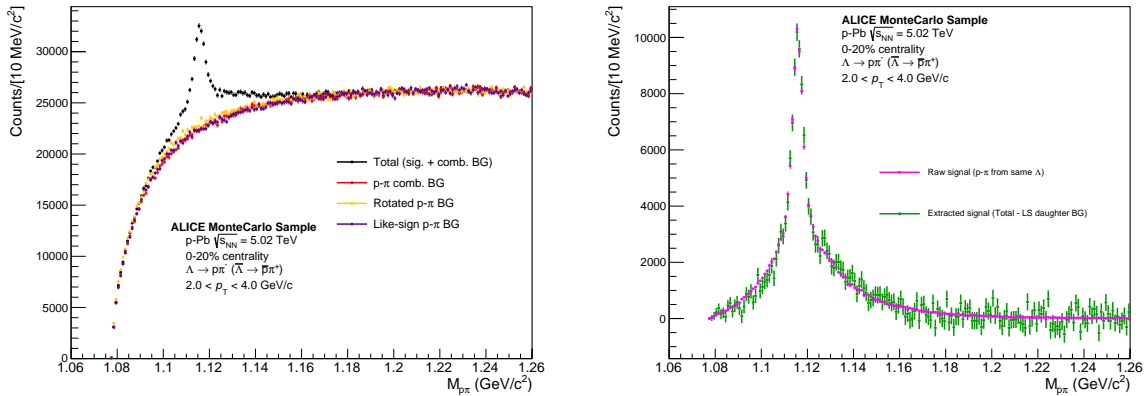


**Fig. 35:** Left: Invariant Mass distribution for unlike-sign  $p\pi$  pairs (black) in our MonteCarlo sample. The like-sign  $p\pi$  pair mass distribution (purple) and unlike-sign rotated  $p\pi$  distributions are scaled to match the unlike-sign distribution within the invariant mass region. The true combinatorial background (red) matches most closely with the like-sign pairs. Right: The actual  $\Lambda$  signal (magenta) compared with the result of subtracting the like-sign from the total unlike-sign  $p\pi$  distribution (green). The two distributions show good agreement.

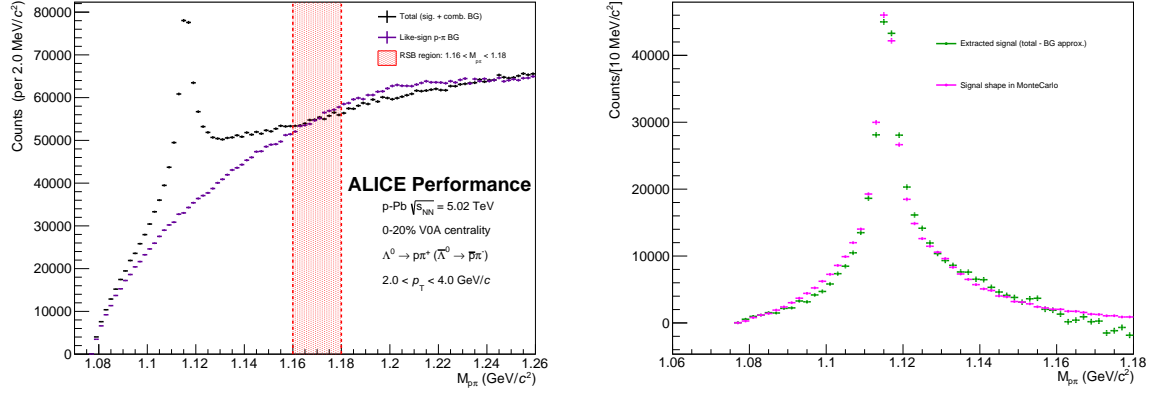


**Fig. 36:** Left: Invariant Mass distribution for unlike-sign  $p\pi$  pairs (black) along with the like-sign  $p\pi$  background (purple) and the RSB region (red) in the 0-20% multiplicity bin. Right: The extracted signal (green) compared with the resonance-technique reconstructed signal shape in MonteCarlo (magenta). The RSB was chosen such that these shapes are similar.

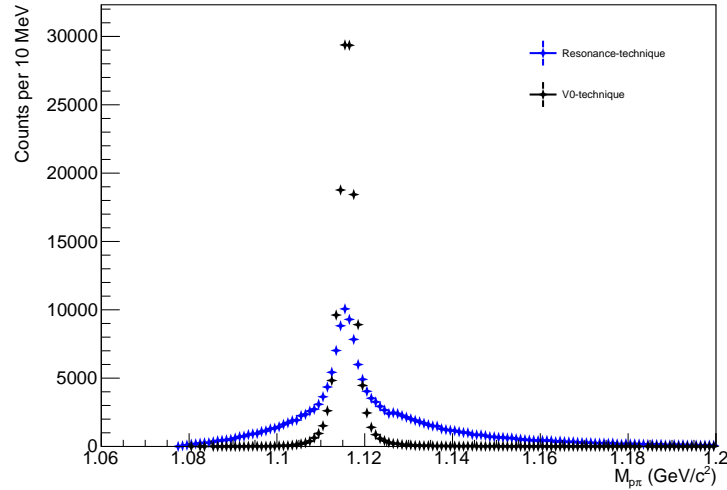


**Fig. 37:** The invariant mass signal for  $\Lambda$ s reconstructed using the resonance technique (blue) compared to the V0 technique (black) in MC. The wider tails of the resonance technique distribution are due to using the global AOD tracks for reconstruction, which do not account for the secondary vertex position and therefore slightly miscalculate the kinematics.

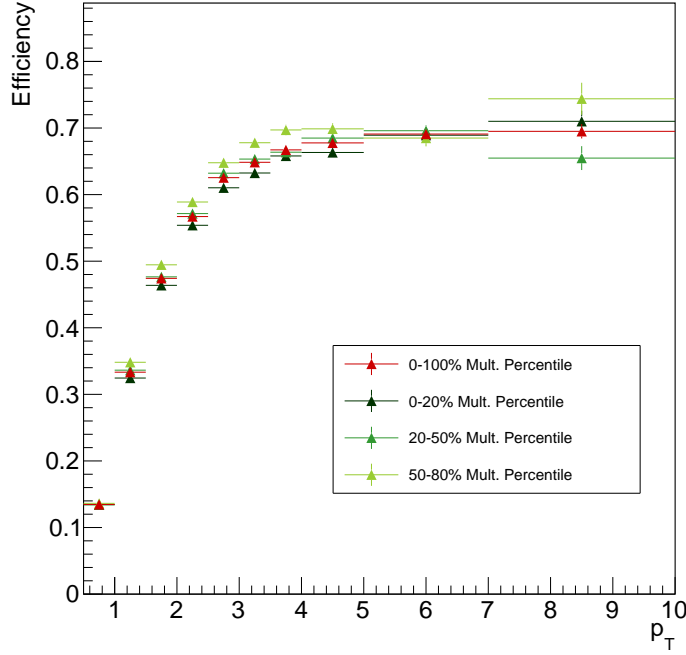


**Fig. 38:** Efficiency vs.  $p_T$  for  $\Lambda$  reconstruction using resonance technique for each multiplicity bin, along with an integrated 0-100% point in red. There does not appear to be any significant dependence on multiplicity. Also worth noting that the efficiency is higher for this technique when compared to the V0 technique, as expected (all AOD tracks from V0 finder daughters are also in total AOD track list).

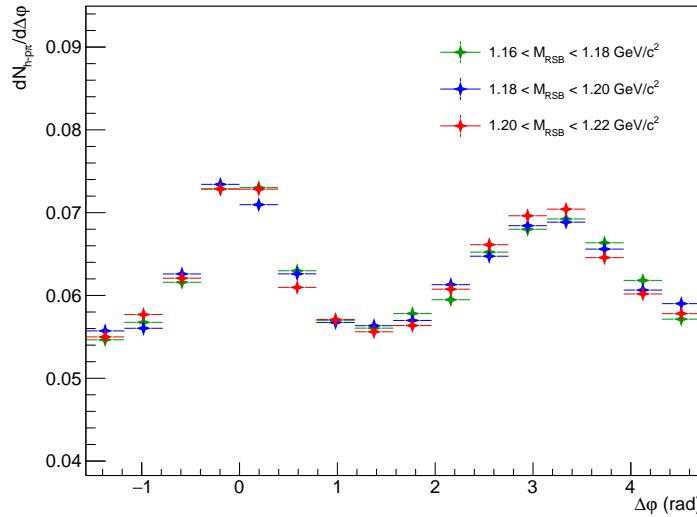


**Fig. 39:** The projected  $\Delta\phi$  distributions for different choices of RSB within the  $-1.2 < \Delta\eta < 1.2$  region. The correlation shapes are identical within the statistical errors.

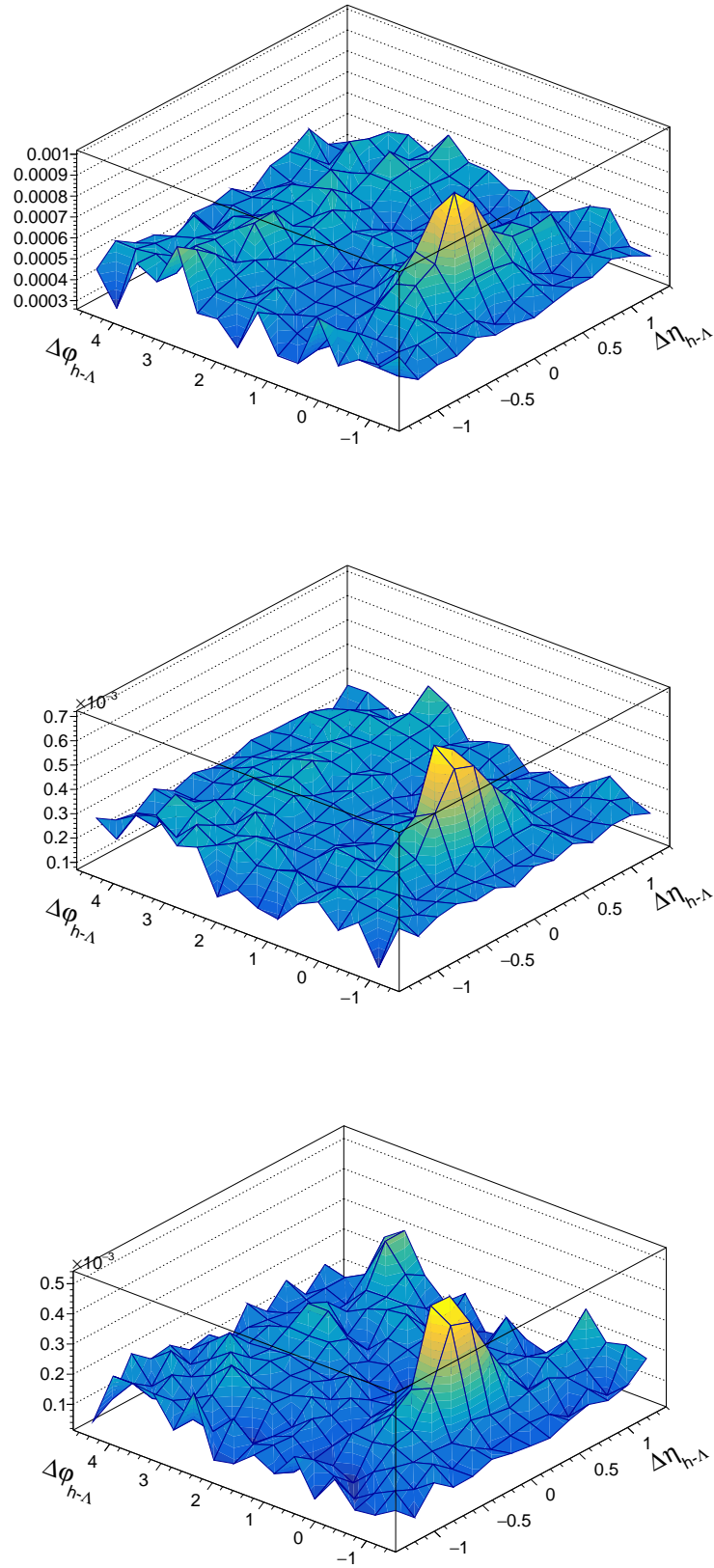


**Fig. 40:** The final per-trigger  $h - \Lambda$  2D  $\Delta\eta\Delta\phi$  distributions after mixed event acceptance correction and combinatorial background subtraction for the 0-20% (top), 20-50%(center) and 50-80% (bottom) multiplicity bins.

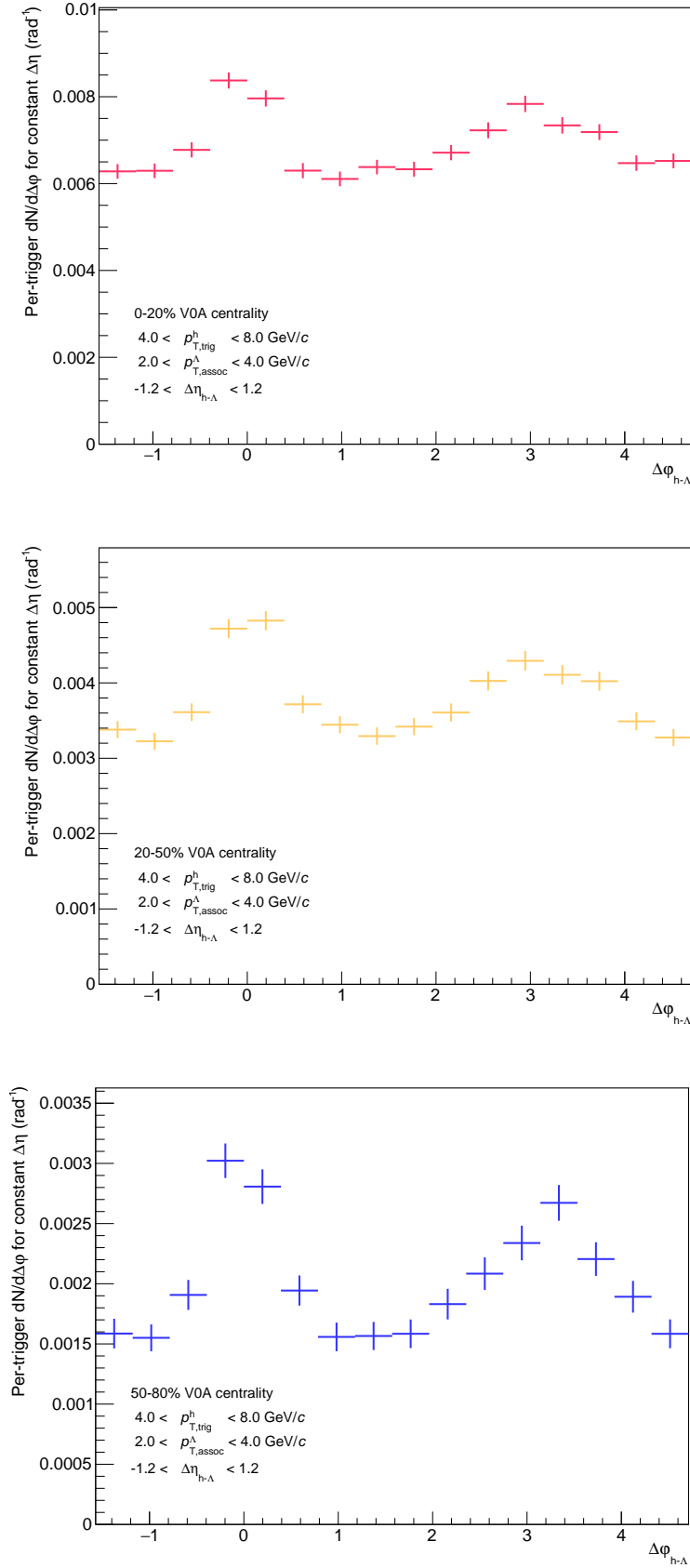


**Fig. 41:** The final per-trigger  $h - \Lambda$   $\Delta\phi$  distributions after mixed event acceptance correction and combinatorial background subtraction for the 0-20% (top), 20-50% (center) and 50-80% (bottom) multiplicity bins within  $-1.2 < \Delta\eta < 1.2$ .

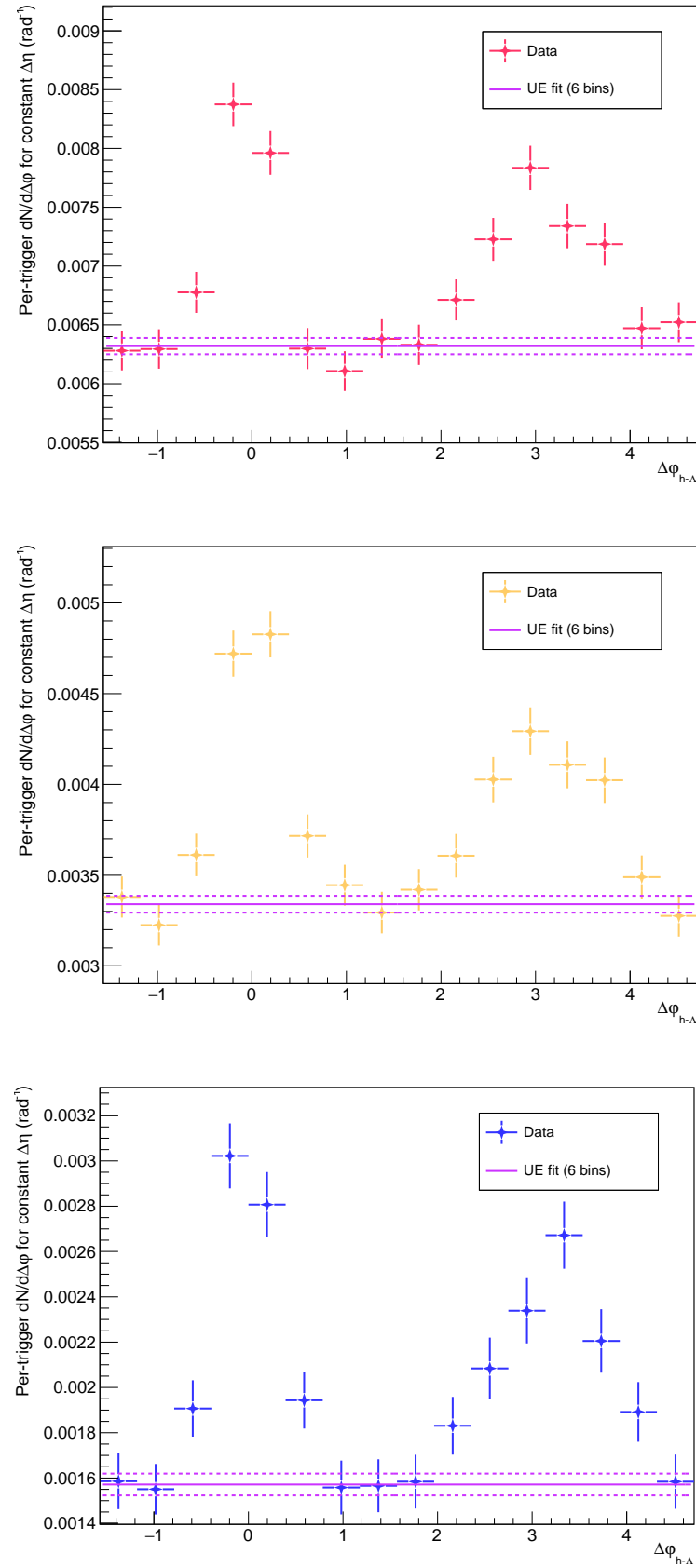


**Fig. 42:** The final  $h - \Lambda$   $\Delta\phi$  correlations with underlying event fit for the 0-20% (top), 20-50%(center) and 50-80% (bottom) multiplicity bins. The solid line is the central value for the fit, with the dashed lines representing the error (+/-). The underlying event fit was taken using the 6-bin technique described in Section ??.

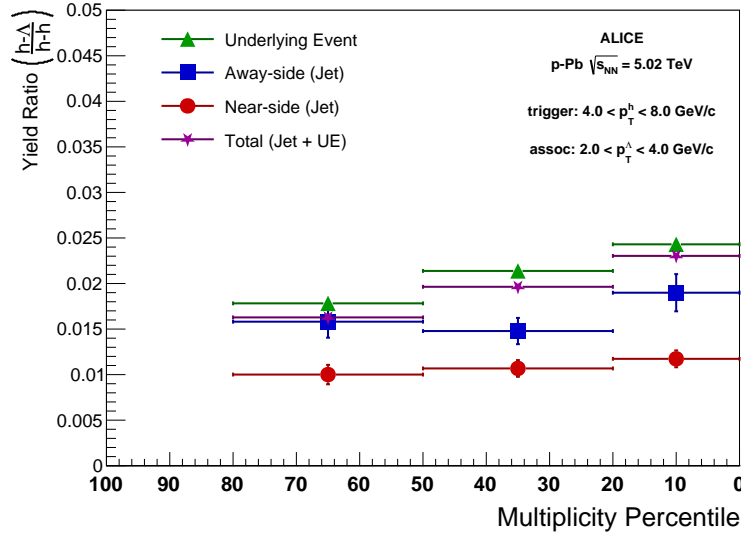


**Fig. 43:** The final  $h - \Lambda/h - h$  ratio vs. multiplicity plot for  $\Lambda_s$  reconstructed using the resonance technique. While the error bars and statistical fluctuations are larger than the same plot with  $\Lambda_s$  reconstructed using the V0 technique (due to the comb. BG subtraction), the general trends are the same.

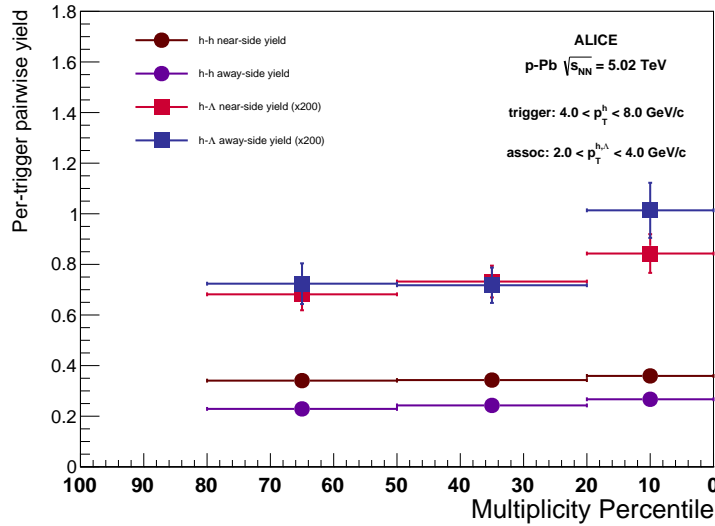


**Fig. 44:** The final  $h - \Lambda/h - h$  per-trigger pairwise jet yields vs. multiplicity plot for  $\Lambda_s$  reconstructed using the resonance technique. The general trends are very similar to the same plot with  $\Lambda_s$  reconstructed using the V0 technique, just with larger uncertainties.



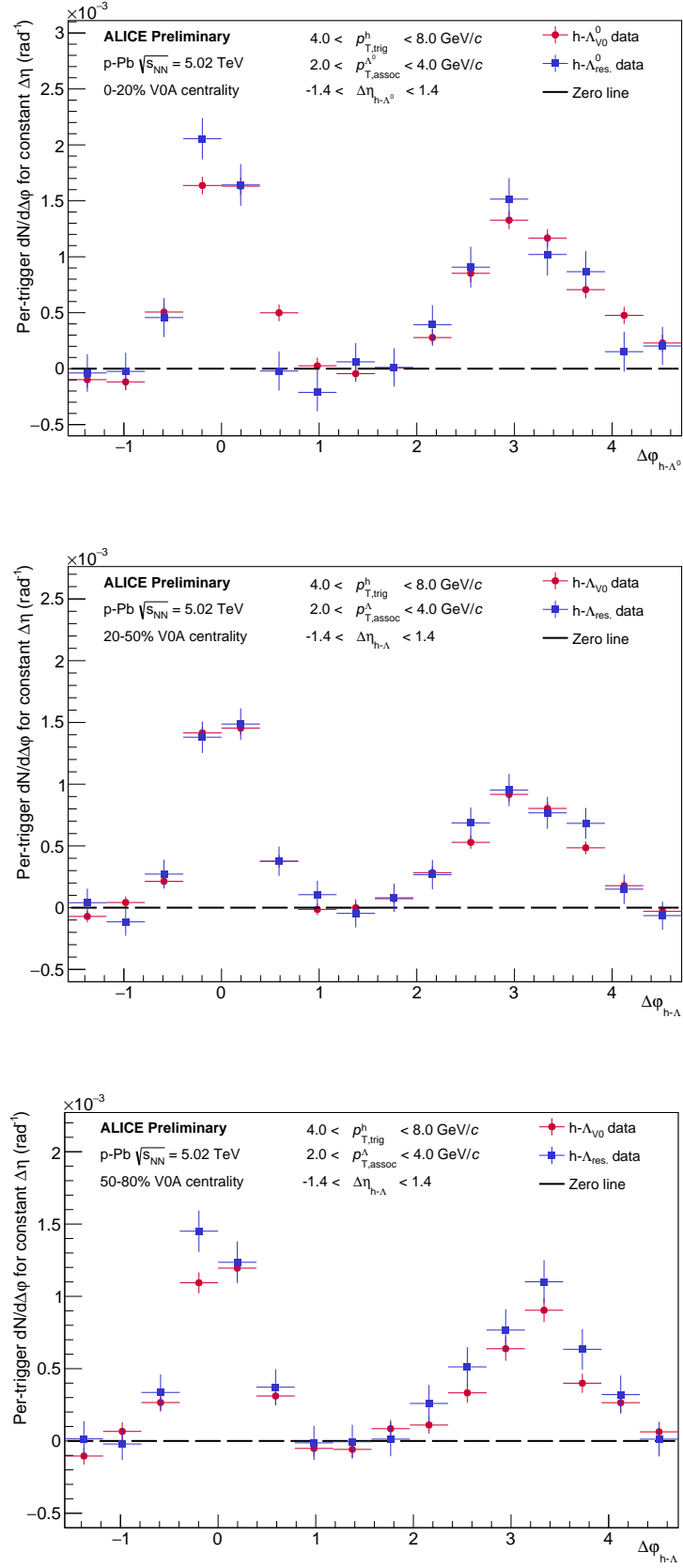


**Fig. 45:** The final per-trigger  $h-\Lambda$   $\Delta\phi$  correlations for  $\Lambda$ s reconstructed using the resonance technique (blue) and the V0 technique (red) for each multiplicity bin (from top to bottom). All three multiplicity bins show very good agreement between the two techniques.

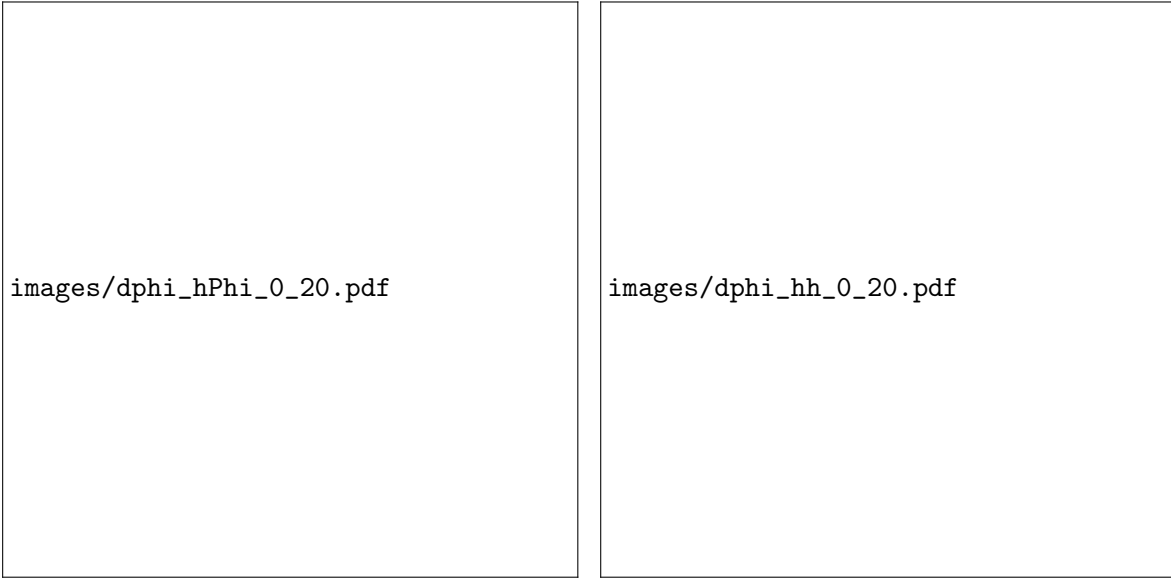


**Fig. 46:** Angular Correlations for  $h - \phi$  (left) and  $h - h$  (right) pairs after full acceptance and efficiency corrections. Both distributions are fit with a function (dashed lines) consisting of two gaussians and a constant BG term. The constant BG term of the fit is used in calculating the "Jet-like" yields in the near- and away-side peaks.



**Fig. 47:** Example histogram showing how the yields in the different regions of correlation space are calculated. The green region represents the "Underlying Event", and is defined by the constant BG term of the  $\Delta\phi$  fit function. The near- (red) and away-side (blue) Jet yields are defined as the area above the constant BG in the  $-\pi/2 < \Delta\phi < \pi/2$  and  $\pi/2 < \Delta\phi < 3\pi/2$  regions, respectively.



**Fig. 48:** Direct comparison of the generated (green) and reconstructed (red)  $\Delta\phi$  correlation, using the LHC17f2b.FAST dataset (left). The ratio of the two distributions (right) shows that the reconstruction technique in Eq. ?? is able to correctly capture the real  $h - \phi$  correlation, with a straight line fit of the ratio giving a value of  $0.99 \pm 0.02$



**Fig. 49:** Full MC Closure test (**left**) comparing the generated per-trigger correlation (green) with the correlation measured using the track reconstruction outlined in eq. ?? (blue). The ratio of the two (**right**) shows good agreement with 1, within statistical fluctuations.



**Fig. 50:**  $\Delta\phi$  correlation (**left**) showing the differences between different invariant mass ranges for the  $\phi(1020)$  signal region. By looking at the ratio of these correlations to the chosen range ( $1.014 \text{ GeV}/c^2 < M_\phi < 1.026 \text{ GeV}/c^2$ )

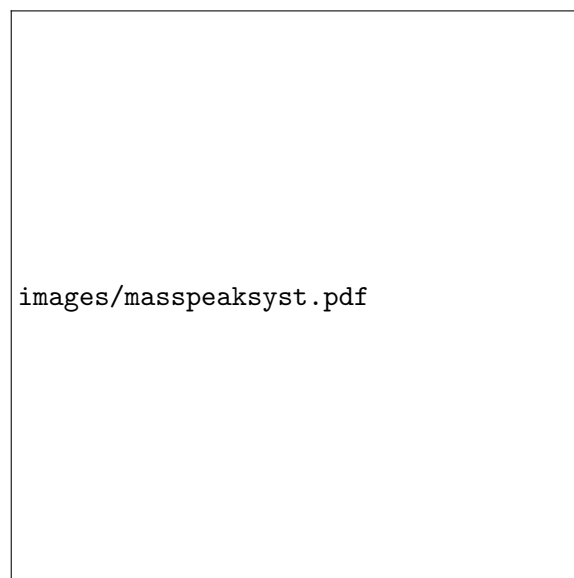


**Fig. 51:**



**Fig. 52:** Plot showing the variation in final  $\Delta\phi$  correlation (**left**) from varying the right sideband invariant mass region. This variation changes both the correlation background subtraction, as well as the likesign scaling factor. However, from the ratios of the variation to the standard range (**left**), we see this variation has no effect on the final correlation structure.



**Fig. 53:** Projection of the ratio  $\Delta\phi$  points onto a single distribution shows no significant difference from the variation in right sideband region (RMS of 0.5%)

## A Resonance Technique for $\Lambda$ Reconstruction

While using the V0 finder to reconstruct  $\Lambda$  baryons is the most common method, it is possible that the V0 finder algorithm introduces some topological biases in the  $\Lambda$  reconstruction, even when no further topological cuts are being applied to the V0 or its corresponding daughters. Because of this, we also investigate another method for reconstructing  $\Lambda$  baryons whereby all proton and pion pairs from the global AOD track list that pass the daughter cuts (Section ??) within an event are combined to reconstruct the  $\Lambda$ s. This method is referred to as the *resonance technique*, as it is the technique used to reconstruct short-lived particles that could otherwise not be reconstructed using the V0 finder.

### A.1 Combinatorial Background Estimation

As  $\Lambda$  baryons reconstructed using the resonance technique will have a large combinatorial background, the final correlation will contain  $h - (p\pi)$  pairs that need to be removed. In order to remove this background, we need both an estimate of the correlation shape of the  $h - (p\pi)$  pairs, as well as an estimate of the Signal/Background in the  $\Lambda$  mass peak region.

The background shape of the  $\Lambda$  invariant mass distribution can be estimated using one of the following techniques:

- **Like-sign  $p\pi$  pairs** - Reconstruct the invariant mass of like-sign  $p\pi$  pairs, and scale the like-sign  $p\pi$  distribution to the un-like sign  $p\pi$  distribution in a region outside of the  $\Lambda$  signal region.
- **Rotated  $p\pi$  pairs** - Reconstruct the invariant mass of unlike-sign  $p\pi$  pairs, but rotate either the pion or proton around the z-axis by  $\pi$  radians, and scale the rotated  $p\pi$  distribution to the un-like sign  $p\pi$  distribution in a region outside of the  $\Lambda$  signal region.
- **Voigt + polynomial fit** - Perform a standard fitting procedure using TMath::Voigt for the signal along with a second-order polynomial for the background.

We will address the last technique (fitting procedure) first, as it fails to properly estimate the signal and background in data. To illustrate this, we can find the best possible fits in data and extract the corresponding signal shape to compare with the signal shape in MonteCarlo (with full track reconstruction). This comparison is done for our 20-50% multiplicity bin in Figure ??.

The MonteCarlo plot was generated using our standard MC sample, and applying the same techniques for  $\Lambda$  reconstruction described previously using the global AOD list. The background on the plot was generated by taking all  $p\pi$  pairs that did NOT come from a  $\Lambda$ , verified within the MC stack. While comparing data to MonteCarlo should be done with caution, it should also be pointed out that even extracting the  $\Lambda$  signal in MonteCarlo without a priori knowledge of the background shape is nontrivial and naive attempts result in severely underestimating the signal.

While it may be possible to get a proper handle on the background shape using the fitting procedure, all attempts by the author to do so have failed. Because of this, we will only consider the first two techniques for the rest of this analysis. To determine which of the two remaining techniques is more effective, we compare the background shape of the  $\Lambda$  invariant mass distribution for both techniques in MonteCarlo where we have direct access to the background shape. The like-sign and rotated  $p\pi$  pairs are shown along with the extracted signal comparison in Figure ??.

The like-sign  $p\pi$  pairs match the background shape of the  $\Lambda$  invariant mass distribution more closely than the rotated  $p\pi$  pairs, so we use the like-sign  $p\pi$  pairs to estimate the combinatorial background in the  $\Lambda$  invariant mass distribution in data.

The region outside of the  $\Lambda$  signal region used for scaling the background estimates is called the Right SideBand region, or RSB. The choice of RSB has a large systematical effect on the background approximation as neither the like-sign nor rotated  $p\pi$  pairs match the background shape throughout the

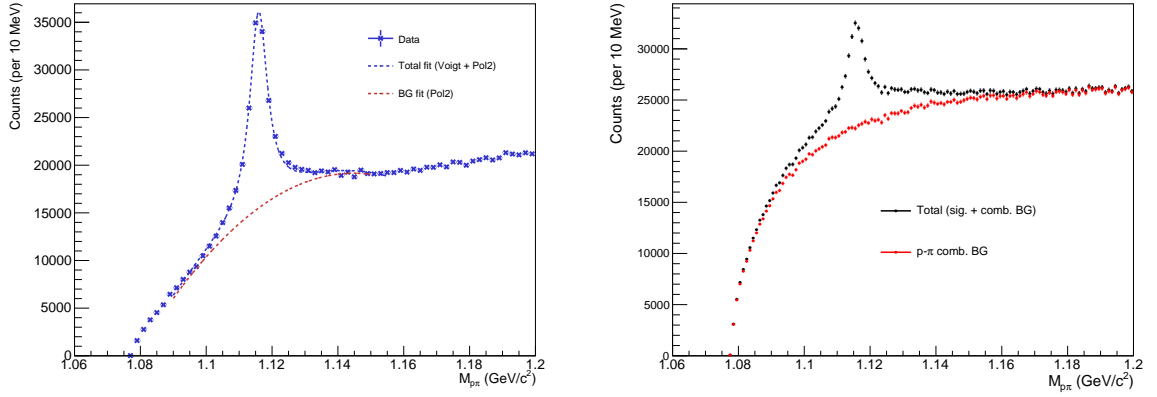


**Fig. A.1:** Left: Invariant mass distribution with corresponding Voigt + Polynomial fit in our 20-50% multiplicity bin (data). Right: Our signal and background shapes in MonteCarlo (MC). Note that even though MC appears to have a completely different S/B, the signal shapes should be similar. Our fit in data appears to be massively underestimating our  $\Lambda$  signal, as our MC sample indicates we have  $\Lambda$  signal where our total data fit converges with our BG fit.

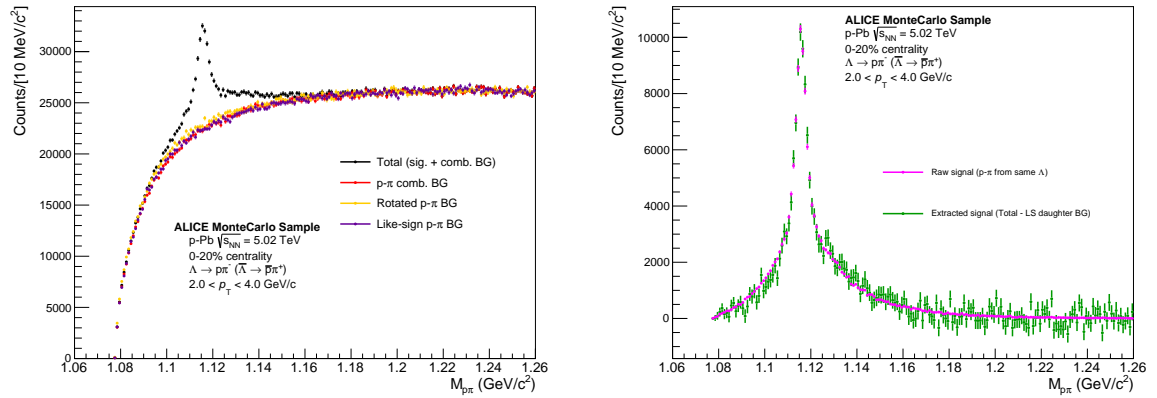


**Fig. A.2:** Left: Invariant Mass distribution for unlike-sign  $p\pi$  pairs (black) in our MonteCarlo sample. The like-sign  $p\pi$  pair mass distribution (purple) and unlike-sign rotated  $p\pi$  distributions are scaled to match the unlike-sign distribution within the invariant mass region. The true combinatorial background (red) matches most closely with the like-sign pairs. Right: The actual  $\Lambda$  signal (magenta) compared with the result of subtracting the like-sign from the total unlike-sign  $p\pi$  distribution (green). The two distributions show good agreement.

entirety of the distribution. The RSB region was chosen to minimize the difference in shape between the extracted signal in data (total - like-sign BG) and the resonance-technique reconstructed signal shape in MonteCarlo, generated from all  $p\pi$  pairs which guaranteed came from a  $\Lambda$ . The raw unlike-sign  $p\pi$  distribution for the 0-20% Multiplicity Percentile is shown in Figure ??, and the extracted signal and comparison with MonteCarlo is shown in Figure ??.

The resonance technique  $p\pi$  invariant mass distributions for each multiplicity bin are shown in Figure ??, and a table containing their yields, signal/BG and significance is shown in Table ??.

## A.2 Invariant Mass Regions

The signal shape and background from  $\Lambda$ s reconstructed using the resonance technique is vastly different than those reconstructed using the V0 finder, thus it is necessary to define new invariant mass regions such that the signal can be properly extracted:

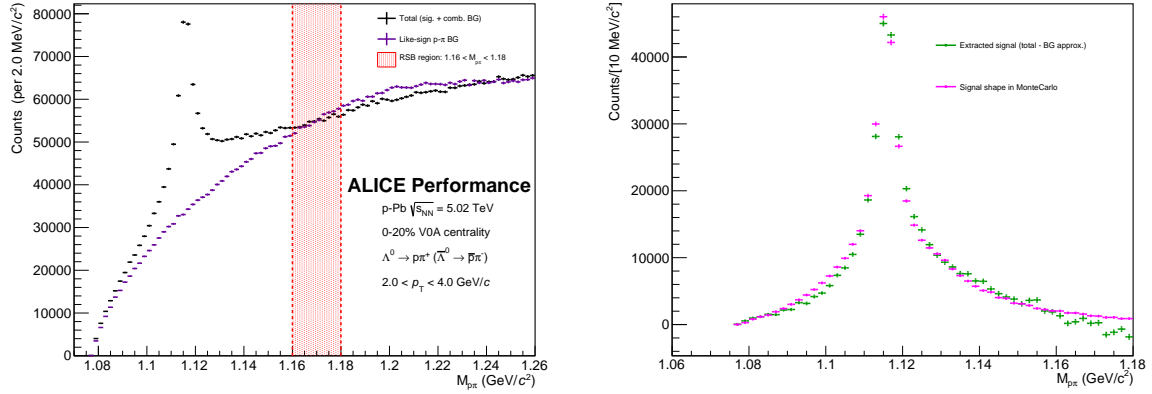


**Fig. A.3:** Left: Invariant Mass distribution for unlike-sign  $p\pi$  pairs (black) along with the like-sign  $p\pi$  background (purple) and the RSB region (red) in the 0-20% multiplicity bin. Right: The extracted signal (green) compared with the resonance-technique reconstructed signal shape in MonteCarlo (magenta). The RSB was chosen such that these shapes are similar.

- unlike-sign  $p\pi$  in  $\Lambda$  mass region:  $1.014 \text{ GeV}/c^2 < M_{p\pi} < 1.026 \text{ GeV}/c^2$
- like-sign  $p\pi$  in  $\Lambda$  mass region:  $1.014 \text{ GeV}/c^2 < M_{p\pi} < 1.026 \text{ GeV}/c^2$
- unlike-sign  $p\pi$  in 0-20% multiplicity bin RSB:  $0.995 \text{ GeV}/c^2 < M_{p\pi} < 1.005 \text{ GeV}/c^2$
- unlike-sign  $p\pi$  in 20-50% multiplicity bin RSB:  $0.995 \text{ GeV}/c^2 < M_{p\pi} < 1.005 \text{ GeV}/c^2$
- unlike-sign  $p\pi$  in 50-80% multiplicity bin RSB:  $0.995 \text{ GeV}/c^2 < M_{p\pi} < 1.005 \text{ GeV}/c^2$

The signal regions were chosen to maximize significance and were not multiplicity dependent, whereas the RSB regions were chosen to minimize the difference in shape between the extracted signal in data (total - like-sign BG) and the resonance-technique reconstructed signal shape in MonteCarlo, generated from all  $p\pi$  pairs which guaranteed came from a  $\Lambda$ , as was demonstrated in Figure ???. This process was repeated for each multiplicity bin resulting in slight fluctuations of the RSB with respect to multiplicity.

For the resonance technique, the combinatorial background contribution to the correlation was removed using the like-sign  $p\pi$  distribution scaled to the RSB for each multiplicity bin, a procedure described with more detail in Section ??.

### A.3 Efficiency Correction

To estimate the  $\Lambda$  reconstruction efficiency, we compare  $\Lambda$  yields reconstructed using the resonance technique to the true  $\Lambda$  yields using the MC production LHC17f2b\_FAST (anchored to LHC16q\_FAST production). The efficiency was calculated using the following formula:

$$\epsilon_{\Lambda} = \frac{N_{\Lambda, \text{ reco. with resonance technique}}}{N_{\Lambda, \text{ real MC yield}}},$$

where each  $\Lambda$  in  $N_{\Lambda, \text{ reco. with resonance technique}}$  is found in the following way:

- Find all protons and pions within the AOD list that pass our daughter cuts (Section ??, PID is done via MC label)



- 709 – For each proton in list, determine if it came from a  $\Lambda$  (via MC label)
- 710 – If proton came from  $\Lambda$ , loop through pions until we find one that came from same  $\Lambda$  (via MC label)
- 711 – Reconstruct the  $\Lambda_{reco}$  using the daughter AOD tracks
- 712 – Only keep  $\Lambda_{reco}$  if  $|\eta| < 0.8$
- 713 and each  $\Lambda$  in  $N_{\Lambda, \text{real MC yield}}$  meets the following criteria:
- 714 – Found in the MC stack
- 715 –  $|\eta_{\Lambda}| \leq 0.8$
- 716 – The  $\Lambda$  decays to  $p\pi$

717 As the resulting invariant mass signal from  $N_{\Lambda, \text{reco. with resonance technique}}$  is much wider than the signal  
 718 from the V0 finder technique (Figure ??), the efficiency calculation is taken using the entire invariant  
 719 mass range and the correction for our finite signal region is applied later (see Section ??).

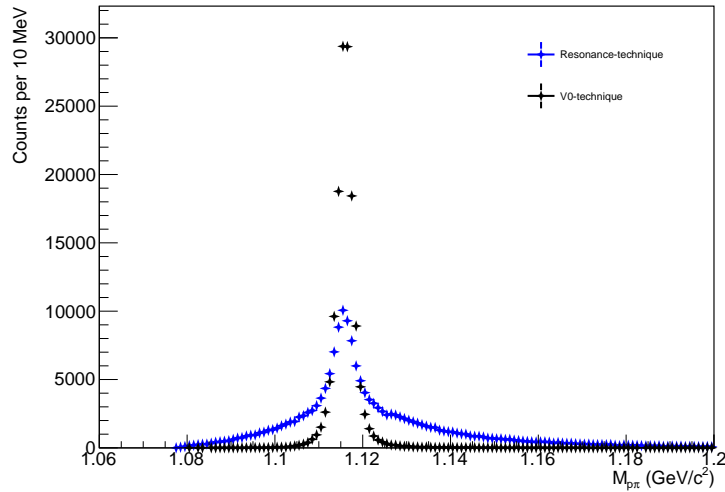


**Fig. A.4:** The invariant mass signal for  $\Lambda$ s reconstructed using the resonance technique (blue) compared to the V0 technique (black) in MC. The wider tails of the resonance technique distribution are due to using the global AOD tracks for reconstruction, which do not account for the secondary vertex position and therefore slightly miscalculate the kinematics.

720 While previous analyses focus solely on primary  $\Lambda$ s (excluding  $\Omega$  and  $\Xi$  contamination), there is no  
 721 requirement for either the V0-reconstructed  $\Lambda$  or the MC-generated  $\Lambda$  to be a primary particle. As this  
 722 analysis is mostly interested in the  $\Lambda$  due to its strange quark content, whether or not the  $\Lambda$  came from  
 723 a cascade decay is irrelevant. This is important to note when making comparisons between this analysis  
 724 and previous analyses, as secondary contamination from cascades accounts for nearly 20% of all  $\Lambda$ s.

725 As mentioned in Section ??, both the  $\Lambda$  and the  $\bar{\Lambda}$  were combined together for this efficiency calculation.  
 726 Efficiencies were calculated as a function of  $p_T$ ,  $\eta$ ,  $\phi$ , Event Z vertex, and Multiplicity. However, the  
 727 final efficiency correction was applied as a function of  $p_T$  only and can be seen in Figure ??.

728 The  $h - \Lambda$  pairwise efficiency correction is applied in the same way as described in Section ??.

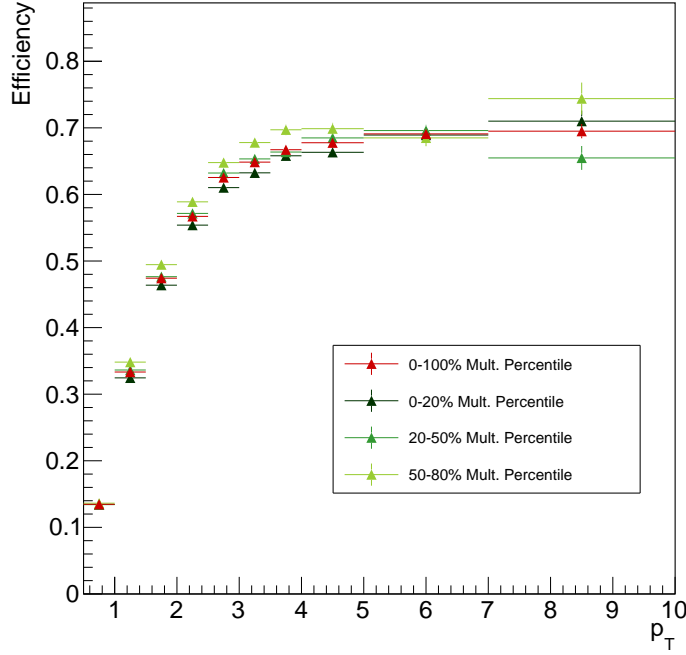


**Fig. A.5:** Efficiency vs.  $p_T$  for  $\Lambda$  reconstruction using resonance technique for each multiplicity bin, along with an integrated 0-100% point in red. There does not appear to be any significant dependence on multiplicity. Also worth nothing that the efficiency is higher for this technique when compared to the V0 technique, as expected (all AOD tracks from V0 finder daughters are also in total AOD track list).

#### A.4 Mixed Event Acceptance Correction

The procedure for correcting for finite detector acceptance in our angular correlations is exactly the same as the one described in Section ??.

#### A.5 Removal of Combinatorial $p - \pi$ Background

Since we do not know which  $p - \pi$  pairs came from a real  $\Lambda$  decay, we must remove the contribution to the angular correlation structure due to the combinatorial background of  $p - \pi$  pairs that did not come from a  $\Lambda$ .

To do this,  $h$ -( $p\pi$ ) angular correlations are measured for unlike-sign  $p\pi$  pairs within the right sideband (RSB) for each multiplicity bin. The correlation structure in the RSB is then normalized to its integral to give an estimate of the combinatorial background shape, as the RSB should contain little-to-no  $p\pi$  pairs that came from a  $\Lambda$ . The self-normalized 1D  $\Delta\phi$  distributions for different choices of RSB regions are shown in Figure ?. As the shapes are similar for each choice of RSB, we conclude that there is no substantial contribution from  $p\pi$  pairs coming from  $\Lambda$  decay.

For the remainder of this resonance technique analysis we will be using  $1.16 < M_{RSB} < 1.18$  as our choice of RSB region for each multiplicity bin.

Next, the  $h - p\pi$  angular correlation in our chosen sideband region is scaled to match the integral of our background in our signal region. However, this scaling is not performed directly as while the Signal/Background and Signal/(Signal + Background) ratios are the same for the single-particle  $\Lambda$  distribution and its corresponding invariant mass axis in our  $h - \Lambda$  distribution, the total yields are different. We therefore scale the  $h - p\pi$  distribution in the RSB to the BG integral in our signal region found using the following formula:

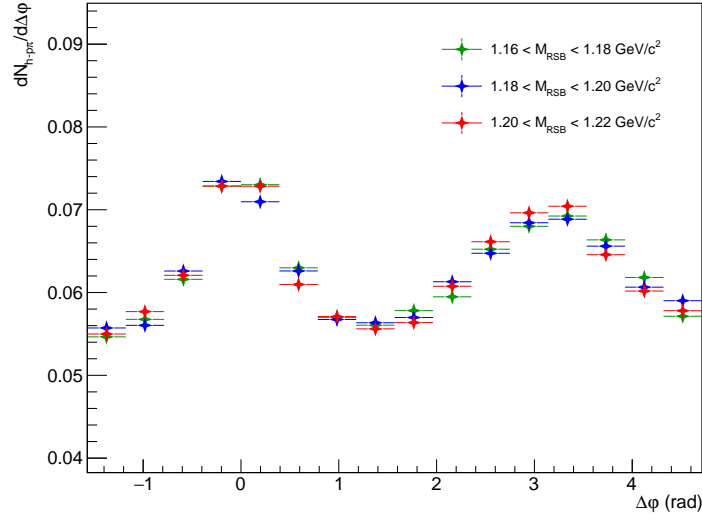


**Fig. A.6:** The projected  $\Delta\phi$  distributions for different choices of RSB within the  $-1.2 < \Delta\eta < 1.2$  region. The correlation shapes are identical within the statistical errors.

$$h - p\pi \text{ Combinatorial BG} = (\text{Integral of } h - p\pi \text{ in Signal Region}) \times \left(1 - \frac{S}{S+B}\right), \quad (\text{A.1})$$

where  $S$  and  $B$  are calculated in the Signal region using the single-particle  $\Lambda$  distributions from Table ??.

Once the  $h - p\pi$  angular correlation in the RSB is scaled to match the  $h - p\pi$  Combinatorial BG, it is subtracted from the total  $h - p\pi$  distribution in our signal region, then scaled to correct for our finite signal region. This scale factor is calculated using the following formula:

$$s_{\text{finite region}} = (\text{Integral of residual in signal region} / \text{Total integral of residual})^{-1} \quad (\text{A.2})$$

Once the scale factor is applied, we are then left with the full  $h - \Lambda$  2D angular correlations and corresponding 1D  $\Delta\phi$  projections, shown in Figures ?? and ??, respectively.

## A.6 Near-side, Away-side and Underlying Event Yield Extraction

The procedure for extracting the near-side, away-side and underlying event yields is exactly the same as the one described in Section ?. However, due to the statistical fluctuations introduced by the combinatorial background subtraction, we will be limiting the underlying event fitting procedure to the “6-bin average” method. The final  $\Delta\phi$  correlations with their corresponding underlying event fits can be seen in Figure ?. The extracted per-trigger yields and corresponding errors are shown in Table ?.

Multiplicity Bin	Near-side Jet	Away-side Jet	Underlying Event	Total
0-20%	$4.21\text{e-}3 \pm 0.38\text{e-}3$	$5.07\text{e-}3 \pm 0.54\text{e-}3$	$1.01\text{e-}1 \pm 0.01\text{e-}1$	$1.11\text{e-}1 \pm 0.07\text{e-}1$
20-50%	$3.66\text{e-}3 \pm 0.31\text{e-}3$	$3.58\text{e-}3 \pm 0.35\text{e-}3$	$5.34\text{e-}2 \pm 0.07\text{e-}2$	$6.05\text{e-}2 \pm 0.05\text{e-}2$
50-80%	$3.40\text{e-}3 \pm 0.31\text{e-}3$	$3.62\text{e-}3 \pm 0.40\text{e-}3$	$2.51\text{e-}2 \pm 0.08\text{e-}2$	$3.21\text{e-}2 \pm 0.05\text{e-}2$

**Table A.1:** Per-trigger pairwise  $h - \Lambda$  extracted yields and corresponding errors in the different kinematic regions for each multiplicity bin. The yields were extracted using the same procedure described in Section ?.

## A.7 Results and Comparison with V0 Technique

The final  $h - \Lambda/h - h$  ratio vs. multiplicity plot for  $\Lambda$ s reconstructed using the resonance technique is shown in Figure ?? . The per-trigger near and away-side pairwise yields vs. multiplicity for the  $h - \Lambda$  and  $h - h$  distributions are shown in Figure ?? .

A comparison of the final per-trigger  $h - \Lambda \Delta\phi$  correlation structure for the resonance and V0 techniques can be seen in Figure ?? . The correlation shapes are nearly identical, with the resonance technique having slightly larger uncertainties due to the combinatorial background subtraction. While this is not surprising (a  $\Lambda$  is a  $\Lambda$ , regardless of how it is reconstructed), it serves as a powerful cross check to our central values from the V0 technique.

## B Second Momentum Bin Measurement

In order to gain more insight into the  $\Lambda$  production in jets vs. the underlying event, we can also split the associated momentum bins into a high  $p_T$  bin ( $2.5 < p_T < 4.0 \text{ GeV}/c$ ) and a low  $p_T$  bin ( $1.5 < p_T < 2.5 \text{ GeV}/c$ ). The correlation analysis is performed for these two separate momentum bins exactly as laid out in Section 4, and is done for both  $h - \Lambda$  and  $h - h$  correlated pairs. The results for the final  $\Delta\phi$  distributions are shown in Figures ?? (low  $p_T$  bin) and ?? (high  $p_T$  bin).

By comparing the ratio of  $(h - \Lambda)/(h - h)$  pairs in these two different momentum regions (Figures ?? (low) and ?? (high)), we still see the clear separation between the jet-like production and the underlying event production. We also observe a similar increase in the  $h - \Lambda/h - h$  ratio as a function of multiplicity in both momentum bins. However, the increase in the UE and total ratios appear to be enhanced within the higher  $p_T$  bin when compared with the lower  $p_T$  bin.

The lower momentum bin also sees a steeper increase in the ratio within the away-side jet as a function of multiplicity, hinting that jet-medium interactions in the low momentum region may be causing the away-side  $h - \Lambda/h - h$  ratio to approach the underlying event ratio at high multiplicity.

The per-trigger pairwise yields for both momentum bins can be seen in Figures ?? (low) and ?? (high). We observe similar trends across both momentum bins, including a much larger increase in both jet-like components of the  $h - \Lambda$  yields when compared to the  $h - h$  yields, which appear mostly flat in both  $p_T$  bins. However, the lower momentum bin sees moderate tension between the near and away-side yields of the  $h - \Lambda$  pairs, with the away-side production appearing to be slightly higher than the near-side production across all multiplicity bins. This may also be a hint that  $\Lambda$  production is being enhanced via jet-medium interactions.

## C Jet vs. Total Production comparison

To get a quantitative look at the differences between low multiplicity events (more jet) and high multiplicity events (more underlying event) and the effect this has on the correlation ratios, we can measure the ratio of Jet pairs over Total pairs (i.e. the fraction of correlated pairs that are in a jet) (fig. ??).

From this measurement, there is a clear difference in behavior of jet production of associated  $\phi$  mesons vs. associated inclusive hadrons as multiplicity increases. The fraction of jet-produced hadrons shows a sharp decrease as a function of multiplicity, while the fraction of jet-produced  $\phi$  mesons is significantly lower and flatter as a function of multiplicity. This shows that the balance of production methods of  $\phi$  mesons are mostly independent of multiplicity, while the production methods of hadrons significantly shifts from jet production towards underlying event production as multiplicity increases.

## D Investigating Radial Flow Effects

The two momentum bins chosen show that there is a relatively narrow momentum range (approx.  $2 < p_T < 4 \text{ GeV}/c$ ) that contains sufficient jet production as well as sufficient production in the underlying event to give a statistically meaningful comparison. However, since this ratio is performed in a narrow range, an additional check was performed to look for the effect of radial flow pushing particles into this momentum range as multiplicity increases.

For this purpose, a simple Boltzmann model was chosen to reflect the effect of the radial flow on the spectra of the different particle species:

$$B(p_T) = \frac{C}{T(m + T)} p_T \exp(-(m_T - m)/T) \quad (\text{D.1})$$

where  $m$  is the particle's mass,  $m_T$  is the transverse mass,  $C$  is a scaling parameter, and  $T$  is the free temperature parameter.

For each particle species,  $T$  was found such that the  $\langle p_T \rangle$  for the Boltzmann distribution for a given multiplicity matched with the measured  $\langle p_T \rangle$  previously reported by ALICE (fig. ??).

After fitting the temperatures of the Boltzmann spectra to the measured  $\langle p_T \rangle$ , the spectra were compared between low and high multiplicity regions to see the effect of the increased temperature on production in our chosen momentum region (fig. ??). This shows that the lower mass particles have a larger shift into our momentum region than the  $\phi$  meson, due to the fact that the  $\phi$  has a much higher  $\langle p_T \rangle$  than the other particle species.

From these normalized model Boltzmann Spectra, a ratio is constructed in the  $2 < p_T < 4 \text{ GeV}/c$  region to see the effect this simplified radial flow model would have on the final ratio results (fig. ??). Since the  $\phi$  has a much larger  $\langle p_T \rangle$ , and therefore experiences less of a shift into this region, the overall effect is actually a decrease in the  $\phi/h$  ratio vs multiplicity within this momentum region. As this is the opposite of what we see in the measured  $\phi/h$  ratio, we conclude this effect is not confounded our measurement of strangeness enhancement.

## E Single Trigger Selection and Results

Since the correlation measurement gives per-trigger yields of associated pairs, rather than the associated particles directly, it is possible that event-by-event fluctuations in the number of trigger and associated particles can lead to a small difference between the ratio of associated pairs and associated particles. While the number of events with multiple trigger particles in the defined momentum range  $4 < p_T < 8 \text{ GeV}/c$  is only 12% (and therefore the possibility of discrepancy is limited), an additional crosscheck was performed to look for any effect this had on the final measurement.

For this crosscheck, only a single trigger particle was chosen from each event for the correlation (fig. ??). In events with multiple triggers in the  $4 < p_T < 8 \text{ GeV}/c$ , only the highest momentum trigger was kept. In this way, the correlation measurement is changed from a per-trigger yield to a per-triggered-event yield, with the presence of at least one  $4 < p_T < 8 \text{ GeV}/c$  hadron being the trigger condition.

Dividing the per-trigger measurement by the single-trigger measurement, effects on the final  $\Delta\phi$  correlations is seen to be a flat scale factor across multiplicity. This scale factor for the (h-h) correlation is found to be 1.2, while the (h- $\phi$ ) correlation is essentially unchanged (fig. ??). The slight difference seen in the structure of the (h-h) correlation is caused by the hardening of the trigger spectra (since choosing the highest trigger will skew the trigger momentum).

841 Since the single trigger analysis acts as a flat scale factor on our original correlation, the effect on our  
842 measurement would only be a change of scale on the final  $\phi/h$  ratio. This shows the validity of our  
843 method of using standard per-trigger correlations to accurately capture the behavior of the  $\phi/h$  ratio in  
844 different production regimes, while also demonstrating the care that needs to be taken when directly  
845 comparing this measurement to inclusive  $\phi/h$  yield measurements.

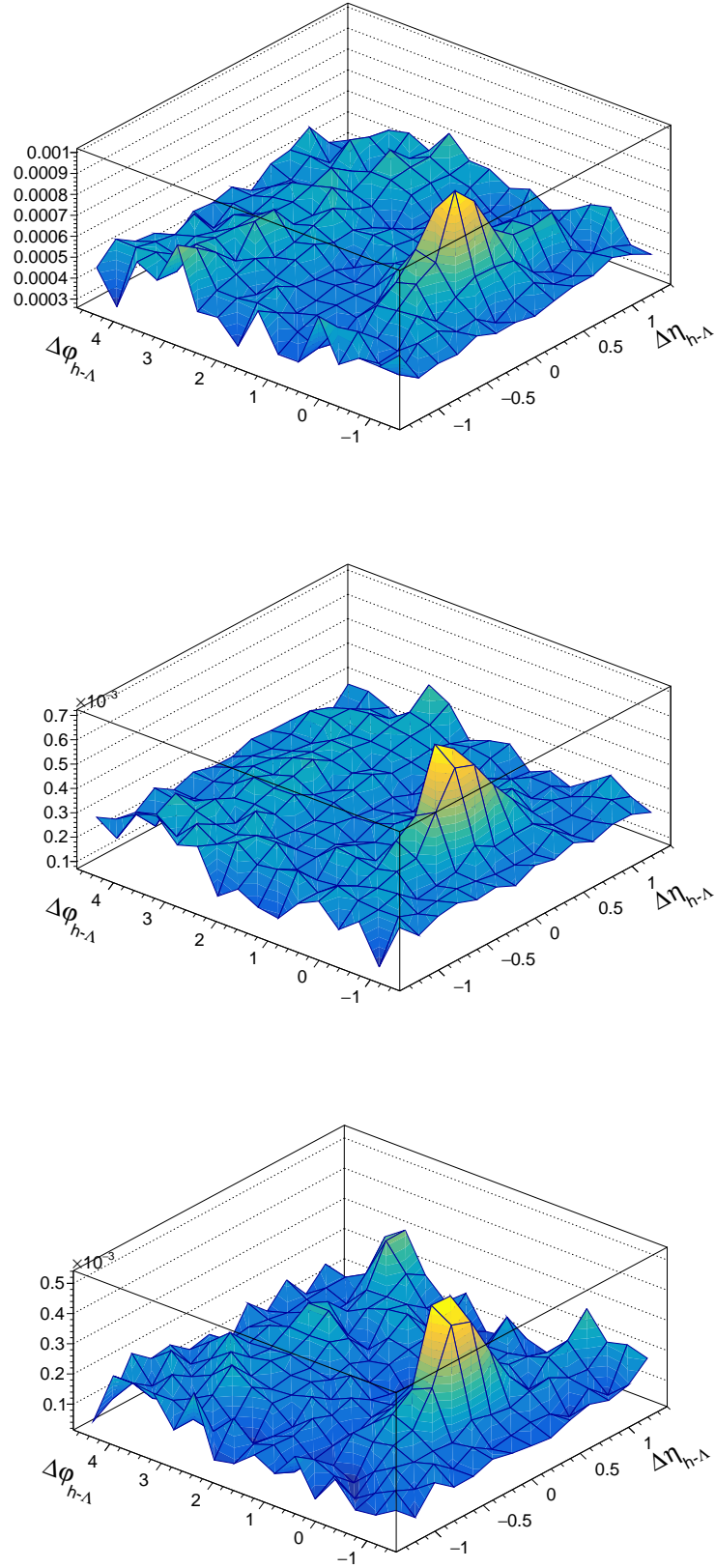


**Fig. A.7:** The final per-trigger  $h - \Lambda$  2D  $\Delta\eta\Delta\phi$  distributions after mixed event acceptance correction and combinatorial background subtraction for the 0-20% (top), 20-50%(center) and 50-80% (bottom) multiplicity bins.

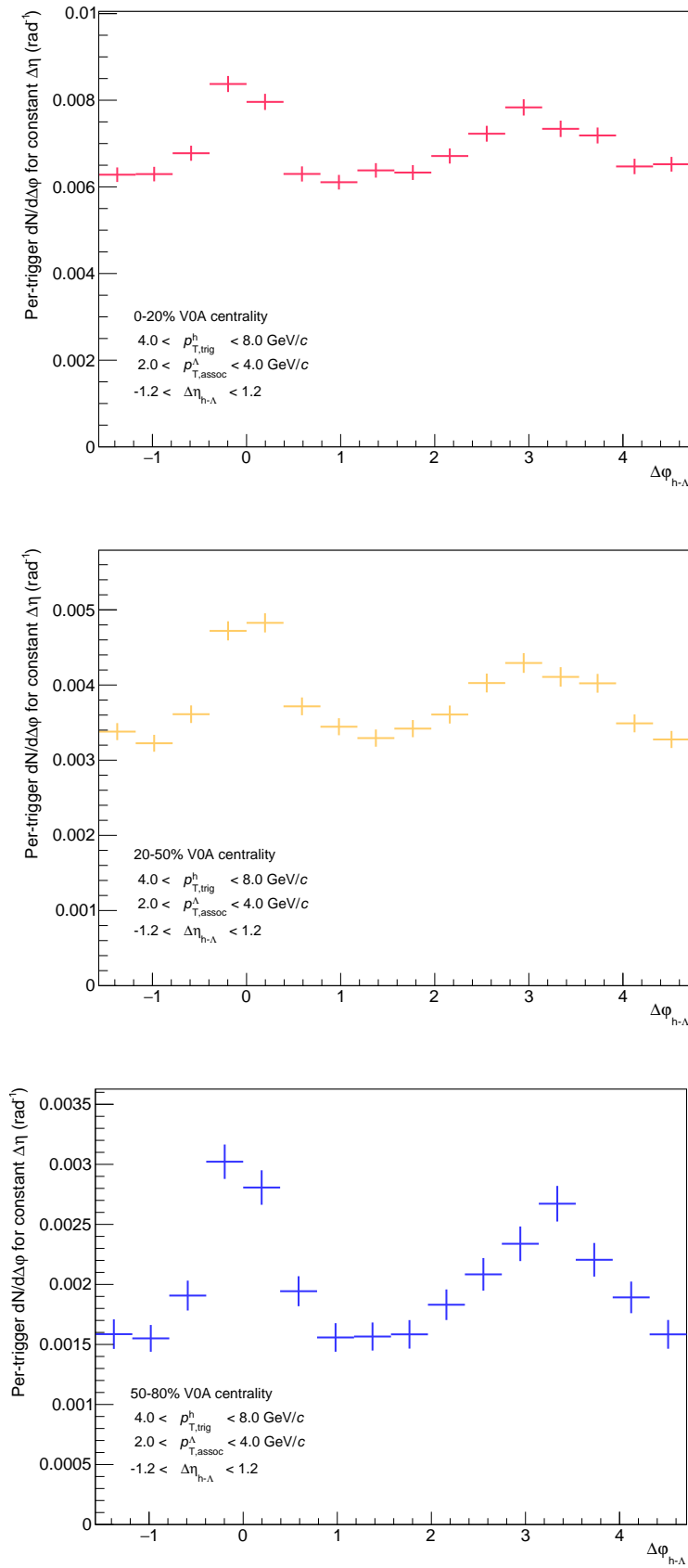


**Fig. A.8:** The final per-trigger  $h - \Lambda$   $\Delta\phi$  distributions after mixed event acceptance correction and combinatorial background subtraction for the 0-20% (top), 20-50% (center) and 50-80% (bottom) multiplicity bins within  $-1.2 < \Delta\eta < 1.2$ .



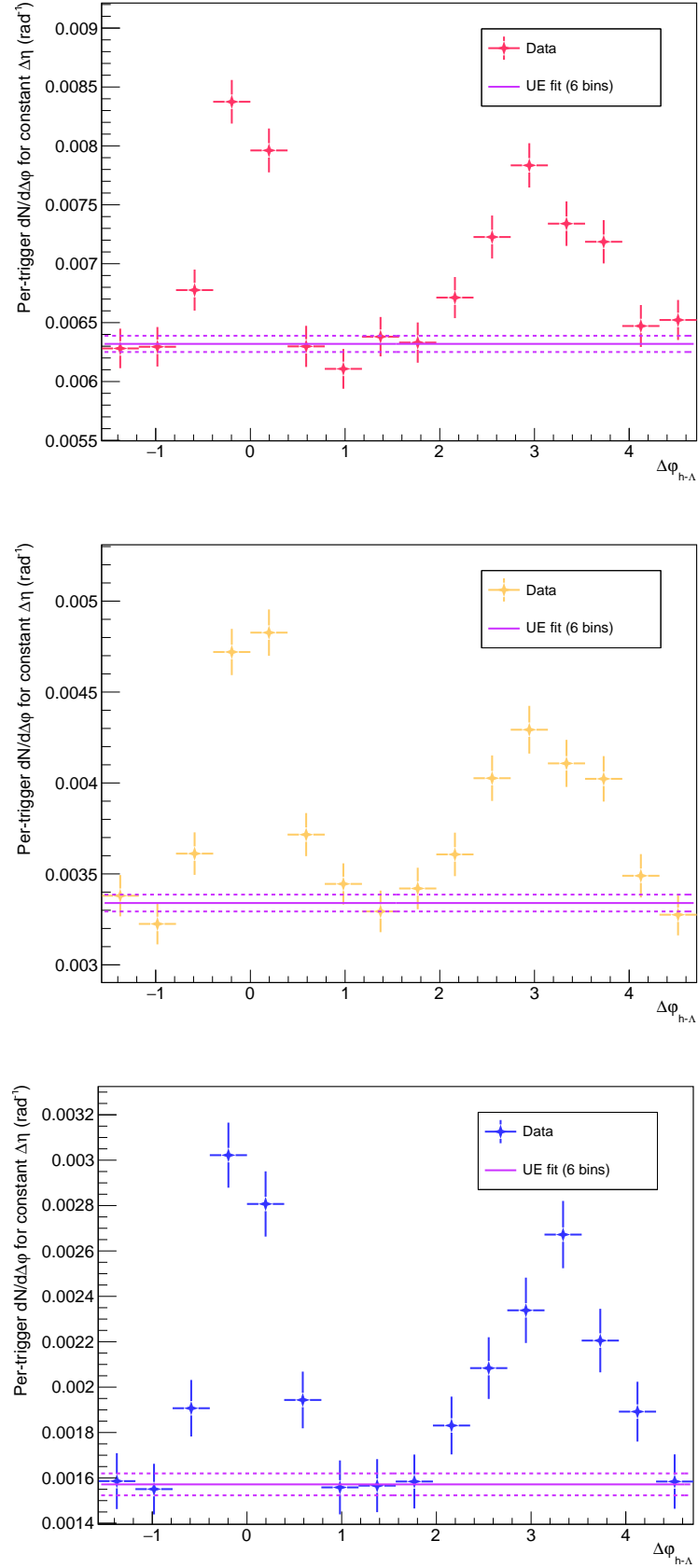


**Fig. A.9:** The final  $h - \Lambda$   $\Delta\phi$  correlations with underlying event fit for the 0-20% (top), 20-50%(center) and 50-80% (bottom) multiplicity bins. The solid line is the central value for the fit, with the dashed lines representing the error (+/-). The underlying event fit was taken using the 6-bin technique described in Section ??.

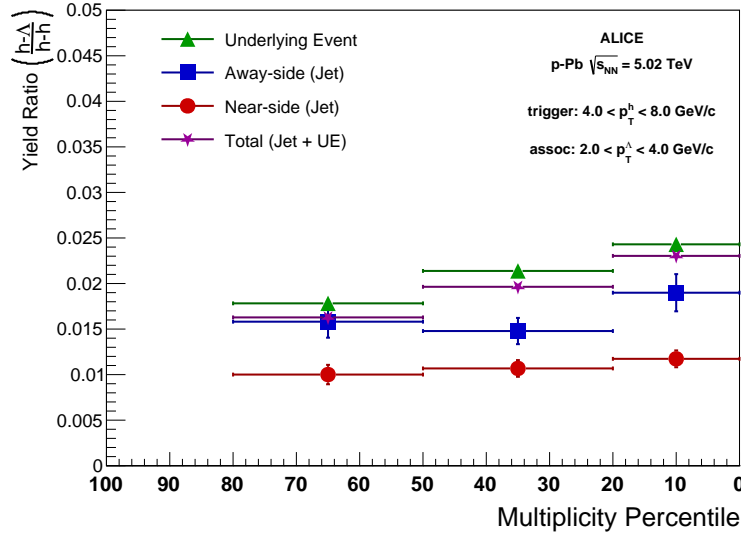


**Fig. A.10:** The final  $h - \Lambda/h - h$  ratio vs. multiplicity plot for  $\Lambda_s$  reconstructed using the resonance technique. While the error bars and statistical fluctuations are larger than the same plot with  $\Lambda_s$  reconstructed using the V0 technique (due to the comb. BG subtraction), the general trends are the same.

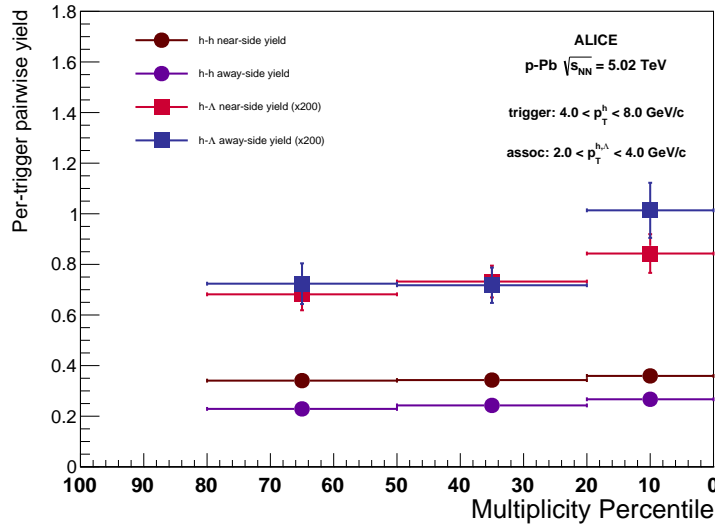


**Fig. A.11:** The final  $h - \Lambda/h - h$  per-trigger pairwise jet yields vs. multiplicity plot for  $\Lambda_s$  reconstructed using the resonance technique. The general trends are very similar to the same plot with  $\Lambda_s$  reconstructed using the V0 technique, just with larger uncertainties.

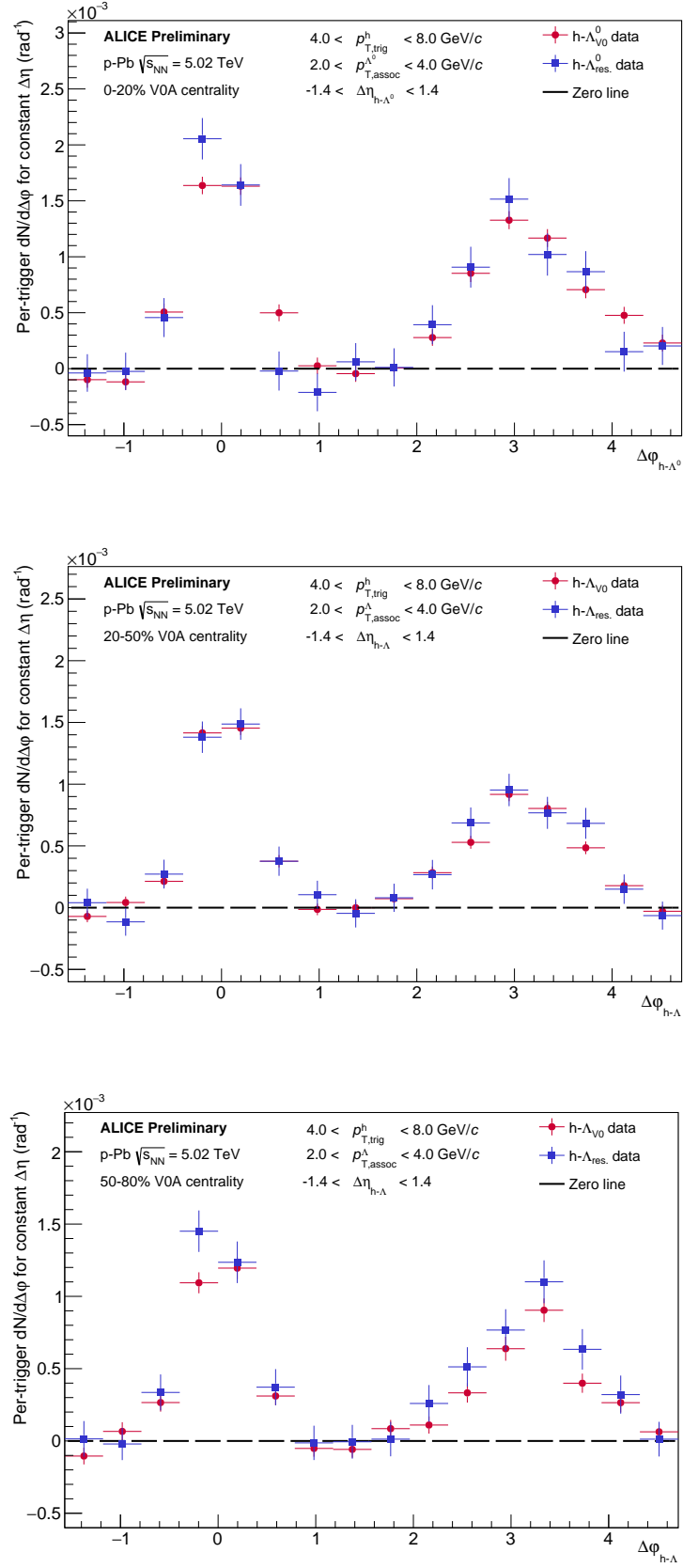


**Fig. A.12:** The final per-trigger  $h - \Lambda$   $\Delta\phi$  correlations for  $\Lambda$ s reconstructed using the resonance technique (blue) and the V0 technique (red) for each multiplicity bin (from top to bottom). All three multiplicity bins show very good agreement between the two techniques.

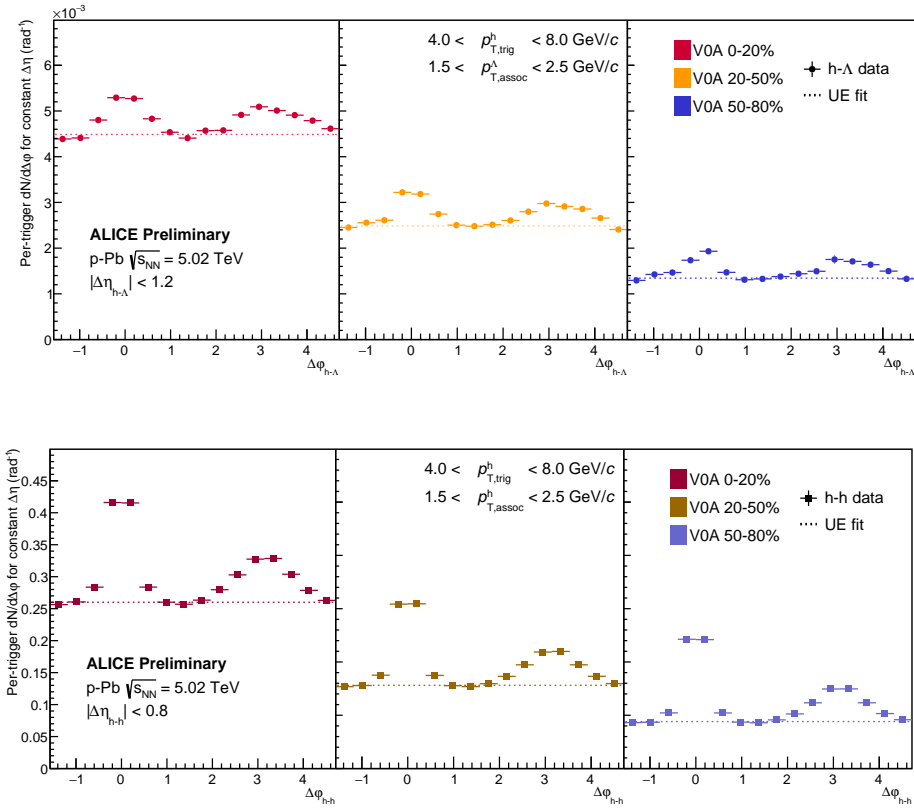


**Fig. B.1:** Final  $h-\Lambda$  (top) and  $h-h$  (bottom)  $\Delta\phi$  distributions in the low  $p_T$  bin. The jet-like components appear suppressed when compared to our full momentum range measurement.

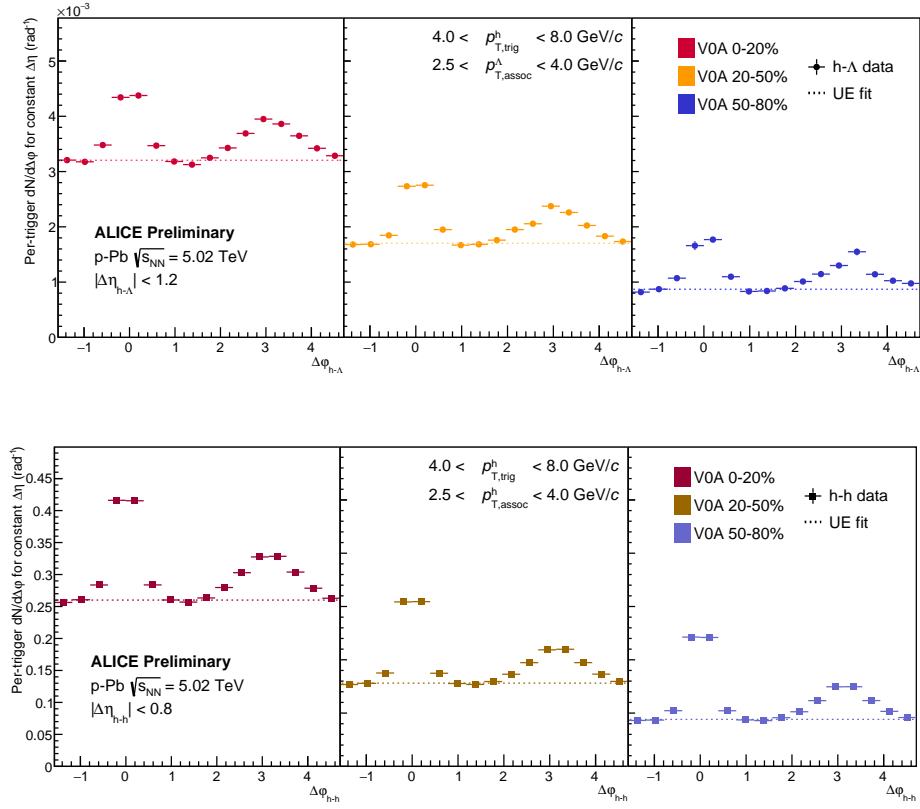


**Fig. B.2:** Final  $h - \Lambda$  (top) and  $h - h$  (bottom)  $\Delta\phi$  distributions in the high  $p_T$  bin. There appears to be a slight enhancement of the jet-like components when compared to our full momentum range measurement.

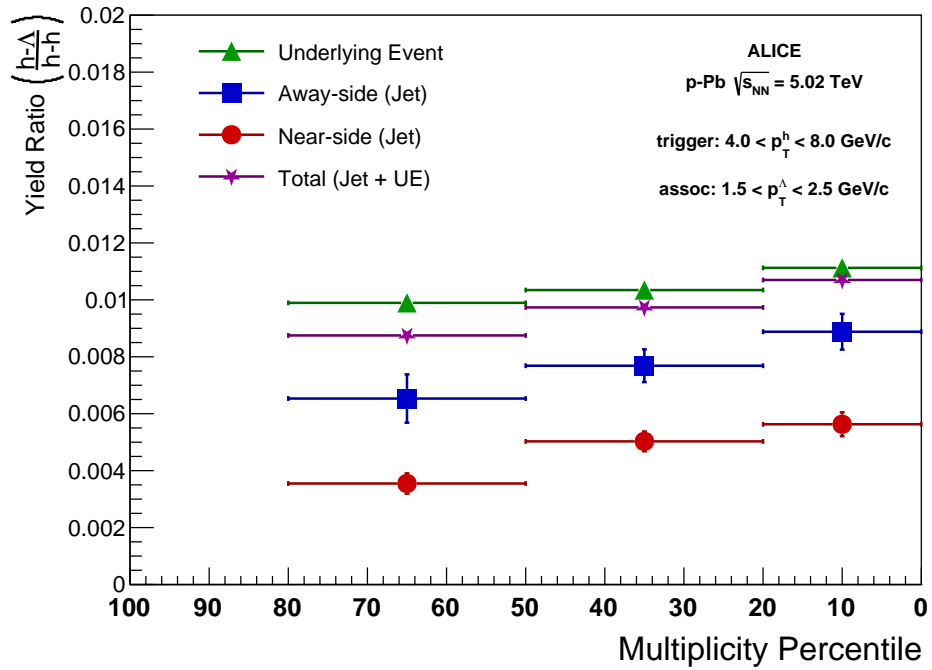


**Fig. B.3:** The final  $h - \Lambda/h - h$  ratios as a function of multiplicity in the  $1.5 < p_T < 2.5$  GeV/c bin.

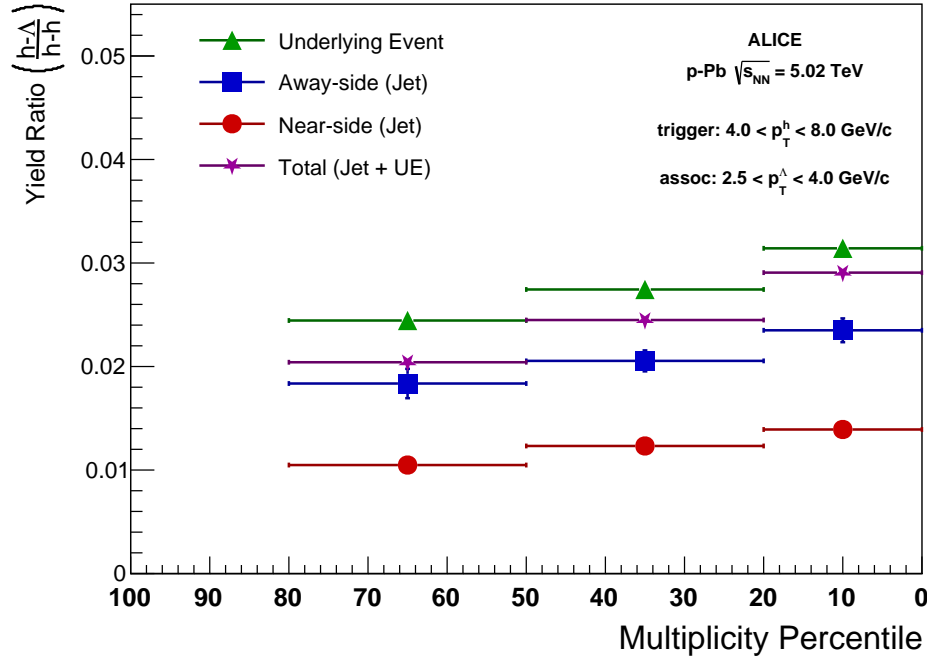


**Fig. B.4:** The final  $h - \Lambda/h - h$  ratios as a function of multiplicity in the  $2.5 < p_T < 4.0$  GeV/c bin.

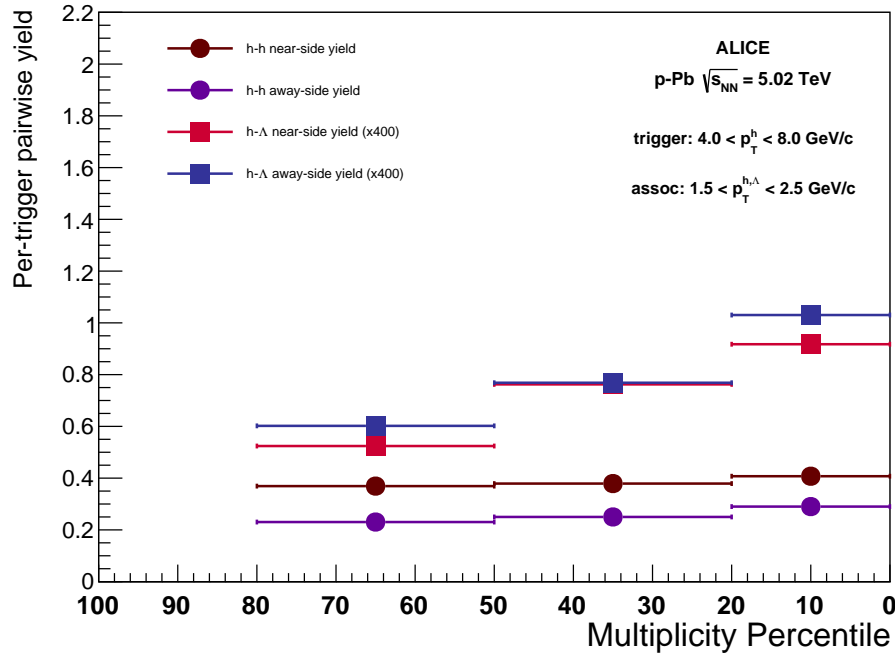


**Fig. B.5:** The final per-trigger  $h - \Lambda$  and  $h - h$  yields as a function of multiplicity in the  $1.5 < p_T < 2.5$  GeV/c bin.

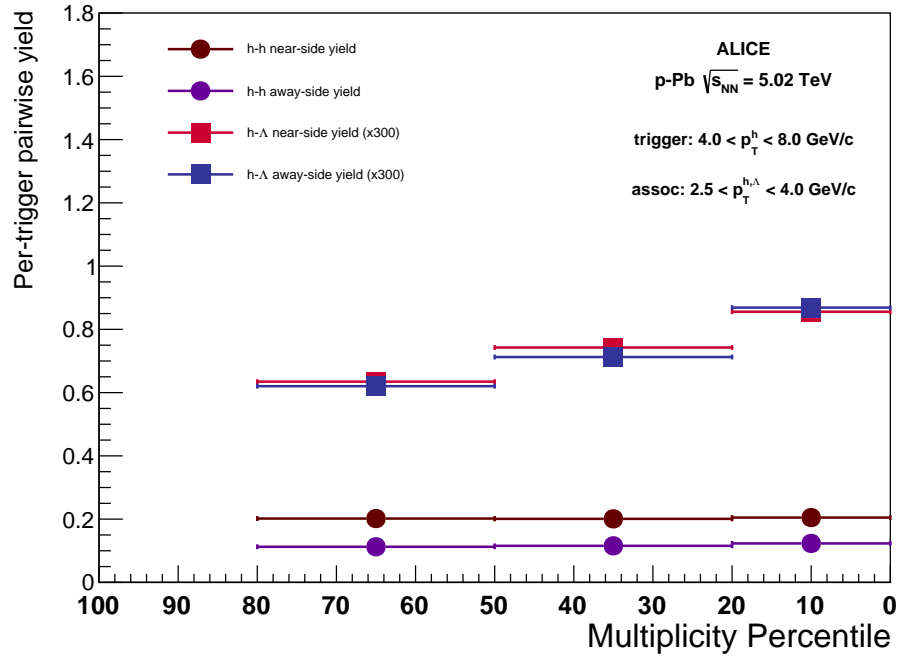


**Fig. B.6:** The final per-trigger  $h - \Lambda$  and  $h - h$  yields as a function of multiplicity in the  $2.5 < p_T < 4.0$  GeV/c bin.

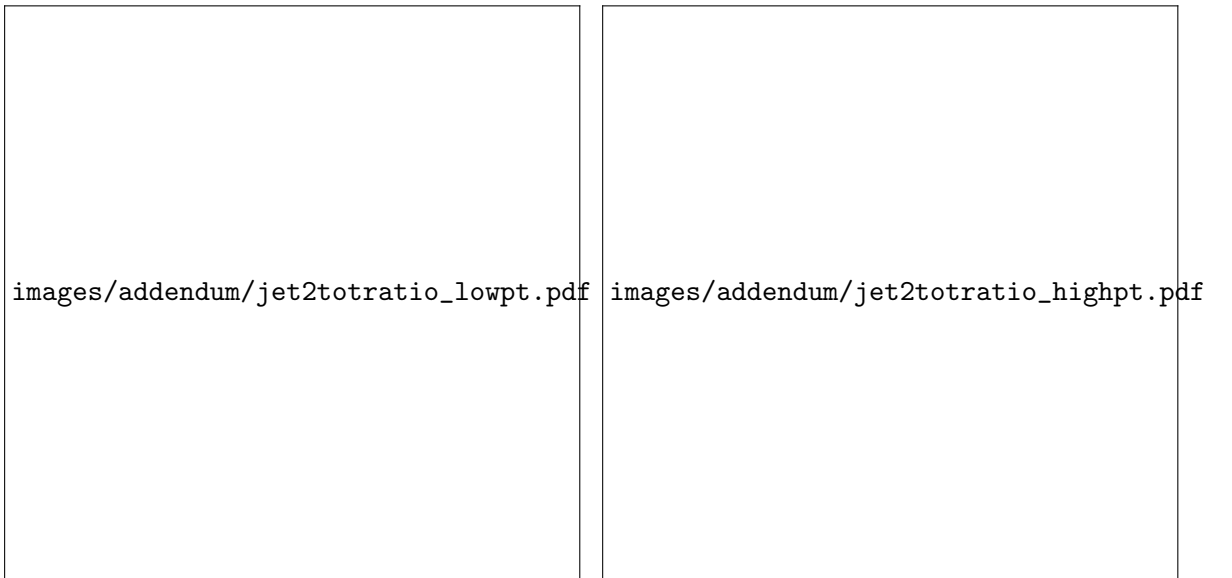


**Fig. C.1:** Fraction of Jet Produced correlated pairs as a function of multiplicity for low momentum (left) and high momentum (right) regions. In both momentum regions, the Jet fraction of  $h-h$  pairs decreases significantly as a function of multiplicity. For  $h-\phi$  pairs, however, the overall fraction coming from jets only slightly decreases as multiplicity increases.



**Fig. D.1:** Temperature of the Boltzmann model for different particle species and multiplicities (left) to match the Boltzmann spectra  $\langle p_T \rangle$  to the published ALICE values (right).

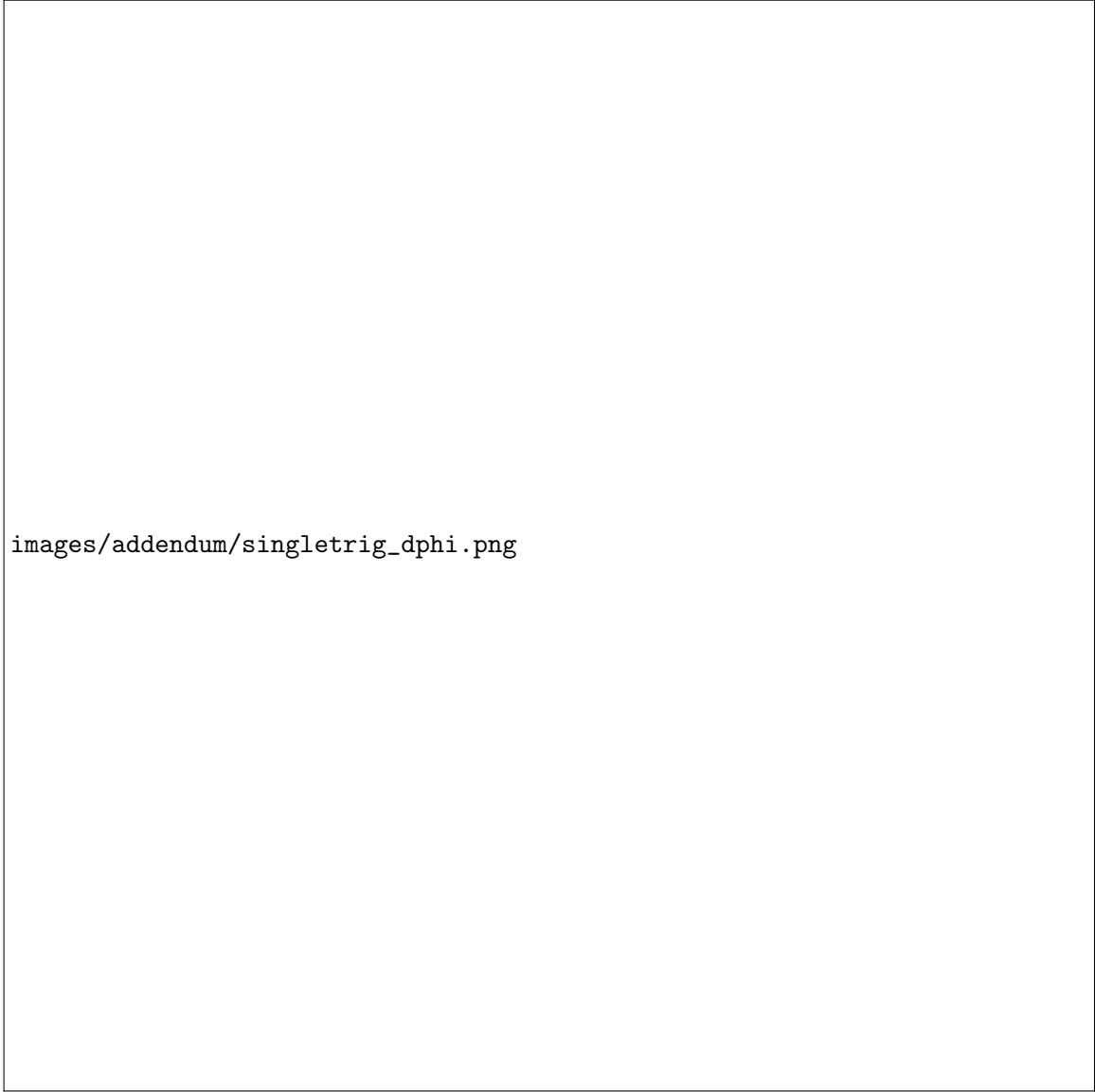


**Fig. D.2:** Boltzmann model spectra comparison between a low and high multiplicity bin for the  $\phi$  (left) and pion (right). While both particles are shifted to high momentum at high multiplicity, the pion sees a much larger increase in the marked  $2 < p_T < 4 \text{ GeV}/c$  region



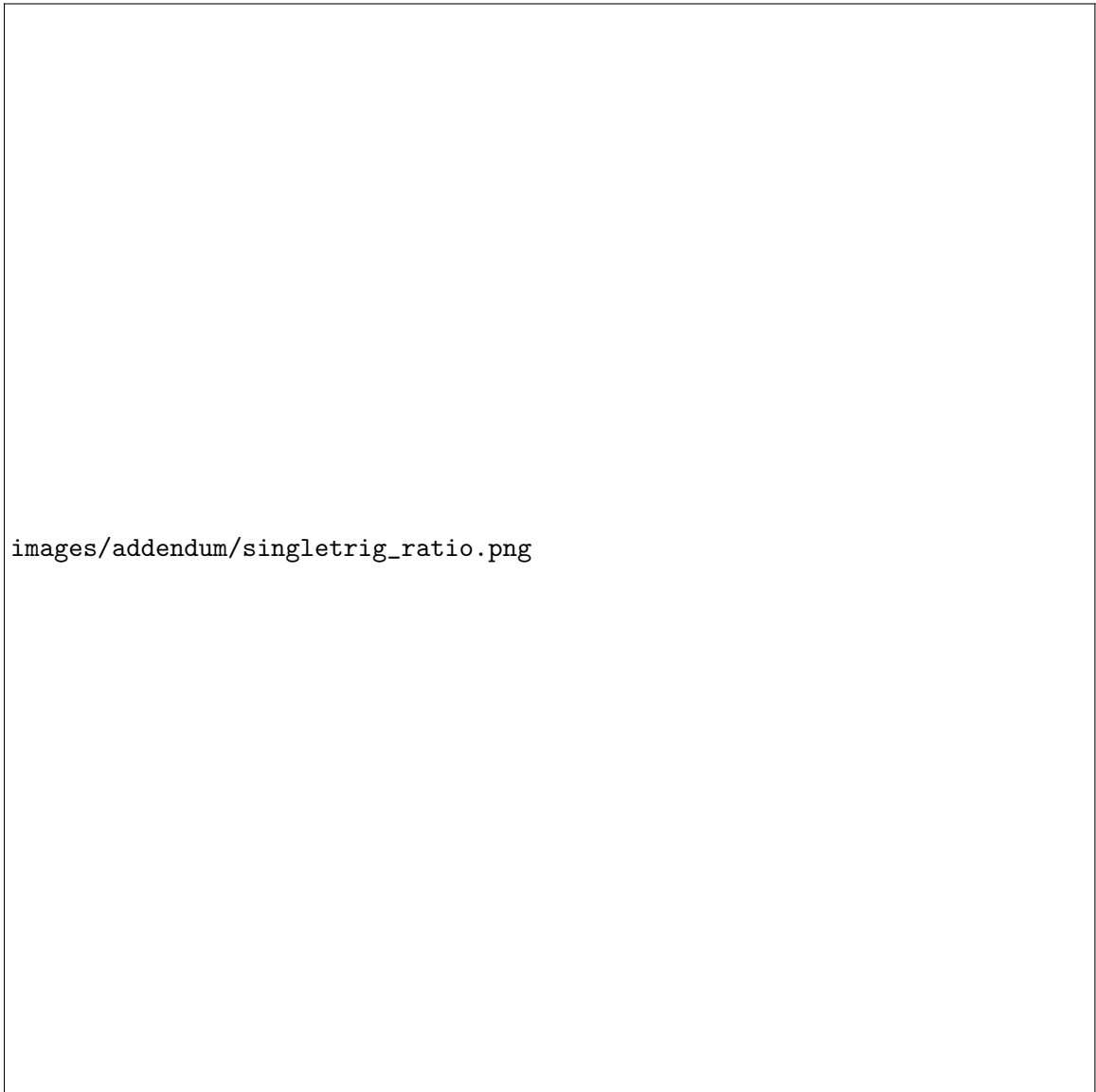


**Fig. D.3:** Normalized ratio of  $\phi$  to stable hadrons vs. multiplicity based on the simplified Boltzmann model fit from measured  $\langle p_T \rangle$  in the region  $2 < p_T < 4 \text{ GeV}/c$ . From the model results, the effect of increased  $\langle p_T \rangle$  would actually decrease the  $\phi/h$  ratio due to the much higher  $\langle p_T \rangle$  of the  $\phi$  compared to the other hadrons.

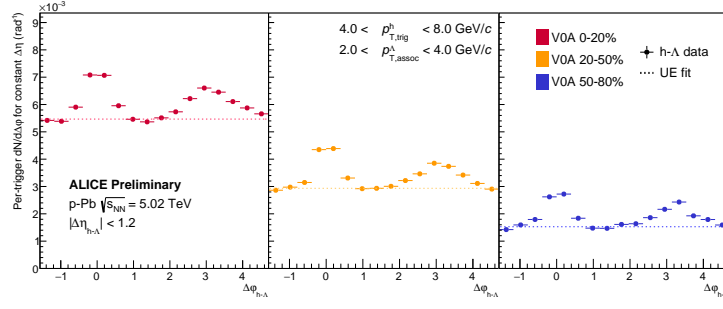
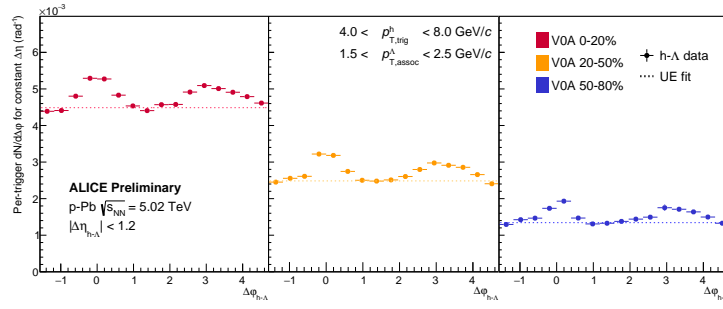
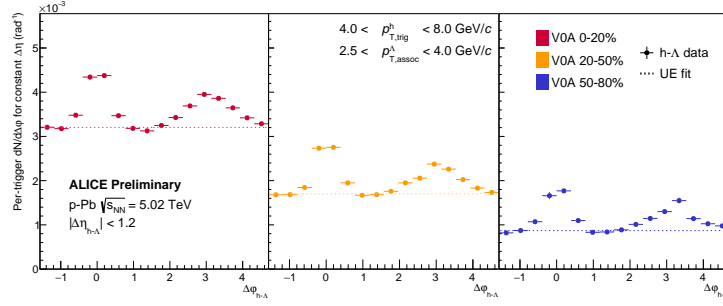


images/addendum/singletrig\_dphi.png

**Fig. E.1:** Comparison between the standard per-trigger correlation (solid markers) and the highest-trigger correlation (open markers) for the 20-50% multiplicity bin.




**Fig. E.2:** Ratio of the standard per-trigger correlation to the single-trigger correlation. The effect of choosing a single high trigger is a constant scaling across all multiplicities. Since most events that have a  $\phi$  meson only have a single  $\phi$  meson, the change in trigger scaling has a negligible effect on the  $h - \phi$  correlation.

846 **F Searchable Section****Fig. F.1:** The  $h - \Lambda$   $\Delta\phi$  plots for each multiplicity bin in the  $p_T$  bin  $2.0 < p_T < 4.0$  GeV/c.**Fig. F.2:** The  $h - \Lambda$   $\Delta\phi$  plots for each multiplicity bin in the  $p_T$  bin  $1.5 < p_T < 2.5$  GeV/c.**Fig. F.3:** The  $h - \Lambda$   $\Delta\phi$  plots for each multiplicity bin in the  $p_T$  bin  $2.5 < p_T < 4.0$  GeV/c.

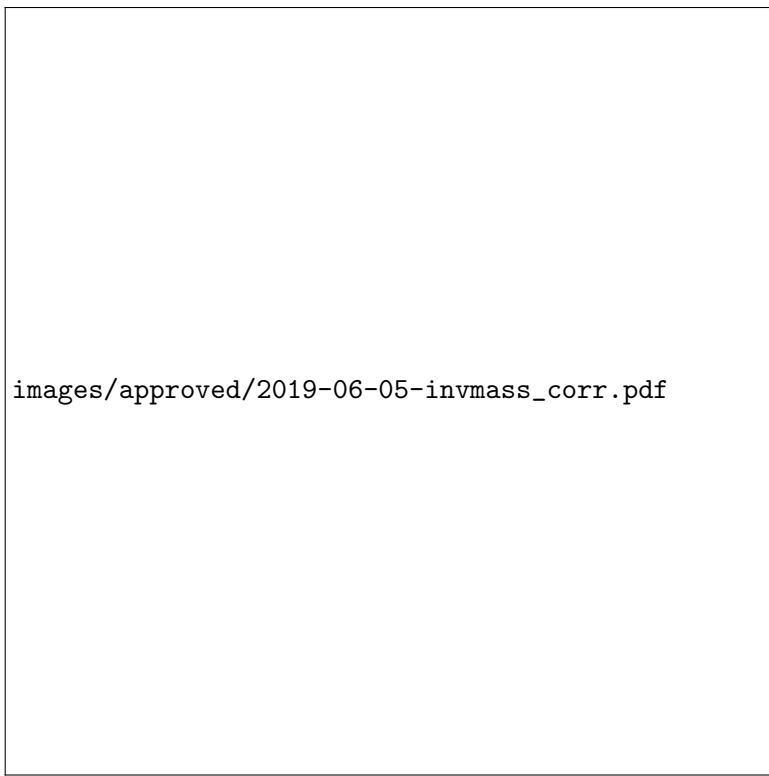
## 847 **G Additional Plots**

### 848 **G.1 Approved Plots**




images/approved/2019-06-05-invmass\_raw.pdf

**Fig. G.1:**



images/approved/2019-06-05-invmass\_corr.pdf

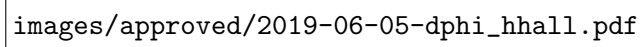
**Fig. G.2:**



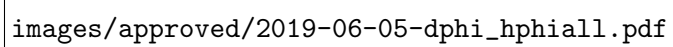
images/approved/2019-06-04-dphi\_bgcompare.pdf

**Fig. G.3:**

**Fig. G.4:**



images/approved/2019-06-05-dphi\_hhall.pdf



images/approved/2019-06-05-dphi\_hphia11.pdf



849 **G.2 Misc. Plots**

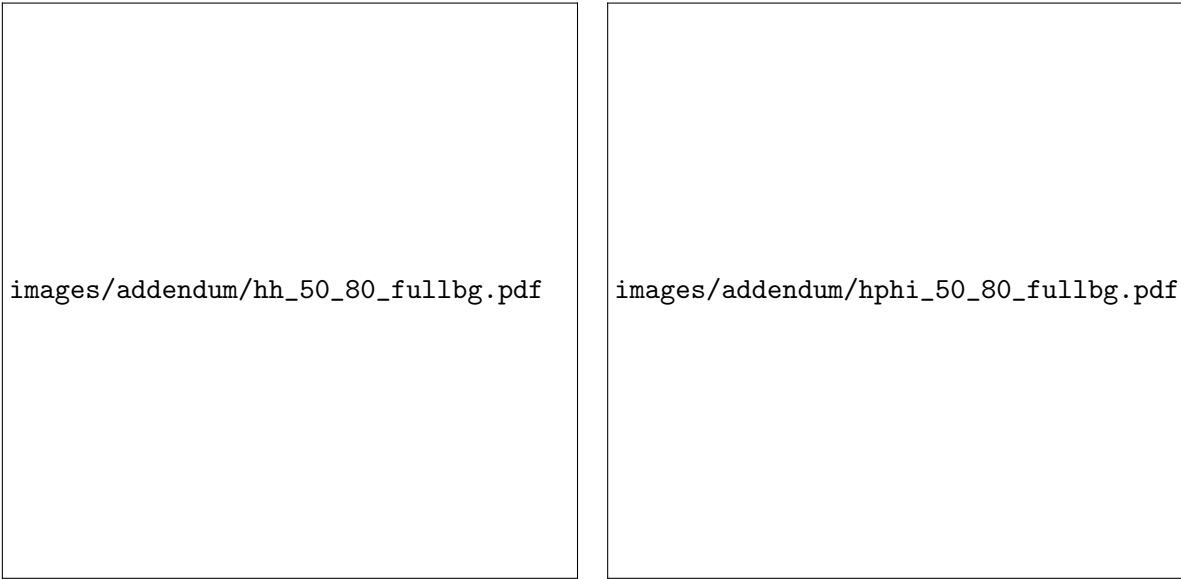


**Fig. G.6:**

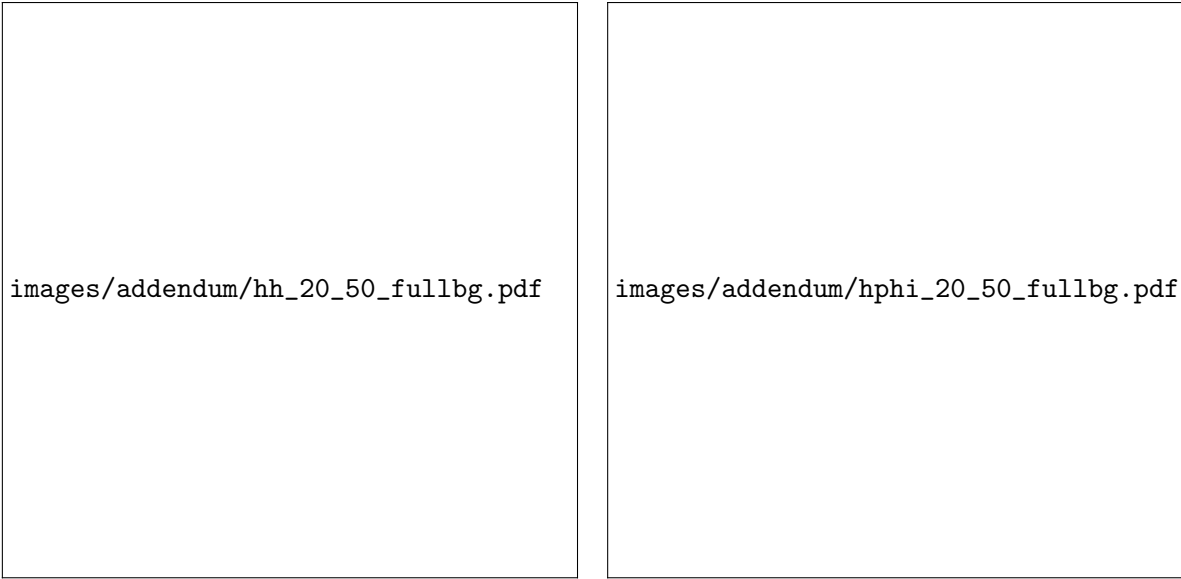


**Fig. G.7:**



**Fig. G.8:**